High-fidelity hot gates for generic spin-resonator systems

M. J. A. Schuetz,[1] G. Giedke,[2,3] L. M. K. Vandersypen,[4] and J. I. Cirac[1]
[1]*Max-Planck-Institut für Quantenoptik, Hans-Kopfermann-Str. 1, 85748 Garching, Germany*
[2]*Donostia International Physics Center, Paseo Manuel de Lardizabal 4, E-20018 San Sebastián, Spain*
[3]*Ikerbasque Foundation for Science, Maria Diaz de Haro 3, E-48013 Bilbao, Spain*
[4]*Kavli Institute of NanoScience, TU Delft, P.O. Box 5046, 2600 GA Delft, The Netherlands*
(Received 8 July 2016; revised manuscript received 18 April 2017; published 17 May 2017)

We propose and analyze a high-fidelity hot gate for generic spin-resonator systems which allows for coherent spin-spin coupling, in the presence of a thermally populated resonator mode. Our scheme is nonperturbative in the spin-resonator coupling strength, applies to a broad class of physical systems, including, for example, spins coupled to circuit-QED and surface acoustic wave resonators as well as nanomechanical oscillators, and can be implemented readily with state-of-the-art experimental setups. We provide and numerically verify simple expressions for the fidelity of creating maximally entangled states under realistic conditions.

DOI: 10.1103/PhysRevA.95.052335

I. INTRODUCTION

Motivation. The physical realization of a large-scale quantum information processing (QIP) architecture constitutes a fascinating problem at the interface between fundamental science and engineering [1,2]. With single-qubit control steadily improving in various physical setups, further advances towards this goal currently hinge upon realizing *long-range* coupling between the logical qubits since coherent interactions at a distance do not only relax some serious architectural challenges [3], but also allow for applications in quantum communication, distributed quantum computing, and some of the highest tolerances in error-correcting codes based on long-distance entanglement links [2,4,5]. One particularly prominent approach to address this problem is to interface qubits with a common quantum bus which effectively mediates long-range interactions between distant qubits, as has been demonstrated successfully for superconducting qubits [6,7] and trapped ions [8].

Executive summary. In the spirit of the celebrated Sørensen-Mølmer or similar gates for *hot* trapped ions [9–20], here we propose and analyze a generic bus-based quantum gate between distant (solid-state) qubits coupled to one resonator mode which allows for coherent spin-spin coupling, even if the mode is thermally populated. For certain times the qubits are shown to disentangle entirely from the (thermally populated) resonator mode, thereby providing a gate that is insensitive to the state of the resonator, without any need of cooling it to the ground state. While a similar gate has been considered for two superconducting qubits and (practically) zero temperature in Refs. [21,22], here we show that this gate opens up the prospect of operating and coupling qubits at elevated temperatures $\sim$(1–4) K (as opposed to millikelvin). This finding brings about the potential to integrate the qubit plane right next to the classical cryogenic electronics; therefore, our scheme may provide a solution to the solid-state QIP interconnect problem between the quantum (for encoding quantum information) and the classical layer (for classical control and read-out) [23]. Our approach should be accessible to a broad class of physical systems [24], including for example circuit-QED setups with both (i) superconducting qubits [6,21,22,25] and (ii) spin qubits [26–45], (iii) spins coupled to surface acoustic wave (SAW) resonators [46–48], and (iv) spins coupled to nanomechanical oscillators [49–53]; compare Fig. 1. We discuss in detail the dominant sources of errors for our protocol, due to rethermalization of the resonator mode and qubit dephasing, and numerically verify the expected error scaling.

II. THE SCHEME

We consider a set of spins (qubits) $i = 1,2,\ldots$ with transition frequencies ω_q coupled to a common (bosonic) cavity mode of frequency ω_c, as described by the Hamiltonian ($\hbar = 1$)

$$H = \omega_c a^\dagger a + \frac{\omega_q}{2} S^z + g\mathcal{S} \otimes (a + a^\dagger), \tag{1}$$

with $\mathcal{S} = \sum_{i,\alpha} \eta_i^\alpha \sigma_i^\alpha$, $S^z = \sum_i \sigma_i^z$, where $\vec{\sigma}_i$ refer to the usual Pauli matrices describing the qubits, and a is the bosonic annihilation operator for the resonator mode. The operator $\mathcal{S}$ is a generalized (collective) spin operator which accounts for both transversal ($\alpha = x,y$) and longitudinal ($\alpha = z$) spin-resonator coupling; the unit-less parameters η_i^α capture potential anisotropies and inhomogeneities in the single-photon (or single-phonon) coupling constants $g_i^\alpha = \eta_i^\alpha g$. Similar to existing (low-temperature) schemes [27,43], the spin-resonator coupling $g = g(t)$ is assumed to be tunable on a time scale $\ll \omega_c^{-1}$; for details we refer to Appendix D.

Typically, for artificial atoms such as quantum dots the qubit transition frequencies ω_q are highly tunable. In what follows, we consider the regime where ω_q is much smaller than all other energy scales; therefore, for the purpose of our analytical derivation, effectively we take $\omega_q = 0$. The robustness of our scheme against nonzero splittings ($\omega_q > 0$) will be discussed below. In this limit, the Hamiltonian given in Eq. (1) can be rewritten as

$$H = \omega_c \left(a + \frac{g}{\omega_c}\mathcal{S}\right)^\dagger \left(a + \frac{g}{\omega_c}\mathcal{S}\right) - \frac{g^2}{\omega_c}\mathcal{S}^2. \tag{2}$$

Using the relation $UaU^\dagger = a + (g/\omega_c)\mathcal{S}$, with the unitary (polaron) transformation $U = \exp[g/\omega_c \mathcal{S}(a - a^\dagger)]$, Eq. (2)

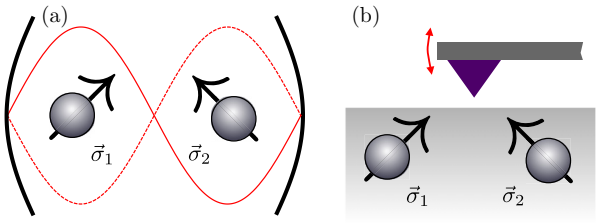

FIG. 1. Schematic illustration for a generic spin-resonator system, comprising a set of spins $\{\vec{\sigma}_i\}$ coupled to a common resonator mode [as provided by, e.g., (a) a transmission line or (b) nanomechanical oscillators], with a nonvanishing thermal occupation.

can be recast into the form

$$H = U\underbrace{\left[\omega_c a^\dagger a - \frac{g^2}{\omega_c}\mathcal{S}^2\right]}_{H_0}U^\dagger, \tag{3}$$

where we have used that $\mathcal{S}$ commutes with U. The time evolution governed by the Hamiltonian H reads as

$$e^{-iHt} = e^{-iUH_0U^\dagger t} = Ue^{-i\omega_c t a^\dagger a}e^{i\frac{g^2}{\omega_c}t\mathcal{S}^2}U^\dagger, \tag{4}$$

where the second equality directly follows from $\exp(x) = \sum_n x^n/n!$ and $U^\dagger U = \mathbb{1}$. For certain times where $\omega_c t_m = 2\pi m$ (with m integer), the first exponential equals the identity, $\exp[-i\omega_c t a^\dagger a] = \exp[-i2\pi m a^\dagger a] = \mathbb{1}$, since the number operator $\hat{n} = a^\dagger a$ has an integer spectrum $0,1,2,\ldots$. Thus, for $t_m = (2\pi/\omega_c)m$, the full time evolution reduces to

$$e^{-iHt_m} = e^{i\frac{g^2}{\omega_c}t_m\mathcal{S}^2} = \exp[i2\pi m(g/\omega_c)^2\mathcal{S}^2]. \tag{5}$$

This relation comes with two major implications: (i) Our approach is not based on a perturbative argument; therefore, apart from Eq. (5), the resonator-mediated qubit-qubit interaction does not lead to any further undesired, spurious terms. (ii) Since the unitary transformation given in Eq. (5) does *not* contain any operators acting on the resonator mode, it is completely insensitive to the state of the resonator [9,10,12], even though the spin-spin interactions present in $\mathcal{S}^2$ have been established effectively via the resonator degrees of freedom; similar considerations have been applied for the case of two (superconducting) qubits for a zero-temperature mode [22] and for small finite temperature T in a classically modeled mode [21]. For specific times, the time evolution in the polaron and the laboratory frame fully coincide and become truly independent of the resonator mode, allowing for the realization of a *thermally* robust gate, without any need of cooling the resonator mode to the ground state. This statement holds provided that rethermalization of the resonator mode can be neglected over the relevant gate time. The experimental implications for this condition will be discussed below.

To further illustrate Eq. (5), let us consider three paradigmatic examples: (1) For longitudinal coupling ($\eta_i^z = 1$, $\eta_i^x = \eta_i^y = 0$), as could be realized (for example) with defect spins coupled to nanomechanical oscillators [50], we can identify the effective spin-spin Hamiltonian $H_{\rm eff} = \Omega_m(\sigma_1^z + \sigma_2^z)^2$, which results in a relative phase $\phi = 4\Omega_m$ for the states $|11\rangle = |\Uparrow\Uparrow\rangle, |00\rangle = |\Downarrow\Downarrow\rangle$ as compared to the states $|10\rangle$ and $|01\rangle$, respectively. By adding a local unitary on both qubits, such that $|0\rangle_i \to \exp(-i\phi/2)|0\rangle_i$ and $|1\rangle_i \to \exp(i\phi/2)|1\rangle_i$, in total for $\phi = \pi/2$ we obtain a controlled phase gate $U_{\rm Cphase} = {\rm diag}(1,1,1,-1)$, which gives a phase of -1 exclusively to $|11\rangle$, while leaving all other states invariant. Note that such a controlled phase gate can be implemented even in the presence of nonzero and inhomogeneous qubit-level splittings ($\omega_q > 0$), when applying either fast local single-qubit gates (to correct the effect of known $\omega_q \neq 0$) or standard spin-echo techniques (to compensate unknown detunings), thereby lifting the requirement of having a small qubit-level splitting ω_q; see Appendix H for details. (2) Again, for longitudinal coupling ($\eta_i^z = 1, \eta_i^x = \eta_i^y = 0$) and $N \geqslant 2$ qubits, Eq. (5) results in a unitary transformation $U = \exp[-i\theta I_z^2]$ generated by a nonlinear top Hamiltonian describing precession around the $I_z = \sum_i \sigma_i^z$ axis with a rate depending on the z component of angular momentum [12], which can be used to simulate nonlinear spin models [12]. (3) For transversal coupling with $\mathcal{S} = \sigma_1^x + \sigma_2^x$, as could be realized (for example) with quantum dot based qubits embedded in circuit-QED cavities [29,43] or SAW cavities [46,47], we have $\mathcal{S}^2 = 2 \times \mathbb{1} + 2\sigma_1^x\sigma_2^x$. Up to an irrelevant global phase $\phi_{\rm gp}$ due to the first term $\sim\mathbb{1}$, we get

$$e^{-iHt_m} = e^{-i\phi_{\rm gp}}\underbrace{\exp\left[i4\pi m(g/\omega_c)^2\sigma_1^x\sigma_2^x\right]}_{\equiv U_{\rm id}^x(m,g/\omega_c)}, \tag{6}$$

which for $m(g/\omega_c)^2 = \frac{1}{16}$ yields a maximally entangling gate, that is $U_{\rm id}^x(1,\frac{1}{4})|\Uparrow\Downarrow\rangle = \frac{1}{\sqrt{2}}(|\Uparrow\Downarrow\rangle + i|\Downarrow\Uparrow\rangle)$, etc., i.e., initial qubit product states evolve to maximally entangled states, irrespectively of the temperature of the resonator mode, on a time scale $t_{\rm max} = \pi/8g_{\rm eff}$ (where $g_{\rm eff} = g^2/\omega_c$); compare Fig. 2 for an exemplary time evolution, starting initially from the product state $\rho(0) = |\Uparrow\Downarrow\rangle\langle\Uparrow\Downarrow| \otimes \rho_{\rm th}(T)$, with the cavity mode in the thermal state $\rho_{\rm th}(T) = Z^{-1}\exp[-\beta\omega_c a^\dagger a]$, and $\beta = 1/k_BT$. Indeed, entanglement peaks are observed at stroboscopic times ($\omega_c t_m = 2\pi m$), independent of the temperature T, culminating in a maximally entangled state at time $t_{\rm max}$.

III. COUPLING TO THE ENVIRONMENT

In the analysis above, we have ignored the presence of decoherence, which in any realistic setting will degrade the effects of coherent qubit-resonator interactions. Therefore, we complement our analytical findings with numerical simulations of the full master equation for the system's density matrix ρ,

$$\dot{\rho} = -i[H,\rho] + \kappa(\bar{n}_{\rm th}+1)\mathcal{D}[a]\rho + \kappa\bar{n}_{\rm th}\mathcal{D}[a^\dagger]\rho + \frac{\Gamma}{4}\sum_{i=1,2}\mathcal{D}[\sigma_i^z]\rho, \tag{7}$$

where the generic spin-resonator Hamiltonian H is given in Eq. (1) and the last two dissipative terms in the first line of Eq. (7), with $\mathcal{D}[a]\rho = a\rho a^\dagger - \frac{1}{2}\{a^\dagger a,\rho\}$ and a cavity mode decay rate $\kappa = \omega_c/Q$, describe rethermalization of the cavity mode towards the thermal occupation $\bar{n}_{\rm th} = (\exp[\hbar\omega_c/k_BT] - 1)^{-1}$ at temperature T; here, Q is the quality factor of the cavity. The last line in Eq. (7) describes dephasing of the qubits with a dephasing rate $\Gamma \sim 1/T_2^\star$, where $T_2^\star$ is the time-ensemble-averaged dephasing time. As discussed in detail in Appendix J, the noise model underlying Eq. (7) is accurate in the experimentally most relevant regime of

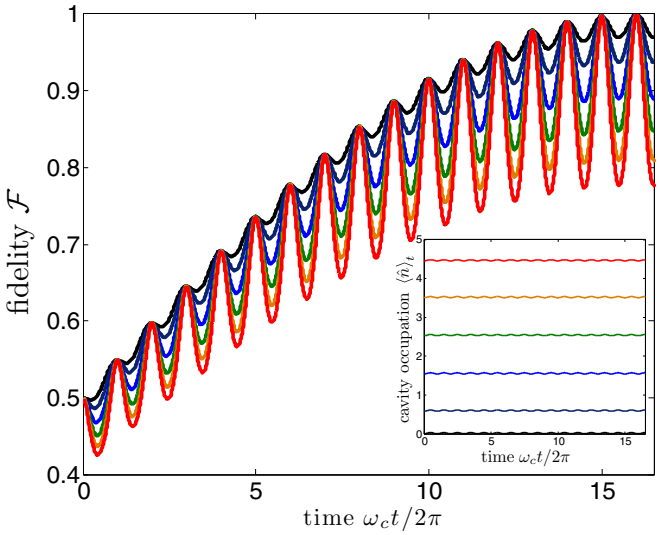

FIG. 2. Fidelity $\mathcal{F}$ with the maximally entangled target state $|\Psi_{\rm tar}\rangle = (|\Uparrow\Downarrow\rangle + i|\Downarrow\Uparrow\rangle)/\sqrt{2}$ for transversal coupling ($\mathcal{S} = \sigma_1^x + \sigma_2^x$), the initial product state $\rho(0) = |\Uparrow\Downarrow\rangle\langle\Uparrow\Downarrow| \otimes \rho_{\rm th}(T)$ and different temperatures $k_BT/\omega_c = 0,1,2,3,4,5$. Independently of the temperature T, the spins periodically disentangle from the (hot) resonator mode and systematically build up entanglement among themselves. While the peaks are merely independent of temperature, the amplitude of the precursory oscillations do increase with temperature. Inset: occupation of the resonator $\langle\hat{n}\rangle_t$ showing small oscillations due to weak entanglement between the qubits and the cavity mode [10]. Other numerical parameters: $\omega_q/\omega_c = \Gamma = 0$, $g/\omega_c = \frac{1}{16}$, $\kappa/\omega_c = Q^{-1} = 10^{-5}$.

weak spin-resonator coupling ($g \ll \omega_c$), where (within the approximation of independent rates of variation [54]) the interactions with the environment can be treated separately for spin and resonator degrees of freedom. In Eq. (7) we have ignored single-spin relaxation processes since the associated time scale T_1 is typically much longer than $T_2^\star$; still, relaxation processes could be included straightforwardly in our model by adding the decay terms $\dot\rho = \cdots + T_1^{-1}\sum_i \mathcal{D}[\sigma_i^-]\rho$ and the corresponding error (infidelity) could be analyzed along the lines of our analysis shown below (see Appendix N for details).

Numerical results. To quantitatively capture the effects of decoherence, in the following we provide numerical results of the master equation (7), for the initial product state $\rho(0) = |\Uparrow\Downarrow\rangle\langle\Uparrow\Downarrow| \otimes \rho_{\rm th}(T)$, and (transversal) spin-resonator coupling with $\eta_i^x = 1$ and $\eta_i^y = \eta_i^z = 0$. As a figure of merit for our protocol, we quantify the state fidelity $\mathcal{F} = \langle\Psi_{\rm tar}|\varrho|\Psi_{\rm tar}\rangle$ with the maximally entangled target state $|\Psi_{\rm tar}\rangle = (|\Uparrow\Downarrow\rangle + i|\Downarrow\Uparrow\rangle)/\sqrt{2}$; here, $\varrho = {\rm tr}_a[\rho]$ refers to the density matrix of the qubits, with ${\rm tr}_a[\dots]$ denoting the trace over the resonator degrees of freedom. As shown in Appendix O, similar results can be obtained for the average gate fidelity. Typical results from our numerical simulations in the presence of noise are displayed in Fig. 3. As expected from our analytical results, for $\omega_c t_m = 2\pi m$ the two qubits disentangle from the thermally populated resonator mode and systematically evolve towards the maximally entangled target state $|\Psi_{\rm tar}\rangle$; for example, for $g/\omega_c = \frac{1}{8}$ (as used in Fig. 3), the spins evolve towards $U_{\rm id}^x(1,\frac{1}{8})|\Uparrow\Downarrow\rangle = \cos(\pi/16)|\Uparrow\Downarrow\rangle + i\sin(\pi/16)|\Downarrow\Uparrow\rangle$ for $m = 1$, $U_{\rm id}^x(2,\frac{1}{8})|\Uparrow\Downarrow\rangle = \cos(\pi/8)|\Uparrow\Downarrow\rangle + i\sin(\pi/8)|\Downarrow\Uparrow\rangle$ for $m = 2$, and $U_{\rm id}^x(3,\frac{1}{8})|\Uparrow\Downarrow\rangle = \cos(3\pi/16)|\Uparrow\Downarrow\rangle + i\sin(3\pi/16)|\Downarrow\Uparrow\rangle$ for $m = 3$, before the entanglement buildup culminates in the fully entangling dynamics $U_{\rm id}^x(4,\frac{1}{8})|\Uparrow\Downarrow\rangle = (|\Uparrow\Downarrow\rangle + i|\Downarrow\Uparrow\rangle)/\sqrt{2}$. For all practical purposes, this statement holds independently of the temperature T and the associated thermal occupation of the resonator mode $\bar n_{\rm th} \approx k_BT/\hbar\omega_c$, provided that the quality factor of the cavity Q is sufficiently high; a quantitative statement specifying this regime will be given below. Moreover, while our analytical treatment has assumed $\omega_q = 0$, we have numerically verified that the proposed protocol is robust against nonzero level splittings of the qubits $\omega_q/\omega_c \lesssim 0.1$; compare the dashed line in Fig. 3 and further information provided in Appendixes G, H, and K.

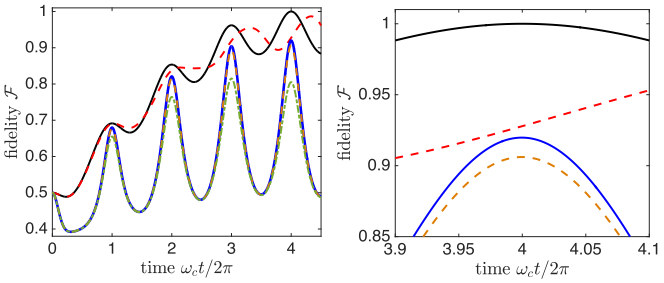

FIG. 3. Fidelity $\mathcal{F}$ (left) in the presence of noise, with a zoom-in around $t_{\rm max}$ (right). As a benchmark, the solid (topmost) black line refers to the quasi-ideal limit ($\Gamma = 0$, $\kappa/\omega_c = Q^{-1} = 10^{-5}$, and $k_BT/\omega_c = 0$), while (only) the red dashed curve accounts for a nonzero qubit-level splitting $\omega_q/\omega_c = 0.1$. The solid blue line also accounts for dephasing of the qubits with a (rather large) dephasing rate $\Gamma/\omega_c = 1\%$ and finite thermal occupation of the resonator mode with $k_BT/\omega_c = 5$ ($\bar n_{\rm th} \approx 4.5$). The results are relatively insensitive to the quality factor of the cavity, provided that $\kappa_{\rm eff} \ll \Gamma$; the orange dashed line (where $Q = 10^3$) is basically identical to the $Q = 10^5$ scenario, whereas the green dashed-dotted (lowest) one with $Q = 10^2$ (that is, $\kappa/\omega_c = \Gamma/\omega_c = 1\%$) shows a clear reduction in $\mathcal{F}$. This result can be traced back to the hot-gate requirement given in Eq. (8). Ideally, maximum entanglement is reached for $f_c t = 4$, with several precursory oscillation peaks at $f_c t = 1,2,3$. Other numerical parameters: $g/\omega_c = \frac{1}{8}$, $\omega_q/\omega_c = 0$ (except for the red dashed curve where $\omega_q/\omega_c = 0.1$).

IV. GATE TIME REQUIREMENTS: ERROR SCALING

As described by Eq. (7), coupling to the environment leads to two dominant error sources: (i) rethermalization of the resonator mode with an effective rate $\sim\kappa\bar n_{\rm th}$, and (ii) dephasing of the qubits on a time scale $\sim T_2^\star$. For any *hot* gate, the associated gate time $t_{\rm gate} \sim g_{\rm eff}^{-1}$, with $g_{\rm eff} = g^2/\omega_c = \mu^2\omega_c$, has to be shorter than the time scale associated with the effective (thermally enhanced) rethermalization rate $\kappa_{\rm eff} = \kappa\bar n_{\rm th} \approx k_BT/Q$. For the gate described above, this directly leads to the requirement

$$g^2/\omega_c \gg k_BT/Q \quad \Leftrightarrow \quad k_BT \ll Q\mu^2\omega_c. \tag{8}$$

Thus, for $T = 1$ K ($k_BT/2\pi \approx 20$ GHz) and a cavity quality factor $Q \approx 10^5$–10^6, we need $g_{\rm eff}/2\pi \gg$ (20–200) kHz. Provided that our assumption $\omega_c \gg \omega_q$ is still fulfilled, for fixed temperature T, quality factor Q, and coupling g, relation

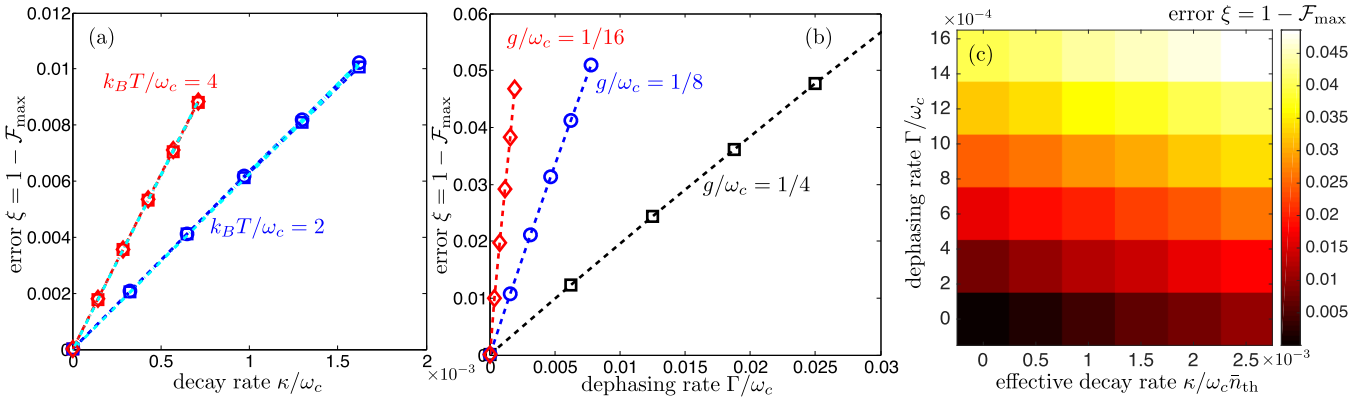

FIG. 4. Errors ($\xi = 1 - \mathcal{F}_{\max}$) due to rethermalization of the cavity mode (a) and qubit dephasing (b). (a) Rethermalization-induced error for $k_BT/\omega_c = 2$ (blue) and $k_BT/\omega_c = 4$ (red), and $\Gamma = 0$. The error ξ_κ is found to be independent of $\mu = g/\omega_c$: $\mu = \frac{1}{16}$ (squares) and $\mu = \frac{1}{8}$ (blue circles and red diamonds). (b) Dephasing-induced errors for $\mu = \frac{1}{4}$ (squares), $\mu = \frac{1}{8}$ (circles), and $\mu = \frac{1}{16}$ (diamonds); here, $\kappa/\omega_c = 10^{-6}$ and $k_BT/\omega_c = 0.01$. In both cases, the linear error scaling is verified. Other numerical parameters: $\omega_q/\omega_c = 0$. (c) Total error ξ as a function of both the effective rethermalization rate $\sim\kappa/\omega_c\bar{n}_{\rm th} \sim \bar{n}_{\rm th}/Q$ and the spin dephasing rate $\sim\Gamma/\omega_c$ for $g/\omega_c = \frac{1}{16}$, $k_BT/\omega_c = 2$, and $\omega_q = 0$.

(8) may be conveniently fulfilled by choosing ω_c sufficiently small, up to the lower limit $\omega_c \geqslant 4g$ (which is needed to fulfill $m \geqslant 1$; compare Appendix C) and at the cost of a potentially relatively large device (since the device dimensions scale with $\sim\lambda_c \sim \omega_c^{-1}$). Conversely, for fixed $\mu = g/\omega_c$ [27,47,55], Eq. (8) can be achieved by choosing ω_c sufficiently large. In addition, the gate time has to be short compared to the qubit's dephasing time $T_2^\star \sim \Gamma^{-1}$, which gives the second requirement

$$g^2/\omega_c \gg \Gamma \quad \Leftrightarrow \quad \Gamma \ll \mu^2\omega_c. \tag{9}$$

For concreteness, let us consider a specific setup where conditions (8) and (9) can be met with state-of-the-art technology: quantum dots (QDs) have been successfully integrated with superconducting microwave cavities, with a relatively large charge-cavity coupling of $g_{\rm ch}/2\pi \sim$ (20–100) MHz [35–38,40]. For QD spin qubits a vacuum Rabi frequency of $g_{\rm sp}/2\pi \sim 1$ MHz has been predicted [28,29,36], with the potential to increase this coupling to $\sim$10 MHz with new, recently demonstrated cavity designs [56]. Furthermore, for superconducting transmission line resonators quality factors $Q \sim 10^6$ have been demonstrated [57]. Then, taking $g_{\rm sp}/2\pi = 10$ MHz, $\omega_c/2\pi \approx$ (0.16–1) GHz, i.e., $g_{\rm eff}/2\pi \approx$ (0.1–0.6) MHz, and $Q = 10^6$, conditions (8) and (9) can be met simultaneously for temperatures $T \sim 1$ K [since $T \ll 5(30)$ K to fulfill condition (8) for $g_{\rm eff}/2\pi \approx 0.1(0.6)$ MHz] and dephasing time scales $T_2^\star \sim 100$ μs [since $\Gamma/2\pi \ll$ (0.1–0.6) MHz to fulfill condition (9)], as has been demonstrated with isotopically purified Si samples [58]. Therefore, a faithful implementation of our gate will *not* require cooling to millikelvin temperatures. Similar promising estimates also apply to spin qubits coupled to SAW resonators; compare Appendix I.

In the following, we quantify the infidelities induced by the two error sources outlined above: rethermalization of the resonator mode during the gate leads to errors (infidelities) if the resonator is entangled with the qubits. Due to leakage of which-way information, resonator noise leads to qubit dephasing at a rate proportional to the relevant separation in phase space, that is the square of the resonator displacement $\mu = g/\omega_c$ [50]. The effective rethermalization-induced dephasing rate for the qubits is then $\Gamma_{\rm eff} \sim \kappa\bar{n}_{\rm th}(g/\omega_c)^2$. To obtain a simple estimate for the rethermalization-induced error, this effective rate $\Gamma_{\rm eff}$ is multiplied with the relevant gate time which scales as $t_{\rm gate} \sim \omega_c/g^2$, yielding the error $\xi_\kappa \sim (\kappa/\omega_c)\bar{n}_{\rm th}$, which is *independent* of the spin-resonator coupling strength g [22,50]; for a full analytical derivation, we refer to Appendix L. However, since the overall gate time $t_{\rm gate} \sim \omega_c/g^2$ increases for small $\mu = g/\omega_c$, errors will accumulate due to direct qubit decoherence processes. Accordingly, errors due to qubit dephasing are expected to scale as $\xi_\Gamma \sim \Gamma/g_{\rm eff} \sim \mu^{-2}\Gamma/\omega_c$. This simple linear scaling holds for a Markovian noise model where qubit dephasing is described by a standard pure dephasing term [compare Eq. (7)] leading to an exponential loss of coherence $\sim\exp[-t/T_2^\star]$; for non-Markovian qubit dephasing a better, sublinear scaling can be expected [46,50]. For small infidelities ($g_{\rm eff} \gg \kappa_{\rm eff}, \Gamma$), the individual linear error terms due to cavity rethermalization and qubit dephasing can be added independently, yielding the total error

$$\xi \approx \alpha_\kappa(\kappa/\omega_c)\bar{n}_{\rm th} + \alpha_\Gamma\Gamma/\omega_c. \tag{10}$$

This simple linear error model has been verified numerically; compare Fig. 4. Based on these results we extract the coefficients $\alpha_\kappa \approx 4$ (which is approximately independent of g [22]; compare Appendixes K and L for details) and $\alpha_\Gamma \approx 0.1/\mu^2$. For $g_{\rm sp}/2\pi \approx 10$ MHz [28,29,56], a relatively low resonator frequency $\omega_c/2\pi = 16g_{\rm sp}/2\pi = 160$ MHz, $T = 1$ K (corresponding to $\bar{n}_{\rm th} \approx 130$), $Q = 10^5$ [56,57], and a realistic dephasing rate $\Gamma/2\pi \approx 0.1$ MHz [58], that is $\kappa/\omega_c\bar{n}_{\rm th} \approx 1.3 \times 10^{-3}$ and $\Gamma/\omega_c \approx 6 \times 10^{-4}$, our estimates then predict an overall infidelity of $\xi \approx 2\%$, with the potential to reach error rates $\xi \approx 0.2\%$ below the threshold for quantum error correction for state-of-the-art experimental parameters ($Q \approx 10^6$, $\Gamma/2\pi \approx 10$ kHz) [4,57,58]. This simple estimate compares well with other bus-based, two-qubit (hot) gates reaching fidelities $\sim$97% [20,50,59] and has been corroborated by numerical simulations that fully account for higher-order errors; compare the density plot in Fig. 4(c). We like to emphasize that, due to the fundamental temperature insensitivity of our gate, technological improvements in the achievable Q factor directly translate to a proportional

reduction of thermalization-induced errors and therefore increase the acceptable temperature. Note that the error estimate given in Eq. (10) assumes perfect timing of the gate, as the maximum fidelity is reached exactly at time $t_{\max}$, whereas under experimentally realistic conditions there will be a residual error due to imperfect timing of the gate. However, as shown in Appendix K, for sufficiently small, but realistic, timing accuracies of $(\omega_c/2\pi)\Delta t \lesssim 1\%$ and small spin-resonator coupling $g/\omega_c \lesssim \frac{1}{16}$ (implying small oscillation amplitudes), the effects of time jitter become negligible.

V. CONCLUSIONS AND OUTLOOK

To conclude, we have proposed and analyzed a high-fidelity hot gate for generic spin-resonator systems which allows for coherent spin-spin coupling, even in the presence of a thermally populated resonator mode. While we have mostly focused on just two spins, our scheme fully applies to more than two spins, which should allow for the preparation of maximally entangled multipartite states; as shown in Ref. [11] in the context of trapped ions, a propagator of the form given in Eq. (5) applied to the initial product state $|00\ldots0\rangle$ may be used to generate states of the form $1/\sqrt{2}(|00\ldots0\rangle + e^{i\phi}|11\ldots1\rangle)$, where $|00\ldots0\rangle$ and $|11\ldots1\rangle$ are product states with all qubits in the same state $|0\rangle$ or $|1\rangle$, respectively.

ACKNOWLEDGMENTS

M.J.A.S. would like to thank T. Shi for useful discussions. M.J.A.S., L.M.K.V., and J.I.C. acknowledge support by the EU project SIQS. M.J.A.S. and J.I.C. also acknowledge support by the Deutsche Forschungsgemeinschaft (DFG) within the Cluster of Excellence NIM. G.G. acknowledges financial support by the Spanish Ministerio de Economía y Competitividad through the Project No. FIS2014-55987-P. L.M.K.V. acknowledges financial support by a European Research Council Synergy grant.

APPENDIXES

The following appendixes provide additional background material to specific topics of the main text. They are structured as follows: In Appendix A we provide typical thermal occupation numbers $\bar{n}_{\rm th}$ for relevant experimental parameter regimes. In Appendix B we compare the ideal evolution in the laboratory frame to the one in the polaron frame. In Appendix C we derive the ideal gate time $t_{\max}$. In Appendix D we discuss a prototypical implementation of a spin-resonator system that allows for time-dependent control of the spin resonator $g = g(t)$, as required for the faithful realization of the proposed hot gate. In Appendix E we discuss the standard approach to coupling spins via a common resonator mode in the dispersive regime, in which, in contrast to the proposed hot gate, the spin degrees of freedom do not fully disentangle from the resonator mode. In Appendix F we compare our general result to a perturbative calculation in the framework of a Schrieffer-Wolff transformation. In Appendixes G and H we analyze in detail the effects coming from a nonzero qubit-level splitting $(\omega_q/\omega_c > 0)$. In Appendix I we provide further details on how to implement experimental candidate systems governed by the class of Hamiltonians given in Eq. (1), using quantum dots embedded in high-quality surface acoustic wave (SAW) resonators. In Appendix J we provide a microscopic derivation of the master equation given in Eq. (7) of our paper. In Appendix K we present further results based on the numerical simulation of the master equation given in Eq. (7) of the main text. In Appendix L we derive an analytical expression for rethermalization-induced errors, while Appendix M provides an analytical model for dephasing-induced errors. In Appendix N we address in detail errors induced by relaxation processes. In Appendix O we conclude with a discussion on the average gate fidelity.

APPENDIX A: THERMAL OCCUPATION

Here, we first provide typical thermal occupation numbers $\bar{n}_{\rm th}$ for relevant experimental parameter regimes. At a temperature $T = 4$ K, a (mechanical) oscillator of frequency $\omega_c/2\pi \sim$ (1–10) GHz has a thermal equilibrium occupation number much larger than one, $\bar{n}_{\rm th} \approx 8$–$80$ (compare Fig. 5).

APPENDIX B: POLARON VERSUS LABORATORY FRAME

In this Appendix we show that for stroboscopic times the ideal time evolution in the laboratory frame fully coincides with the one in the polaron frame. In the ideal (noise-free) scenario, the evolution of the system in the laboratory frame, comprising both spin and resonator degrees of freedom, is described by Schrödinger's equation

$$i\frac{d}{dt}|\psi\rangle_t = H|\psi\rangle_t. \tag{B1}$$

In the polaron frame, the time evolution is governed by

$$i\frac{d}{dt}|\tilde{\psi}\rangle_t = H_0|\tilde{\psi}\rangle_t, \tag{B2}$$

where $|\tilde{\psi}\rangle_t = U^\dagger|\psi\rangle_t$, $U = \exp[\mu S(a - a^\dagger)]$, and $H_0 = U^\dagger H U = \omega_c a^\dagger a - \frac{g^2}{\omega_c}\mathcal{S}^2$; the polaron transformation U entangles spin with resonator degrees of freedom. The solution to Eq. (B2) reads as $|\tilde{\psi}\rangle_t = \exp[-iH_0 t]|\tilde{\psi}\rangle_0$. Using the

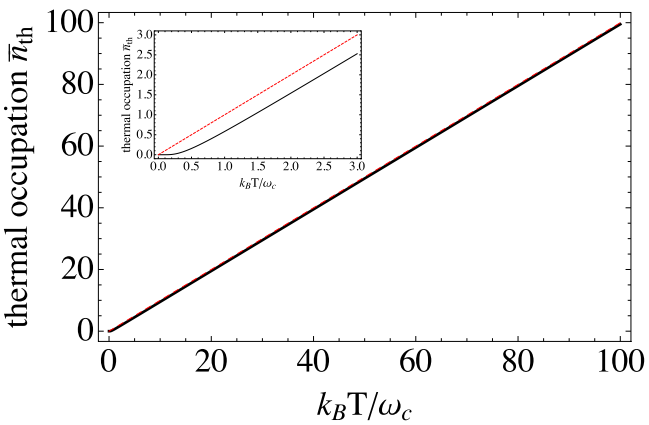

FIG. 5. Thermal occupation $\bar{n}_{\rm th} = (\exp[\hbar\omega_c/k_BT] - 1)^{-1}$ (black solid line) and high-temperature approximate result $\bar{n}_{\rm th} \approx k_BT/\hbar\omega_c$ (red dashed line). For $T = 4$ K and $\omega_c/2\pi = 1$ GHz ($\omega_c/2\pi =$ 10 GHz), we have $k_BT/\hbar\omega_c \approx 80$ ($k_BT/\hbar\omega_c \approx 8$). For $T = 1$ K and $\omega_c/2\pi = 1$ GHz ($\omega_c/2\pi = 10$ GHz), we have $\bar{n}_{\rm th} \approx 20$ ($\bar{n}_{\rm th} \approx 2$).

relation $\exp[-i\omega_c t a^\dagger a] = \exp[-i2\pi m a^\dagger a] = \mathbb{1}$ for stroboscopic times ($\omega_c t_m = 2\pi m$, with m integer), full time evolution in the polaron frame reduces to

$$|\tilde{\psi}\rangle_{t_m} = e^{i2\pi m\mu^2\mathcal{S}^2}|\tilde{\psi}\rangle_0. \tag{B3}$$

Transforming back to the laboratory frame with $|\tilde{\psi}\rangle_t = U^\dagger|\psi\rangle_t$, and using that U commutes with the propagator $\exp[i2\pi m\mu^2\mathcal{S}^2]$, we obtain the (stroboscopic) solution in the laboratory frame $|\psi\rangle_{t_m} = e^{i2\pi m\mu^2\mathcal{S}^2}|\psi\rangle_0$, which fully coincides with the one in the polaron frame.

APPENDIX C: GATE TIME

Ideally, the gate time $t_{\rm gate}$ has to fulfill two conditions: (i) it has to be chosen stroboscopically, that is, $\omega_c t_{\rm gate} = 2\pi m$, with $m = 1,2,\ldots$ with (ii) the parameters such that $m\mu^2 = \frac{1}{16}$ in order to obtain a maximally entangling gate (in the absence of noise). Combination of (i) and (ii) then yields the ideal gate time

$$t_{\rm max} = \frac{\pi}{8g_{\rm eff}}, \tag{C1}$$

as given in the main text. The gate time $t_{\rm max}$ should be short compared to the relevant noise time scales, which yields the requirement $g_{\rm eff} \gg \kappa_{\rm eff}, \Gamma$. In principle, large values of $g_{\rm eff} = g^2/\omega_c$ can be obtained by choosing the resonator frequency ω_c sufficiently small, provided that ω_c can be tuned independently of g. This can be done up to the lower bound $\omega_c \geqslant 4g$ which follows directly from the requirement $m = 1/(16\mu^2) \geqslant 1$.

APPENDIX D: TIME-DEPENDENT CONTROL OF THE SPIN-RESONATOR COUPLING

In this Appendix we discuss in detail a prototypical implementation of a spin-resonator system that allows for time-dependent control of the spin-resonator coupling $g = g(t)$, as required for the faithful realization of the proposed hot gate. Here, we first focus on a *charge* qubit embedded in a lithographically defined double quantum dot (DQD) containing a single electron, and then extend our analysis to a singlet-triplet *spin* qubit made out two electrons in such a DQD. Based on the electric dipole interaction, this type of device may be coupled either to a microwave transmission line resonator in a circuit-QED-like setup, as investigated theoretically and experimentally in (for example) Refs. [35,36,40], or a surface-acoustic-wave resonator, as described in Refs. [46,47]. Our approach then employs standard all-electrical manipulation strategies, in which external, tunable gate voltages are used for (basically) *in situ* control of the effective spin-resonator coupling [26], provided that standard adiabaticity conditions are fulfilled [43], with the additional requirement of having a relatively small qubit transition frequency ω_q when the (hot) gate is turned on; as shown in Appendix H, this condition can be dropped, however, for longitudinal spin-resonator coupling.

1. Double quantum dot charge qubit

The Hamiltonian describing a tunnel-coupled DQD in the single-electron regime coupled to a cavity of frequency ω_c is given by [31–33]

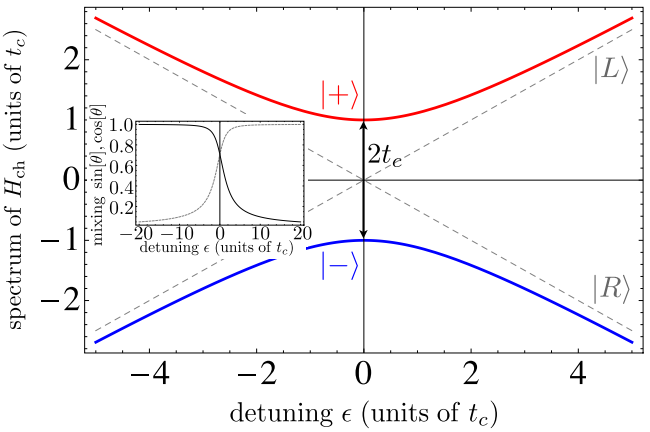

FIG. 6. Spectrum of the DQD Hamiltonian in the single-electron regime, $H_{\rm ch} = \frac{\epsilon}{2}\tau^z + t_c\tau^x$, as a function of the interdot detuning parameter ϵ. Inset: mixing parameters $\sin\theta$ (black solid) and $\cos\theta$ (gray dashed) as a function of the interdot detuning parameter ϵ.

$$H = \frac{\epsilon}{2}\tau^z + t_c\tau^x + \omega_c a^\dagger a + g_{\rm ch}\tau^z \otimes (a + a^\dagger), \tag{D1}$$

where ϵ is the (tunable) level detuning between the dots, t_c gives the (tunable) tunnel coupling, and $g_{\rm ch}$ refers to the single-photon (phonon) coupling strength between the resonator and the DQD. The electron charge state is described in terms of orbital Pauli operators defined as $\tau^z = |L\rangle\langle L| - |R\rangle\langle R|$ and $\tau^x = |L\rangle\langle R| + |R\rangle\langle L|$, respectively, with $|L\rangle(|R\rangle)$ corresponding to the state where the electron is localized in the left (right) dot, while $a^\dagger$ (a) are the standard resonator creation (annihilation) operators.

Diagonalization of the first two terms in the Hamiltonian H, that is, $H_{\rm ch} = \frac{\epsilon}{2}\tau^z + t_c\tau^x$, yields the electronic charge eigenstates

$$|+\rangle = \cos\theta|L\rangle + \sin\theta|R\rangle, \tag{D2}$$

$$|-\rangle = -\sin\theta|L\rangle + \cos\theta|R\rangle, \tag{D3}$$

where the mixing angle is given by $\tan\theta = 2t_c/(\epsilon + \omega_q)$, and $\omega_q = \sqrt{\epsilon^2 + 4t_c^2}$ refers to the energy splitting between the eigenstates $|\pm\rangle$; compare Fig. 6. The logical qubit basis is (by definition) given by the superposition states $|\pm\rangle = (|L\rangle \pm |R\rangle)/\sqrt{2}$ at the charge degeneracy point ($\epsilon = 0$), where to first order the qubit is insensitive to charge fluctuations ($d\omega_q/d\epsilon = 0$). In the eigenbasis of $H_{\rm ch}$, and after a simple gauge transformation ($a \to -a$, $a^\dagger \to -a^\dagger$), the spin-resonator Hamiltonian given in Eq. (D1) can be rewritten as

$$H = \frac{\omega_q}{2}\sigma^z + \omega_c a^\dagger a + (g^x\sigma^x - g^z\sigma^z) \otimes (a + a^\dagger). \tag{D4}$$

Here, we have introduced the Pauli operators as $\sigma^z = (|+\rangle\langle+| - |-\rangle\langle-|)$, and $\sigma^x = (|+\rangle\langle-| + |-\rangle\langle+|)$; the transversal and longitudinal coupling parameters are given by

$$g^x = g_{\rm ch}\frac{2t_c}{\omega_q}, \tag{D5}$$

$$g^z = g_{\rm ch}\frac{\epsilon}{\omega_q}. \tag{D6}$$

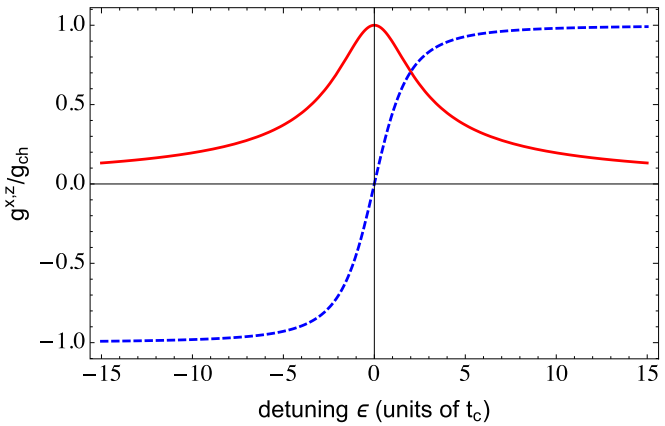

FIG. 7. Effective spin-resonator coupling g^x (solid) and g^z (dashed) as a function of the interdot detuning parameter ϵ.

By redefining the interdot detuning parameter as $\epsilon \to -\epsilon$ (or, equivalently, by relabeling $|L\rangle \leftrightarrow |R\rangle$), the spin-resonator Hamiltonian H may be expressed as [26,31]

$$H = \frac{\omega_q}{2}\sigma^z + \omega_c a^\dagger a + (g^x\sigma^x + g^z\sigma^z)\otimes(a + a^\dagger). \quad \text{(D7)}$$

Both the effective transversal coupling parameter g^x as well as the longitudinal coupling parameter g^z can be controlled via rapid all-electrical tuning of either the interdot detuning parameter ϵ and/or the tunnel splitting t_c (recall $\omega_q = \sqrt{\epsilon^2 + 4t_c^2}$) [26,30,31,33,35,43]. As shown in Fig. 7, the transversal coupling parameter g^x is maximized around $\epsilon = 0$ (that is, when the electron is delocalized in both dots), while it is strongly suppressed for $|\epsilon| \gg t_c$. Conversely, the longitudinal coupling parameter g^z is maximized for $|\epsilon| \gg t_c$, while it is strongly suppressed for small detuning $|\epsilon| \ll t_c$. Note that, outside of our regime of interest, in the limit where $\delta, g_{\rm ch} \ll \omega_c$ (with $\delta = \omega_q - \omega_c$) one can perform a rotating-wave approximation yielding the standard Jaynes-Cummings Hamiltonian, as widely discussed in the literature (see, e.g., Refs. [26,30,32,33,35,46]).

Then, since the parameters $\epsilon(t)$ and $t_c(t)$ can be tuned all electrically on very fast time scales, the protocol for the proposed hot gate proceeds as follows: (i) For $\epsilon \sim 0$, the hot gate is turned on, with $g^x \approx g_{\rm ch}$ and $g^z \sim 0$ (corresponding to purely transversal spin-resonator coupling as discussed extensively in the main text). In this regime, the qubit-level splitting is set by the (highly tunable) tunnel coupling, according to $\omega_q \approx 2t_c$, which should be chosen to be much smaller than the cavity frequency ($t_c \ll \omega_c$) in order to satisfy the requirements of the proposed hot gate. (ii) After some well-controlled (stroboscopic) time $t_m = 2\pi m/\omega_c$, the hot gate can be turned off by sweeping ϵ to large detuning values $\epsilon \gg t_c$.

Both regimes are readily achievable in the quantum dot setting: Due to the exponential dependence of tunnel coupling strength t_c on gate voltage, the interdot barrier characterized by t_c can be varied from about 100 μeV (verified by the broadening of the time-averaged charge transition; note that for much larger tunnel couplings, two neighboring dots become one single dot) all the way down to less than 10^{-12} eV $\sim$ 10^{-6} GHz (corresponding to a millisecond time scale, as verified by real-time detection of single charges hopping on or off the dot) [60], which is five to six orders of magnitude smaller than realistic cavity frequencies. Similarly, the detuning ϵ between the dots can be varied anywhere between zero and a positive or negative detuning equal to the addition energy, at which point additional electrons are pulled into the dot. The typical energy scale for the addition energy is very large ($\sim$1–3 meV) [60].

Note that in the proposed offsetting [step (ii)] the qubits and the cavity are not strictly decoupled due to the nonvanishing longitudinal term (compare Fig. 7). For $g_{\rm ch} \ll \omega_c$, this coupling is usually neglected within a rotating-wave approximation [26,32,35]. However, here we provide an exact treatment, that takes into account the energy shifts and couplings arising from the (fast rotating) qubit-cavity coupling term. For $g^x = 0$, the Hamiltonian H can be diagonalized exactly, yielding the eigenstates $|\sigma\rangle \otimes D^\dagger(\sigma\frac{g^z}{\omega_c})|n\rangle$ with the corresponding eigenenergies $\epsilon(\sigma,n) = \sigma\omega_q/2 - g_z^2/\omega_c + n\omega_c$, with $\sigma = \pm$ for spin up and spin down, respectively, the displacement operator $D(\alpha) = \exp[\alpha a^\dagger - \alpha^* a]$ and $|n\rangle$ denoting the usual Fock states. This treatment can be extended straightforwardly to more than one qubit.

While the analysis above has focused on a single charge qubit, in the following we consider *two* qubits of this type, coupled to a common resonator mode. Then, for two qubits and purely longitudinal spin-resonator coupling, in the presence of a nonzero (and potentially large, $\omega_q \sim |\epsilon|$) level splitting ω_q the time evolution generated by the Hamiltonian H reads as

$$U(t_m) = e^{-iHt_m} = e^{-i\frac{\omega_q}{2}S^z t_m}U_{\rm id}^z(t_m), \quad \text{(D8)}$$

with the ideal evolution $U_{\rm id}^z(t_m) = \exp[i4\pi m\mu^2\sigma_1^z\sigma_2^z]$, up to an irrelevant global phase. Therefore, in the regime $|\epsilon| \gg t_c$, a general two-qubit state $|\Psi_{2q}\rangle = c_{00}|\Downarrow\Downarrow\rangle + c_{01}|\Downarrow\Uparrow\rangle + c_{10}|\Uparrow\Downarrow\rangle + c_{11}|\Uparrow\Uparrow\rangle$ evolves as

$$U(t_m)\big|\Psi_{2q}\big\rangle = e^{+2im\pi\frac{\omega_q}{\omega_c}}c_{00}|\Downarrow\Downarrow\rangle + e^{-2im\pi\frac{\omega_q}{\omega_c}}c_{11}|\Uparrow\Uparrow\rangle + e^{-8im\pi\mu^2}(c_{01}|\Downarrow\Uparrow\rangle + c_{10}|\Uparrow\Downarrow\rangle). \quad \text{(D9)}$$

When tuning the qubit-level splitting on resonance ($\omega_q \approx |\epsilon| = \omega_c$), such that $\exp[\pm 2im\pi\omega_q/\omega_c] = 1$ for all $m = 1,2,3\ldots$, for certain times $t^\star = 2\pi m^\star/\omega_c = \pi/2g_{\rm eff}$, this unitary returns the original state since $U_{\rm id}^z(t^\star) = \mathbb{1}$ and, therefore, absent any other noise sources, leaves the (typically entangled) state prepared by the first step (i) with $g^x = g_{\rm ch}$, $g^z = 0$ unaffected; recall that $\mu = g_{\rm ch}/\omega_c = \frac{1}{4}, \frac{1}{8}, \ldots$ is chosen commensurately. While this statement holds for any two-qubit state $|\Psi_{2q}\rangle$, this effect becomes even simpler to see when the qubits are initialized in any of the four computational basis states $\{|\sigma,\sigma'\rangle\}$. Here, the ideal transversal gate (i) first prepares maximally entangled states, according to

$$|\Downarrow,\Downarrow\rangle \to \frac{1}{\sqrt{2}}(|\Downarrow,\Downarrow\rangle + i|\Uparrow\Uparrow\rangle), \quad \text{(D10)}$$

$$|\Uparrow,\Uparrow\rangle \to \frac{1}{\sqrt{2}}(|\Uparrow\Uparrow\rangle + i|\Downarrow,\Downarrow\rangle), \quad \text{(D11)}$$

$$|\Uparrow,\Downarrow\rangle \to \frac{1}{\sqrt{2}}(|\Uparrow,\Downarrow\rangle + i|\Downarrow\Uparrow\rangle), \quad \text{(D12)}$$

$$|\Downarrow,\Uparrow\rangle \to \frac{1}{\sqrt{2}}(|\Downarrow\Uparrow\rangle + i|\Uparrow,\Downarrow\rangle), \quad \text{(D13)}$$

which subsequently in stage (ii) where ($g^x = 0, g^z = g_{\rm ch}$) are left invariant $\forall\, m = 1,2,\ldots$; Eqs. (D12) and (D13) even hold independently of ω_q.

The charge-qubit-based scheme discussed above can be extended to (switchable) coupling between the resonator mode and the electron' s spin, by making use of various mechanisms which hybridize spin and charge degrees of freedom, as provided by spin-orbit interaction or inhomogeneous magnetic fields [29,30,41,43]. Such an implementation that easily generalizes to N qubits and would allow to fully turn off any coupling to the cavity mode (and to do so selectively for any chosen subset of qubits) is discussed in the next section.

2. Double quantum dot spin qubit

Let us now extend our treatment to singlet-triplet *spin* qubits in quantum dots, where logical qubits are encoded in a two-dimensional subspace of a higher-dimensional two-electron spin system, as investigated theoretically and experimentally (for example) in Refs. [60,61]. This approach successfully combines spin and charge manipulation, making use of the very long coherence times associated with spin states and, at the same time, enabling efficient readout and coherent manipulation of coupled spin states based on intrinsic interactions [27].

In contrast to the charge qubit setting discussed above (where the electron's charge will always couple to the resonator mode with the type of coupling depending on the particular parameter regime), in this setting the coupling to the cavity mode can be turned off completely since the dipole moment associated with the singlet-triplet qubit (which in this case determines the spin-resonator coupling) vanishes in the so-called (1,1) regime; here, (m,n) refers to a configuration with $m(n)$ electrons in the left (right) dot, respectively.

We focus on the typical regime of interest, where (following the standard notation) the relevant electronic levels are given by the triplet states $|T_+\rangle = |\Uparrow\Uparrow\rangle$, $|T_-\rangle = |\Downarrow\Downarrow\rangle$, and $|T_0\rangle = (|\Uparrow\Downarrow\rangle + |\Downarrow\Uparrow\rangle)/\sqrt{2}$, as well as the singlet states $|S_{11}\rangle = (|\Uparrow\Downarrow\rangle - |\Downarrow\Uparrow\rangle)/\sqrt{2}$ and $|S_{02}\rangle = d^\dagger_{R\uparrow} d^\dagger_{R\downarrow}|0\rangle$ with $|\sigma\sigma'\rangle = d^\dagger_{L\sigma} d^\dagger_{R\sigma'}|0\rangle$; the fermionic creation (annihilation) operators $d^\dagger_{i\sigma}$ ($d_{i\sigma}$) create (annihilate) an electron with spin $\sigma = \uparrow,\downarrow$ in the orbital $i = L,R$. For sufficiently large magnetic field B, the levels $|T_+\rangle$ and $|T_-\rangle$ are far detuned and can be neglected for the remainder of the discussion. Therefore, in the following, we restrict ourselves to the subspace $\{|T_0\rangle, |S_{11}\rangle, |S_{02}\rangle\}$, as schematically depicted in the inset of Fig. 8. In the relevant regime of interest, the electronic DQD system is described by the Hamiltonian [27]

$$H_{\rm DQD} = \frac{t_c}{2}(|S_{02}\rangle\langle S_{11}| + \text{H.c.}) + \Delta(|T_0\rangle\langle S_{11}| + \text{H.c.}) - \epsilon|S_{02}\rangle\langle S_{02}|, \tag{D14}$$

where (as before) t_c refers to the interdot tunneling amplitude, ϵ is the interdot detuning parameter, and Δ is a static magnetic field gradient between the two dots which couples singlet and triplet states. State preparation, measurement, single-qubit gates, and local two-qubit gates can be achieved by tuning the bias ϵ [60]. Tunnel coupling between the singlet states $|S_{11}\rangle$ with (1,1) charge occupation and $|S_{02}\rangle$ with (0,2) charge occupation [here, (m,n) refers to a configuration with m (n) electrons in the left (right) dot, respectively] yields the hybridized singlet states $|S_\pm\rangle$, given by

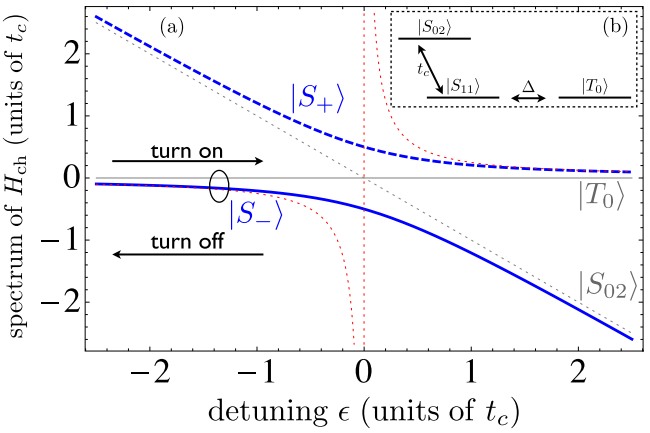

FIG. 8. (a) Spectrum of the DQD Hamiltonian in the two-electron regime, as given in Eq. (D14), as a function of the interdot detuning parameter ϵ for $\Delta = 0$. Tunnel coupling between the singlet states $|S_{11}\rangle$ with (1,1) charge occupation and $|S_{02}\rangle$ with (0,2) charge occupation yields the hybridized singlet states $|S_\pm\rangle$. The ellipse refers to the qubit subspace, spanned by $|T_0\rangle$ and $|S_-\rangle$, while the dotted line (red) refers to the effective exchange coupling $J(\epsilon) = t_c^2/4\epsilon$. The arrows indicate schematically how to turn on and off the effective spin-resonator coupling, by changing the effective dipole moment associated with the qubit. Inset (b): relevant level diagram in the subspace $\{|T_0\rangle, |S_{11}\rangle, |S_{02}\rangle\}$.

$$|S_+\rangle = \cos\theta|S_{11}\rangle + \sin\theta|S_{02}\rangle, \tag{D15}$$

$$|S_-\rangle = -\sin\theta|S_{11}\rangle + \cos\theta|S_{02}\rangle, \tag{D16}$$

with $\tan\theta = t_c/(\epsilon + \Omega)$, $\Omega = \sqrt{\epsilon^2 + t_c^2}$ and the associated eigenenergies $\epsilon_\pm = 1/2(-\epsilon \pm \sqrt{\epsilon^2 + t_c^2})$. For large, negative detuning values ($|\epsilon| \gg t_c$), the splitting between the triplet $|T_0\rangle$ and the hybridized singlet $|S_-\rangle$ can be approximated very well by the effective (tunable) exchange splitting $J(t_c,\epsilon) = t_c^2/4\epsilon$; compare Fig. 8. As schematically denoted by the ellipse in Fig. 8, we focus on the regime where the singlet $|S_+\rangle$ is far off resonance, yielding the effective qubit subspace $\{|T_0\rangle, |S_-\rangle\}$ with a qubit-level splitting $\omega_q \approx J(t_c,\epsilon)$.

Again, we consider a resonator with a single relevant mode of frequency ω_c, as modeled by the Hamiltonian

$$H_{\rm cav} = \omega_c a^\dagger a. \tag{D17}$$

In order to couple the electric field associated with the resonator mode to the electron spin states, the essential idea is to make use of an effective electric dipole moment associated with the exchange-coupled spin states of the DQD [27]. The resonator mode interacts capacitively with the double quantum dot [27], as described by the interaction Hamiltonian $H_I = g_0|S_{02}\rangle\langle S_{02}| \otimes (a + a^\dagger)$. Projection onto the electronic low-energy subspace $\{|T_0\rangle, |S_-\rangle\}$ (i.e., projecting out the high-energy level $|S_+\rangle$) then leads (to lowest order in $\sim g_0/\epsilon_+$) to

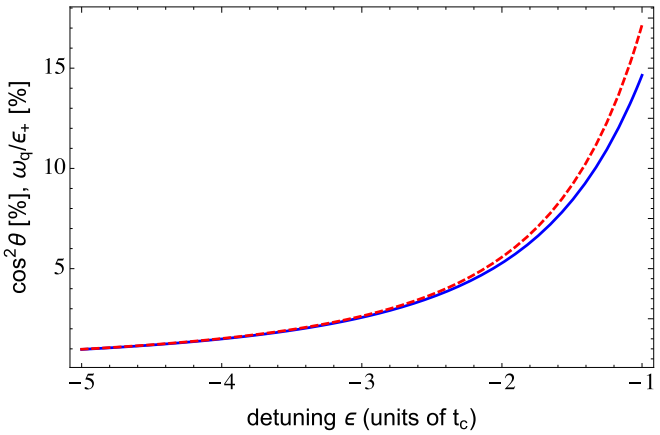

FIG. 9. Effective spin-resonator coupling $g_{\rm sp}/g_0 = \cos^2\theta$ (solid blue line) and qubit-level splitting $\omega_q \approx |J|$ relative to ϵ_+ (dashed red line) as a function of the interdot detuning parameter ϵ. The spin-resonator coupling may reach a few percent of the bare charge-resonator coupling g_0, with a qubit frequency ω_q that is much smaller than the energy of the level $|S_+\rangle$.

the effective spin-resonator system

$$H = J|S_-\rangle\langle S_-| - \Delta\sin\theta(|T_0\rangle\langle S_-| + \text{H.c.}) + \omega_c a^\dagger a + g_0\cos^2\theta|S_-\rangle\langle S_-|\otimes(a+a^\dagger), \tag{D18}$$

which includes a tunable spin-resonator coupling, explicitly given by

$$g_{\rm sp}/g_0 = \cos^2\theta = \frac{1}{2}\left(1 + \frac{\epsilon}{\sqrt{\epsilon^2+t_c^2}}\right). \tag{D19}$$

As demonstrated in Fig. 9, the effective coupling $g_{\rm sp}$ may be turned on and off by sweeping the detuning parameter ϵ (closely following the functional dependence of ω_q/ϵ_+), i.e., by controlling the admixture of $|S_{02}\rangle$ to the hybridized singlet level $|S_-\rangle$. For large, negative values of ϵ this admixture vanishes ($\cos^2\theta \to 0$), such that the effective dipole moment associated with the qubit vanishes and therefore the spin-resonator coupling is switched off. The type of spin-resonator coupling (transversal versus longitudinal) may be controlled by the magnetic gradient Δ, as can be done using, e.g., a nanomagnet or nuclear Overhauser fields [43,60]. While for longitudinal spin-resonator coupling the resonator frequency ω_c may be comparable or even smaller than the effective qubit-level splitting J (see Appendix H for details), in the case of transversal coupling the effective qubit-level splitting needs to be much smaller than the cavity frequency, that is $|J(t_c,\epsilon)| \approx |t_c^2/4\epsilon| \ll \omega_c$, but, at the same time, $\epsilon_+ \approx |\epsilon| + t_c^2/4|\epsilon| \gg \omega_c$ should be fulfilled in order to neglect the high-energy level $|S_+\rangle$. Still, both requirements can be satisfied by choosing the parameters as $t_c, \omega_c \ll |\epsilon|$.

APPENDIX E: SPIN-SPIN COUPLING IN DISPERSIVE REGIME

We consider two identical spins homogeneously coupled to a common resonator mode. The dynamics is assumed to be governed by the Jaynes-Cummings Hamiltonian

$$H = \Delta\left(S_1^z + S_2^z\right) + g[a(S_1^+ + S_2^+) + a^\dagger(S_1^- + S_2^-)], \tag{E1}$$

which is valid within the rotating-wave approximation for $\sqrt{\bar{n}_{\rm th}}g, \Delta \ll \omega_c$, with the detuning $\Delta = \omega_q - \omega_c$. In the following, we consider the *dispersive regime*, where the spin-resonator coupling is strongly detuned ($\sqrt{\bar{n}_{\rm th}}g \ll \Delta$). In this regime, the spin-resonator coupling can be treated perturbatively. To stress the perturbative treatment we write

$$H = H_0 + H_1, \tag{E2}$$

$$H_0 = \Delta S^z, \tag{E3}$$

$$H_1 = g(aS^+ + a^\dagger S^-), \tag{E4}$$

where $S^\alpha = S_1^\alpha + S_2^\alpha$ (for $\alpha = \pm, z$) are collective spin operators. We perform a standard Schrieffer-Wolff transformation

$$\tilde{H} = e^A H e^{-A} \tag{E5}$$

$$\approx H_0 + H_1 + [A, H_0 + H_1] + \tfrac{1}{2}[A,[A,H_0]], \tag{E6}$$

where the operator A (with $A^\dagger = -A$) is assumed to have a perturbative expansion in g, i.e., $A = 0 + O(g) + \ldots$ By choosing

$$[A, H_0] = -H_1, \tag{E7}$$

one obtains a Hamiltonian $\tilde{H}$ without linear coupling in g,

$$\tilde{H} \approx H_0 + \tfrac{1}{2}[A, H_1]. \tag{E8}$$

For the Hamiltonian given in Eq. (E2), the condition in Eq. (E7) is fulfilled by the choice

$$A = \frac{g}{\Delta}(aS^+ - a^\dagger S^-), \tag{E9}$$

which yields the Hamiltonian

$$\tilde{H} \approx \left(\Delta + \frac{g^2}{\Delta} + 2\frac{g^2}{\Delta}a^\dagger a\right)S^z + \frac{g^2}{\Delta}(S_1^+ S_2^- + S_1^- S_2^+). \tag{E10}$$

Here, the last two terms describe a cavity-state-dependent dispersive shift of the qubit transition frequencies and spin-spin coupling via virtual occupation of the cavity mode, respectively. The strength of the effective spin-spin coupling is given by

$$g_{\rm eff} = \frac{g^2}{\Delta} = \frac{\epsilon}{\sqrt{\bar{n}_{\rm th}}}g, \tag{E11}$$

where we have set $\sqrt{\bar{n}_{\rm th}}g/\Delta = \epsilon \ll 1$ in order to reach the regime of validity for Eq. (E10), given by

$$\sqrt{\bar{n}_{\rm th}}g \ll \Delta \ll \omega_c. \tag{E12}$$

By transforming the Hamiltonian given in Eq. (E10) back into the laboratory frame, we recover the result presented in Ref. [25], namely,

$$H \approx \left[\omega_c + 2\frac{g^2}{\Delta}\left(S_1^z + S_2^z\right)\right]a^\dagger a + \left(\omega_q + \frac{g^2}{\Delta}\right)\left(S_1^z + S_2^z\right) + \frac{g^2}{\Delta}(S_1^+ S_2^- + S_1^- S_2^+). \tag{E13}$$

Here, spins and cavity mode are still coupled by the ac Stark shift term $\sim a^\dagger a$. Accordingly, one obtains an effective pure spin Hamiltonian with flip-flop interactions provided that one can neglect any fluctuations of the photon number $a^\dagger a \to \bar{n} = \langle a^\dagger a \rangle$, where $\bar{n}$ is the average number of photons in the cavity mode [30].

Since the operator $S^z a^\dagger a$ in Eq. (E10) has an integer spectrum, one may wonder whether for stroboscopic times the spins disentangle from the resonator mode here as well. Thus, let us consider the full time evolution generated by Eq. (E1):

$$e^{-iHt} = e^{-iU^\dagger \tilde{H} U t} = U^\dagger e^{-i\tilde{H}t} U \tag{E14}$$

$$\approx U^\dagger \{\exp[-it(\delta + \tilde{\delta} a^\dagger a) S^z - i\tilde{g}t(S_1^+ S_2^- + S_1^- S_2^+)]\} U, \tag{E15}$$

with $U = \exp(A)$, $\delta = \Delta + g^2/\Delta$, $\tilde{\delta} = 2g^2/\Delta$, and $\tilde{g} = g^2/\Delta$. Note that Eq. (E15) is an approximate statement, relying on a perturbative expansion in the coupling g. Since the flip-flop interaction conserves S^z, we find

$$e^{-iHt} \approx U^\dagger e^{-i\delta t S^z} e^{-i\tilde{\delta} t S^z a^\dagger a} e^{-i\tilde{g}t(S_1^+ S_2^- + S_1^- S_2^+)} U. \tag{E16}$$

For stroboscopic times $\tilde{\delta} t = 2\pi m$, $e^{-i\tilde{\delta} t S^z a^\dagger a} = \mathbb{1}$, yielding

$$e^{-iHt} \approx U^\dagger e^{-iH_{\rm spin} t} U, \tag{E17}$$

where $H_{\rm spin} = \delta S^z + \tilde{g}(S_1^+ S_2^- + S_1^- S_2^+)$ is a pure spin Hamiltonian, without any coupling to the resonator mode. However, in contrast to our scheme presented in the main text, the full time evolution does not reduce to a pure spin problem since the Schrieffer-Wolff transformation $U = \exp[\frac{g}{\Delta}(aS^- - a^\dagger S^+)]$ does not commute with $e^{-iH_{\rm spin}t}$, but rather entangles the qubits with the resonator mode.

APPENDIX F: SCHRIEFFER-WOLFF TRANSFORMATION

If one restricts oneself to the regime $g \ll \omega_c$, the result stated in Eq. (6) may also be derived in the perturbative framework of a Schrieffer-Wolff transformation. For concreteness, assuming $\omega_q = 0$, we consider the Hamiltonian

$$H = \underbrace{\omega_c a^\dagger a}_{H_0} + \underbrace{g S^x \otimes (a + a^\dagger)}_{V}, \tag{F1}$$

where $S^x = \sum_i \eta_i^x \sigma_i^x$ is a collective operator. In the following, and contrary to our general analysis in the main text, we restrict ourselves to the regime where the spin-resonator coupling V can be treated perturbatively with respect to H_0, that is $g \ll \omega_c$. Performing a Schrieffer-Wolff transformation $\tilde{H} = e^A H e^{-A}$ as presented in Appendix E, with $A = -\frac{g}{\omega_c} S^x (a - a^\dagger)$, we obtain an effective Hamiltonian $\tilde{H}$ where the slow subspace is decoupled from the fast subspace up to second order in g. Explicitly, it reads as [compare Eq. (5)]

$$\tilde{H} \approx \omega_c a^\dagger a - \frac{g^2}{\omega_c} S_x^2. \tag{F2}$$

APPENDIX G: NONZERO QUBIT-LEVEL SPLITTING

In our derivation of Eq. (5), starting from the generic spin-resonator Hamiltonian given in Eq. (1), we have assumed $\omega_q = 0$. As demonstrated also numerically in Appendix K below, small level splittings with $\omega_q \approx 0.1\omega_c$ may still be tolerated without a significant loss in the amount of generated entanglement and the fidelity with the maximally entangled target state.

In this appendix, we investigate analytically the effects associated with a finite splitting $\omega_q > 0$. In this case, Eq. (3) can be generalized straightforwardly to

$$H = U\Big[\underbrace{\omega_c a^\dagger a - \frac{g^2}{\omega_c}\mathcal{S}^2}_{H_0} + \frac{\omega_q}{2}\tilde{S}^z\Big]U^\dagger, \tag{G1}$$

where $\tilde{S}^z = U^\dagger S^z U$, with $U = \exp[\frac{g}{\omega_c}\mathcal{S}(a - a^\dagger)]$. In what follows, we restrict ourselves to the (experimentally) most relevant regime where $\mu = g/\omega_c \ll 1$, which allows for a simple perturbative treatment. Expansion in the small parameter μ yields

$$\tilde{S}^z \approx S^z - \mu(a - a^\dagger)[\mathcal{S}, S^z] + \frac{\mu^2}{2}(a - a^\dagger)^2[\mathcal{S},[\mathcal{S}, S^z]]. \tag{G2}$$

Specifically, for $\mathcal{S} = \sum_i \sigma_i^x$ (as considered in the main text) we then obtain

$$\tilde{S}^z \approx S^z + 2i\frac{g}{\omega_c} S^y (a - a^\dagger) + 2\left(\frac{g}{\omega_c}\right)^2 S^z (a - a^\dagger)^2, \tag{G3}$$

which leads to an additional (undesired) contribution in Eq. (G1) of the form

$$\frac{\omega_q}{2}\tilde{S}^z \approx \frac{\omega_q}{2} S^z + \epsilon\left[i g S^y (a - a^\dagger) + \frac{g^2}{\omega_c} S^z (a - a^\dagger)^2\right]. \tag{G4}$$

Here, in contrast to the ideal Hamiltonian H_0 in Eq. (G1) the spins are not decoupled from the (hot) resonator mode. However, apart from being detuned by at least $\omega_c - \omega_q$, the undesired terms, that lead to entanglement of the spins with the (hot) resonator mode, are suppressed by the small parameter $\epsilon = \omega_q/\omega_c \ll 1$. In the limit $\omega_q \to 0$ ($\epsilon \to 0$), we recover the ideal dynamics.

APPENDIX H: ERRORS DUE TO NONZERO QUBIT-LEVEL SPLITTING

In this Appendix, we analyze errors induced by a nonzero qubit-level splitting ($\omega_q/\omega_c > 0$). In the case of longitudinal spin-resonator coupling, we show that controlled phase gates can be implemented (as described in the main text for $\omega_q = 0$), even in the presence of nonzero and inhomogeneous qubit-level splittings ($\omega_q > 0$), when applying either fast local single-qubit gates (to correct the effect of known $\omega_q \neq 0$) or standard spin-echo techniques (to compensate unknown detunings); see Appendix H 1. Therefore, for longitudinal spin-resonator coupling, our approach yields a high-fidelity hot gate, that is *independent* of the qubit-level splitting $\omega_q/\omega_c \geqslant 0$. As detailed in Appendix H 2, this is not the case for transversal coupling, where $\omega_q \neq 0$ causes second-order errors, which, however, are suppressed in certain decoherence-free subspaces. Thus, as opposed to the limiting regime where $\omega_q = 0$, the distinction between longitudinal and transversal spin-resonator coupling indeed becomes meaningful.

The model. In the absence of other error sources ($\kappa = \Gamma = 0$), the system's dynamics is governed by the Hamiltonian

$$H = H_0 + V, \tag{H1}$$

$$H_0 = \omega_c a^\dagger a + g\mathcal{S} \otimes (a + a^\dagger), \tag{H2}$$

$$V = \frac{\omega_q}{2} S^z, \tag{H3}$$

with $S^z = \sum_i \sigma_i^z$ and $\mathcal{S} = \sum_{i,\alpha} \eta_i^\alpha \sigma_i^\alpha$. Below, we will set $S^\alpha = S_\alpha$ ($\alpha = x,z$) interchangeably. Also, note that S^x, S^z as defined here refer to the usual spin operators multiplied by 2.

1. Longitudinal spin-resonator coupling

Controlled phase gate. Let us first focus on the case of longitudinal spin-resonator coupling, where $\mathcal{S} = \sum_i \sigma_i^z = S^z$ and accordingly $[H_0, V] = 0$. In this scenario, controlled phase gates can be implemented (as described in the main text for $\omega_q = 0$), even in the presence of nonzero qubit-level splittings ($\omega_q > 0$), when applying either fast local single-qubit phase gates (to correct the effect of known $\omega_q \neq 0$) or standard spin-echo techniques (to compensate unknown detunings). By flipping the qubits (for example) halfway the evolution and at the end of the gate, the effect of V is canceled exactly. Denoting such a global flip of all qubits around the axis $\alpha = x,y,z$ as $U_\alpha(\varphi) = \exp[-i\varphi/2\sigma_1^\alpha] \ldots \exp[-i\varphi/2\sigma_N^\alpha] = \exp[-i\varphi/2 \sum \sigma_i^\alpha]$, for two qubits the full evolution (in the computational basis $\{|00\rangle, |10\rangle, |01\rangle, |11\rangle\}$), intertwined by spin-echo pulses, reads as

$$U(2t_m) = U_x(\pi) e^{-iHt_m} U_x(\pi) e^{-iHt_m} \tag{H4}$$

$$= \mathrm{diag}(e^{i\phi}, 1, 1, e^{i\phi}), \tag{H5}$$

with $\phi = 16 m \pi \mu^2$. The gate $U(2t_m)$ is independent of the resonator mode and, as a consequence of the spin-echo π pulses $U_x(\pi)$, independent of ω_q; accordingly, the qubit-level splittings do not have to be necessarily small. When complementing the propagator $U(2t_m)$ with local unitaries, such that $|0\rangle_i \to e^{-i\phi/2}|0\rangle_i$ and $|1\rangle_i \to e^{i\phi/2}|1\rangle_i$, we obtain

$$U_{\mathrm{Cphase}} = U_z(-\phi) U_x(\pi) e^{-iHt_m} U_x(\pi) e^{-iHt_m} \tag{H6}$$

$$= \mathrm{diag}(1, 1, 1, e^{2i\phi}), \tag{H7}$$

which yields a controlled phase gate for $\phi = \pi/2$ (corresponding to a gate time $t_{\max} = \pi/16 g_{\mathrm{eff}}$), that is insensitive to the qubit-level splittings $\omega_q > 0$.

For longitudinal spin-resonator coupling, Eq. (5) of the main text simply reads as

$$e^{-iHt_m} = \exp[i 2\pi m \mu^2 \tilde{\mathcal{S}}^2], \tag{H8}$$

with (the generalized expression) $\tilde{\mathcal{S}}^2 = \mathcal{S}^2 - (\omega_q/2g_{\mathrm{eff}}) S^z$, where $\mathcal{S} = \sum_i \eta_i \sigma_i^z$, while the operator S^z can also be generalized to account for possible inhomogeneities in the qubit-level splittings (with $\omega_{q,i} = \delta_i \omega_q$), i.e., $S^z \to \sum \delta_i \sigma_i^z$. This gate differs from the ideal one ($\exp[i 2\pi m \mu^2 \mathcal{S}^2]$) only by the local phases $\exp[-i t_m (\omega_q/2) S^z]$ and thus has the same computational power.

2. Transversal spin-resonator coupling

Transversal spin-resonator coupling. In the following, we turn to systems with transversal spin-resonator coupling, where $\mathcal{S} = S^x = \sum_i \sigma_i^x$. In this case, the theoretical treatment is more involved as compared to our previous discussion on longitudinal spin-resonator coupling because the ideal free evolution does not commute with the perturbation ($[H_0, V] \neq 0$). We use perturbative techniques to derive an analytic expression for the error ξ_q induced by nonzero qubit splittings $\omega_q > 0$. For the sake of readability, here we restrict ourselves to two qubits, while our analysis can be generalized readily to more than two qubits.

Perturbative series. Up to second order in the perturbation V, the unitary evolution operator associated with H is approximately given by

$$U(t) \approx e^{-iH_0 t} \Big[\mathbb{1} - i \int_0^t d\tau\, \tilde{V}(\tau) - \int_0^t d\tau_2 \int_0^{\tau_2} d\tau_1 \tilde{V}(\tau_2) \tilde{V}(\tau_1) \Big], \tag{H9}$$

with

$$\tilde{V}(\tau) = e^{iH_0\tau} V e^{-iH_0\tau}. \tag{H10}$$

Initially, the resonator mode is assumed to be in a thermal state $\rho_{\mathrm{th}} = \rho_{\mathrm{th}}(T) = Z^{-1} \exp[-\beta \omega_c a^\dagger a]$. Then, starting from the initial state $\rho(0) = \varrho(0) \otimes \rho_{\mathrm{th}}$, the system (comprising both spin and resonator degrees of freedom) evolves as

$$\rho(t) = U(t) \varrho(0) \rho_{\mathrm{th}} U^\dagger(t). \tag{H11}$$

Inserting the perturbative expansion given in Eq. (H9), up to second order in V we obtain

$$\rho(t) \approx e^{-iH_0 t} \Big\{ \rho(0) - i \int_0^t d\tau [\tilde{V}(\tau), \rho(0)] + \int_0^t d\tau \int_0^t d\tau' \tilde{V}(\tau) \rho(0) \tilde{V}(\tau') - \int_0^t d\tau_2 \int_0^{\tau_2} d\tau_1 \tilde{V}(\tau_2) \tilde{V}(\tau_1) \rho(0) - \int_0^t d\tau_2 \int_0^{\tau_2} d\tau_1 \rho(0) \tilde{V}(\tau_1) \tilde{V}(\tau_2) \Big\} e^{iH_0 t}. \tag{H12}$$

Eigensystem of unperturbed Hamiltonian. In the first step, it it instructive to find the eigensystem of H_0. Following the same strategy as outlined in the main text, H_0 can be written as

$$H_0 = D^\dagger(\mu S^x) \big[\omega_c a^\dagger a - g_{\mathrm{eff}} S_x^2 \big] D(\mu S^x), \tag{H13}$$

where $\mu = g/\omega_c$, $g_{\mathrm{eff}} = g^2/\omega_c = \mu^2 \omega_c$ and $D(\alpha) = \exp[\alpha a^\dagger - \alpha^* a]$ is a displacement operator. Accordingly, the eigensystem of H_0 is found to be

$$H_0 \widetilde{|n, \vec{\sigma}_x\rangle} = E_{n,s} \widetilde{|n, \vec{\sigma}_x\rangle}, \tag{H14}$$

where the eigenvectors are given by product states of spins aligned along the transversal direction x and displaced resonator states with a displacement proportional to the total spin projection s along x,

$$\widetilde{|n, \vec{\sigma}_x\rangle} = D^\dagger(\mu s) |n\rangle \otimes |\vec{\sigma}_x\rangle, \tag{H15}$$

with $s = s_1^x + s_2^x$, $S^x|\vec{\sigma}_x\rangle = (s_1^x + s_2^x)|\vec{\sigma}_x\rangle$ and $|n\rangle$ denoting the usual Fock states. The corresponding eigenenergies

$$E_{n,s} = n\omega_c - s^2 g_{\text{eff}} \tag{H16}$$

refer to manifolds with fixed resonator excitation number $n = 0,1,2,\ldots$ and two-qubit spin states with a resonator-induced splitting of $4g_{\text{eff}}$ between the states $\{|\uparrow_x,\downarrow_x\rangle,|\downarrow_x,\uparrow_x\rangle\}$ with $s^2 = 0$ and $\{|\uparrow_x,\uparrow_x\rangle,|\downarrow_x,\downarrow_x\rangle\}$ with $s^2 = 4$, respectively.

Perturbation in the interaction picture. In the following, we focus on the perturbative regime where the perturbation $\sim\omega_q$ is small compared to the resonator-induced splitting of S_x^2 eigenstates, that is, $\omega_q \ll 8g_{\text{eff}} = 8\mu^2\omega_c$. Rewriting the perturbation in the unperturbed eigenbasis yields

$$V = \sum_{n,n'}\sum_{\vec{\sigma},\vec{\sigma}'}\langle n'|D[\mu(s'-s)]|n\rangle\langle\vec{\sigma}_x'|V|\vec{\sigma}_x\rangle\widetilde{|n',\vec{\sigma}_x'\rangle}\widetilde{\langle n,\vec{\sigma}_x|}. \tag{H17}$$

Using the relation [62]

$$\langle m|D[\alpha]|n\rangle = \sqrt{\frac{n!}{m!}}\alpha^{m-n}e^{-|\alpha|^2/2}L_n^{(m-n)}(|\alpha|^2), \tag{H18}$$

with $L_n^{(m-n)}$ denoting the associated Laguerre polynominals, in the experimentally most relevant regime of weak spin-resonator coupling (that is, $\mu \ll 1$) we can neglect the off-diagonal contributions where $n \neq m$ since eigenstates with different boson number are very weakly coupled ($\sim\omega_q\mu^{|n-m|}$) and far off resonance ($\omega_q \ll 8g_{\text{eff}} \ll \omega_c$), with rapidly decaying contributions as the number difference increases. In this limit, the perturbation in the interaction picture [compare Eq. (H10)] reads as

$$\tilde{V}(\tau) \approx \tilde{V}_q(\tau)\otimes\sum_n \chi_n(\mu)|n\rangle\langle n|, \tag{H19}$$

$$\tilde{V}_q(\tau) = \frac{\omega_q}{2}[e^{i4g_{\text{eff}}\tau}Q + e^{-i4g_{\text{eff}}\tau}Q^\dagger], \tag{H20}$$

where

$$\chi_n(\mu) = \langle n|D[\pm 2\mu]|n\rangle = e^{-2\mu^2}L_n^{(0)}(4\mu^2). \tag{H21}$$

Since the perturbation $\sim S^z$ is purely off diagonal in the S^x eigenbasis, the operator

$$Q = |\uparrow_x\downarrow_x\rangle\langle\downarrow_x\downarrow_x| + |\downarrow_x\uparrow_x\rangle\langle\downarrow_x\downarrow_x| + |\uparrow_x\downarrow_x\rangle\langle\uparrow_x\uparrow_x| + |\downarrow_x\uparrow_x\rangle\langle\uparrow_x\uparrow_x| \tag{H22}$$

describes *only* transitions from the $s = \pm 2$ subspace to the $s = 0$ subspace (and vice versa for the Hermitian conjugate operator $Q^\dagger$), which in the interaction picture underlying Eq. (H20) rotate with the corresponding transition frequency $\pm 4g_{\text{eff}}$. While Eq. (H19) is purely off diagonal in spin space, in the limit $\mu \ll 1$ it is (approximately) diagonal in the excitation number $|n\rangle$, as the coupling V between different n subspaces is strongly detuned by the corresponding large energy splitting $\sim\omega_c$.

Quasidecoherence-free subspace. In our numerical simulations, the initial qubit states have been chosen to be aligned along the z direction, defining the computational basis states and corresponding to eigenstates of the perturbation $V \sim S^z$. Therefore, it is didactic to rewrite $\tilde{V}(\tau)$ in the eigenbasis of S^z. With $|\uparrow_x\rangle = (|\uparrow_z\rangle + |\downarrow_z\rangle)/\sqrt{2}$, and $|\downarrow_x\rangle = (|\uparrow_z\rangle - |\downarrow_z\rangle)/\sqrt{2}$, we obtain

$$Q = |\uparrow_z\uparrow_z\rangle\langle\uparrow_z\uparrow_z| - |\downarrow_z\downarrow_z\rangle\langle\downarrow_z\downarrow_z| + |\uparrow_z\uparrow_z\rangle\langle\downarrow_z\downarrow_z| - |\downarrow_z\downarrow_z\rangle\langle\uparrow_z\uparrow_z|. \tag{H23}$$

As can be seen readily from this expression, the subspace $\{|\uparrow_z\downarrow_z\rangle,|\downarrow_z\uparrow_z\rangle\}$ with $S^z = 0$ defines a decoherence-free subspace since Q and $Q^\dagger$ [and therefore $\tilde{V}(\tau)$] vanish on this subspace, with $Q|\uparrow_z\downarrow_z\rangle = Q|\downarrow_z\uparrow_z\rangle = 0$. In the following, this finding is elaborated in more detail: To do so, we first rewrite $\tilde{V}(\tau)$ as

$$\tilde{V}(\tau) = \frac{\omega_q}{2}D^\dagger(\mu S^x)e^{i\omega_c a^\dagger a\tau}e^{-ig_{\text{eff}}\tau S_x^2}D(\mu S^x)S^z \times D^\dagger(\mu S^x)e^{-i\omega_c a^\dagger a\tau}e^{ig_{\text{eff}}\tau S_x^2}D(\mu S^x). \tag{H24}$$

This expression is exact. Defining triplet and singlet states in the spin eigenbasis of H_0 as

$$|T_+^x\rangle = |\uparrow_x\uparrow_x\rangle, \tag{H25}$$

$$|T_0^x\rangle = (|\uparrow_x\downarrow_x\rangle + |\downarrow_x\uparrow_x\rangle)/\sqrt{2}, \tag{H26}$$

$$|T_-^x\rangle = |\downarrow_x\downarrow_x\rangle, \tag{H27}$$

$$|S^x\rangle = (|\uparrow_x\downarrow_x\rangle - |\downarrow_x\uparrow_x\rangle)/\sqrt{2}, \tag{H28}$$

the (by definition) computational basis states (taken as initial states in our numerical simulations) are given by

$$|\uparrow_z\uparrow_z\rangle = \tfrac{1}{2}[|T_+^x\rangle + \sqrt{2}|T_0^x\rangle + |T_-^x\rangle], \tag{H29}$$

$$|\uparrow_z\downarrow_z\rangle = \tfrac{1}{2}[|T_+^x\rangle - \sqrt{2}|S^x\rangle - |T_-^x\rangle], \tag{H30}$$

$$|\downarrow_z\uparrow_z\rangle = \tfrac{1}{2}[|T_+^x\rangle + \sqrt{2}|S^x\rangle - |T_-^x\rangle], \tag{H31}$$

$$|\downarrow_z\downarrow_z\rangle = \tfrac{1}{2}[|T_+^x\rangle - \sqrt{2}|T_0^x\rangle + |T_-^x\rangle]. \tag{H32}$$

For a general resonator state $|\text{cav}\rangle$, the first-order error term will be proportional to

$$\tilde{V}(\tau)|T_+^x\rangle|\text{cav}\rangle = \frac{\omega_q}{\sqrt{2}}e^{4ig_{\text{eff}}\tau}|T_0^x\rangle \otimes e^{i\omega_c a^\dagger a\tau}D^\dagger(2\mu)e^{-i\omega_c a^\dagger a\tau}D(2\mu)|\text{cav}\rangle, \tag{H33}$$

$$\tilde{V}(\tau)|T_0^x\rangle|\text{cav}\rangle = \frac{\omega_q}{\sqrt{2}}e^{-4ig_{\text{eff}}\tau}[|T_+^x\rangle\otimes D^\dagger(2\mu)e^{i\omega_c a^\dagger a\tau}D(2\mu)e^{-i\omega_c a^\dagger a\tau}|\text{cav}\rangle + |T_-^x\rangle\otimes D^\dagger(-2\mu)e^{i\omega_c a^\dagger a\tau}D(-2\mu)e^{-i\omega_c a^\dagger a\tau}|\text{cav}\rangle], \tag{H34}$$

$$\tilde{V}(\tau)|T_-^x\rangle|\text{cav}\rangle = \frac{\omega_q}{\sqrt{2}}e^{4ig_{\text{eff}}\tau}|T_0^x\rangle \otimes e^{i\omega_c a^\dagger a\tau}D^\dagger(-2\mu)e^{-i\omega_c a^\dagger a\tau}D(-2\mu)|\text{cav}\rangle, \tag{H35}$$

$$\tilde{V}(\tau)|S^x\rangle|\text{cav}\rangle = 0. \tag{H36}$$

In the spirit of our previous discussion [recall Eq. (H18) with $D^\dagger(\alpha) = D(-\alpha)$], these exact statements can be simplified in the limit $\mu \ll 1$ as

$$e^{i\omega_c a^\dagger a\tau} D^\dagger(\pm 2\mu) e^{-i\omega_c a^\dagger a\tau} = \sum_{n,n'} e^{i\omega_c \tau(n'-n)} \langle n'|D^\dagger(\pm 2\mu)|n\rangle |n'\rangle\langle n| \quad \text{(H37)}$$

$$\approx \sum_n \chi_n(\mu)|n\rangle\langle n|, \quad \text{(H38)}$$

yielding the approximate results [for a Fock state $|\text{cav}\rangle = |n\rangle$]

$$\tilde{V}(\tau)|T_+^x\rangle|n\rangle \approx \frac{\omega_q}{\sqrt{2}} e^{4ig_{\text{eff}}\tau} \chi_n^2(\mu)\big|T_0^x\big\rangle|n\rangle, \quad \text{(H39)}$$

$$\tilde{V}(\tau)\big|T_0^x\big\rangle|n\rangle \approx \frac{\omega_q}{\sqrt{2}} e^{-4ig_{\text{eff}}\tau} \chi_n^2(\mu)[|T_+^x\rangle + |T_-^x\rangle]|n\rangle, \quad \text{(H40)}$$

$$\tilde{V}(\tau)|T_-^x\rangle|n\rangle \approx \frac{\omega_q}{\sqrt{2}} e^{4ig_{\text{eff}}\tau} \chi_n^2(\mu)\big|T_0^x\big\rangle|n\rangle. \quad \text{(H41)}$$

With these (approximate) relations, one can readily verify $\tilde{V}(\tau)|\uparrow_z\downarrow_z\rangle|n\rangle \approx 0$ and $\tilde{V}(\tau)|\downarrow_z\uparrow_z\rangle|n\rangle \approx 0$, in agreement with our result based on Eq. (H23), while the subspace $\{|\uparrow_z\uparrow_z\rangle,|\downarrow_z\downarrow_z\rangle\}$ is directly affected by the perturbation $\tilde{V}(\tau)$. As long as transitions between different n subspaces can be neglected, the bosonic part of the Hamiltonian can be ignored and the free part of the Hamiltonian reduces to $H_0 \approx -g_{\text{eff}} S_x^2$. Then, since the perturbation $V = (\omega_q/2)S^z$ leaves the subspace $\{|\uparrow_z\downarrow_z\rangle,|\downarrow_z\uparrow_z\rangle\}$ invariant, V cannot induce errors since it vanishes on this subspace. As a perspective, this finding opens up the possibility to define a logical qubit in the quasidecoherence-free subspace $\{|\uparrow_z\downarrow_z\rangle,|\downarrow_z\uparrow_z\rangle\}$ as $|\text{qubit}\rangle = \alpha|\uparrow_z\downarrow_z\rangle + \beta|\downarrow_z\uparrow_z\rangle$, which is largely protected from splitting-induced errors in the limit $\mu \ll 1$ (provided that the perturbative condition $\omega_q \ll 8g_{\text{eff}}$ is still satisfied).

Splitting-induced error. Based on Eqs. (H12) and (H19), in the following we derive an approximate analytic expression for the splitting-induced error ξ_q. Taking the trace over the resonator mode, for stroboscopic times $t_m = 2\pi m/\omega_c$ (where the ideal evolution reduces to a pure spin gate, leaving the resonator mode unaffected) the fidelity $\mathcal{F}$ with the target qubit state $|\Psi_{\text{tar}}\rangle = \exp[-iH_0 t_m]|\Psi(0)\rangle$ is found to be

$$\mathcal{F}(t_m) = 1 - \langle\Psi_{\text{tar}}|\varrho^{(2)}(t_m)|\Psi_{\text{tar}}\rangle, \quad \text{(H42)}$$

where we have used that first-order terms vanish; moreover, we have introduced the second-order contribution

$$\varrho^{(2)} = -\Upsilon_q e^{-iH_0 t_m}\Big\{\int_0^{t_m} d\tau \int_0^{t_m} d\tau' \tilde{V}_q(\tau)\varrho(0)\tilde{V}_q(\tau') - \int_0^{t_m} d\tau_2 \int_0^{\tau_2} d\tau_1 \tilde{V}_q(\tau_2)\tilde{V}_q(\tau_1)\varrho(0) - \int_0^{t_m} d\tau_2 \int_0^{\tau_2} d\tau_1 \varrho(0)\tilde{V}_q(\tau_1)\tilde{V}_q(\tau_2)\Big\} e^{iH_0 t_m},$$

with $\varrho(0) = |\Psi(0)\rangle\langle\Psi(0)|$ and the prefactor

$$\Upsilon_q = \Upsilon_q(\mu, k_B T) = \frac{1}{Z}\sum_n e^{-\beta\omega_c n}\chi_n^2(\mu). \quad \text{(H43)}$$

The latter depends on both the spin-resonator coupling $\mu = g/\omega_c$ and temperature T (with $\beta = 1/k_B T$) and can be readily evaluated numerically. After some manipulations, we then arrive at an analytic expression for the error $\xi_q = 1 - \mathcal{F}(t_{\max})$ at the (nominally) optimal time $t_{\max} = \pi/8g_{\text{eff}}$. For $|\Psi(0)\rangle \in \{|\uparrow_z\uparrow_z\rangle,|\downarrow_z\downarrow_z\rangle\}$, it reads as explicitly

$$\xi_q = \Upsilon_q(\mu, k_B T)\frac{\omega_q^2}{16 g_{\text{eff}}^2} \quad \text{(H44)}$$

$$= \alpha_q \times (\omega_q/\omega_c)^2, \quad \text{(H45)}$$

showing a quadratic scaling with the splitting $\sim\omega_q^2$. In the last step, we have introduced the prefactor $\alpha_q = \Upsilon_q(\mu, k_B T)/(16\mu^4)$.

Numerical results. As shown in Fig. 10, we have numerically verified our analytical results (as discussed above): (i) The error ξ_q scales quadratically with the qubit splitting, i.e., $\xi_q \sim (\omega_q/\omega_c)^2$, with (ii) a numerical prefactor α_q depending on both the spin-resonator coupling g and temperature T, and (iii) (all other parameters equal) the error ξ_q is found to be significantly smaller for initial states in the quasidecoherence-free subspace $\{|\uparrow_z\downarrow_z\rangle,|\downarrow_z\uparrow_z\rangle\}$ than for initial qubit states in the orthogonal subspace $\{|\uparrow_z\uparrow_z\rangle,|\downarrow_z\downarrow_z\rangle\}$.

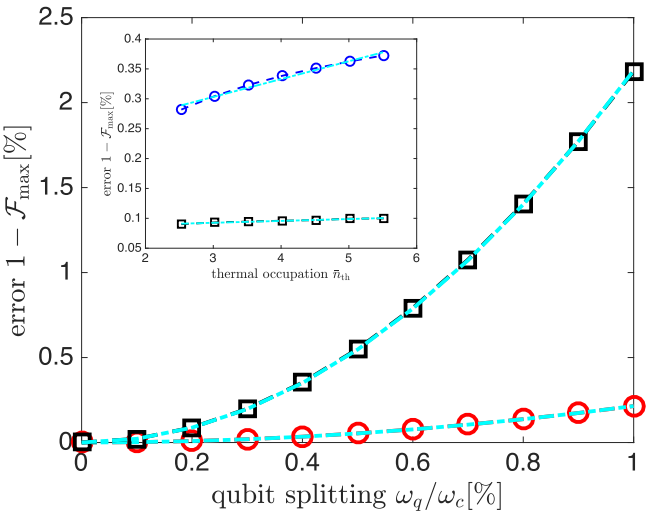

FIG. 10. The error ξ_q induced by a nonzero qubit splitting $\omega_q > 0$, for $\mathcal{S} = S^x = \sum_i \sigma_i^x$ (transversal coupling), and for different initial qubit states $|\Psi(0)\rangle = |\uparrow_z\downarrow_z\rangle$ (red circles) and $|\Psi(0)\rangle = |\downarrow_z\downarrow_z\rangle$ (black squares); here, $g/\omega_c = \frac{1}{8}$ and $k_B T/\omega_c = 1$. Quadratic fits (cyan, dashed-dotted lines) verify a quadratic error scaling $\sim\omega_q^2$, with the numerical pre-factor α_q depending on both the spin-resonator coupling g and temperature T. Inset: the error ξ_q as a function of the thermal occupation number $\bar{n}_{\text{th}}$ for $g/\omega_c = \frac{1}{8}$ (black squares) and $g/\omega_c = 1/(8\sqrt{2})$ (blue circles) for $|\Psi(0)\rangle = |\uparrow_z\downarrow_z\rangle$ and $\omega_q/\omega_c = 0.5\%$. Other numerical parameters: $\Gamma = \kappa = 0$.

APPENDIX I: SAW-BASED SPIN-RESONATOR SYSTEM

Here, we provide further details on how to implement experimental candidate systems governed by the class of Hamiltonians given in Eq. (1), using quantum dots embedded in high-quality surface acoustic wave (SAW) resonators [46,47]. For similar considerations based on (for example) transmission-line resonators or nanomechanical oscillators, we refer to Refs. [29] and [50], respectively.

Charge qubit. A single electron in a double quantum dot (DQD) coupled to a SAW resonator can be described by

$$H_{\text{charge}} = \frac{\epsilon}{2}\sigma^z + t_c\sigma^x + \omega_c a^\dagger a + g_{\text{ch}}\sigma^z \otimes (a + a^\dagger), \quad \text{(I1)}$$

where ϵ is the interdot detuning parameter, t_c the tunnel coupling between the dots, $g_{\text{ch}} = e\phi_0\mathcal{F}(kd)\sin(kl/2)$ the bare single-phonon coupling strength (assuming a sinelike mode function of the piezoelectric potential, with a node tuned between the two dots separated by a distance l), and the (orbital) Pauli operators are defined as $\sigma^z = |L\rangle\langle L| - |R\rangle\langle R|$ and $\sigma^x = |L\rangle\langle R| + |R\rangle\langle L|$, respectively [46]. In our expression for g_{ch}, e refers to the electron's charge, and ϕ_0 to the piezoelectric potential associated with a single SAW phonon; the decay of the SAW resonator mode into the bulk is captured by the factor $\mathcal{F}(kd)$, where d is the distance between the DQD and the surface and $k = 2\pi/\lambda_c$ the wave number of the resonator mode [46]. In the computational basis, where the dot Hamiltonian $H_{\text{dot}} = \frac{\epsilon}{2}\sigma^z + t_c\sigma^x$ is diagonal, with the electronic eigenstates

$$|+\rangle = \cos\theta|L\rangle + \sin\theta|R\rangle, \quad \text{(I2)}$$

$$|-\rangle = -\sin\theta|L\rangle + \cos\theta|R\rangle, \quad \text{(I3)}$$

where the mixing angle is given by $\tan\theta = 2t_c/(\epsilon + \Omega)$, $\Omega = \sqrt{\epsilon^2 + 4t_c^2}$, the spin-resonator Hamiltonian given in Eq. (I1) can be rewritten as

$$H_{\text{charge}} = \frac{\Omega}{2}S^z + \omega_c a^\dagger a + g^x S^x \otimes (a + a^\dagger) + g^z S^z \otimes (a + a^\dagger), \quad \text{(I4)}$$

where the Pauli operators in the logical qubit basis are $S^z = (|+\rangle\langle+| - |-\rangle\langle-|)$, $S^x = (|+\rangle\langle-| + |-\rangle\langle+|)$ and

$$g^x = g_{\text{ch}}\frac{2t_c}{\Omega}, \quad \text{(I5)}$$

$$g^z = -g_{\text{ch}}\frac{\epsilon}{\Omega}. \quad \text{(I6)}$$

In the last step, we have made use of the relations $2\sin\theta\cos\theta = \sin(2\theta) = 2t_c/\Omega$ and $\cos^2\theta - \sin^2\theta = \cos(2\theta) = \epsilon/\Omega$. In the limit where $\delta, g_{\text{ch}} \ll \omega_c$, with $\delta = \Omega - \omega_c$, one can perform a rotating-wave approximation yielding the standard Jaynes-Cummings Hamiltonian [35]. Finally, the spin-resonator Hamiltonian given in Eq. (I4) belongs to the general class of Hamiltonians defined in Eq. (1). In particular, at the charge degeneracy point $\epsilon = 0$, where $\sin\theta = \cos\theta = 1/\sqrt{2}$, the Hamiltonian given in Eq. (I4) reduces to

$$H_{\text{charge}} = t_c S^z + \omega_c a^\dagger a + g_{\text{ch}} S^x \otimes (a + a^\dagger). \quad \text{(I7)}$$

Accordingly, the (pseudo)spin-resonator coupling is maximized at this charge-degeneracy point, i.e., when there is no bias between the two dots, and decreases as one moves away from this point [29,32,35].

Coupling strength. Following Ref. [47], the single-phonon coupling strength g_{ch} may be expressed as

$$\frac{g_{\text{ch}}}{\omega_c} = \zeta_{\text{ch}} = \sqrt{\alpha_{\text{eff}}}\sqrt{\frac{l^2\lambda}{V}}, \quad \text{(I8)}$$

where V is the mode volume associated with the resonator mode and $\alpha_{\text{eff}} = \alpha K^2 c/v_s\epsilon_r$ is an effective fine-structure constant, defined in terms of the fine-structure constant $\alpha \sim \frac{1}{137}$, the (material-specific) electromechanical coupling coefficient K^2 (as a widely used measure to quantify the piezoelectric coupling strength), the speed of light c, the SAW speed of sound v_s, and the relative dielectric constant ϵ_r. The coupling parameter K^2 describes piezoelectric stiffening and may be expressed as $K^2 = e_{14}^2/\underline{c}\epsilon$, where e_{14}, $\underline{c}$, and ϵ refer to representative values of the piezoelectric, the elasticity, and the dielectric tensor, respectively. Typical values for $\alpha_{\text{eff}}/\alpha$ range from $\alpha_{\text{eff}}/\alpha \sim 10$ for GaAs up to $\alpha_{\text{eff}}/\alpha \gtrsim 100$ for strongly piezoelectric materials such as $LiNbO_3$ or ZnO, underlining the potential of SAW-based systems to reach the ultrastrong coupling regime [47]. For a typical SAW penetration length $\sim 0.3\lambda$ close to the surface, Eq. (I8) further simplifies to $g_{\text{ch}}/\omega_c \approx (0.5\text{–}1.5)\sqrt{l^2/A}$, where A refers to the surface mode area. When expressing α_{eff} in terms of the fundamental material parameters, Eq. (I8) can be rewritten as

$$\frac{g_{\text{ch}}}{\omega_c} \approx \frac{ee_{14}}{\epsilon v_s}\sqrt{\frac{1}{\rho v_s}}\sqrt{\frac{l^2\lambda}{V}}. \quad \text{(I9)}$$

This estimate also follows from the expression given above, $g_{\text{ch}} = e\phi_0\mathcal{F}(kd)\sin(kl/2)$, with $\phi_0 \approx (e_{14}/\epsilon)\sqrt{\hbar/2\rho V\omega_c}$ [46], close to the surface $\mathcal{F}(kd) \sim 1$, and with $\sin(kl/2) \approx kl/2$ for $kl/2 \ll 1$ (in the spirit of circuit-QED setups).

Spin qubit. In the two-electron regime of a DQD, one can couple the effective dipole moment of singlet-triplet subspace to the resonator mode [27,46]. Within the two-level subspace (all other levels are far detuned), the dynamics is described by

$$H_{\text{spin}} = \frac{\Omega}{2}\sigma^z + \omega_c a^\dagger a + g^x\sigma^x \otimes (a + a^\dagger) + g^z\sigma^z \otimes (a + a^\dagger), \quad \text{(I10)}$$

where $\sigma^z = |1\rangle\langle 1| - |0\rangle\langle 0|$, $\sigma^x = |1\rangle\langle 0| + |0\rangle\langle 1|$ and

$$g^x = e\phi_0\mathcal{F}(kd)\eta_{\text{geo}}\kappa_0\kappa_1, \quad \text{(I11)}$$

$$g^z = e\phi_0\mathcal{F}(kd)\eta_{\text{geo}}\left[\kappa_1^2 - \kappa_0^2\right]/2. \quad \text{(I12)}$$

Here, $\eta_{\text{geo}} = \sin(kx_R) - \sin(kx_L)$ accounts for the positioning of the DQD with respect to the piezoelectric mode function. The coupling is reduced by the admixtures of the qubit's states $\{|0\rangle, |1\rangle\}$ with the localized singlet $\kappa_n = \langle n|S_{02}\rangle$. Again, for $\Omega \approx \omega_c$ and $g^\alpha \ll \omega_c$, we recover the prototypical Jaynes-Cummings dynamics. Moreover, the spin-resonator Hamiltonian given in Eq. (I10) belongs to the general class of Hamiltonians defined in Eq. (1).

Hot gate. For such a spin qubit, a spin-resonator coupling strength of $g_{\text{sp}}/2\pi \equiv g^x/2\pi = (g_0/2\pi)\kappa_0\kappa_1 \approx 3.2$ MHz($g^z/2\pi \approx 0.64$ MHz) has been predicted for typical parameters in GaAs [46]. For a typical resonator frequency $\omega_c/2\pi \approx 1.5$ GHz, this amounts to a relative coupling strength $\mu_{\text{sp}} = g_{\text{sp}}/\omega_c \approx 0.2\%$ and an effective coupling $g_{\text{eff}}/2\pi = \mu_{\text{sp}}g_{\text{sp}}/2\pi \approx 65$ kHz, which could be increased substantially by additionally depositing a strongly piezoelectric material such as $LiNbO_3$ or ZnO on the GaAs substrate [46,47,63]. The condition $\omega_c \gg \Omega$ can be satisfied by choosing the magnetic gradient Δ between the dots appropriately, $\Delta \lesssim 0.1\ \mu$eV. Recently, SAW resonators with quality factors approaching $\sim 10^6$ have been realized experimentally [64]. Then, taking

an optimistic quality factor of $Q = 10^6$, according to the hot-gate requirement $k_B T \ll Q \times g_{\rm eff}$, we find $T \ll 3.1$ K; therefore, for spin qubits coupled to high-quality SAW resonators, our scheme can tolerate temperatures approaching the Kelvin regime, where the thermal occupation number is much larger than one. For example, for $\omega_c/2\pi \approx (1.0\text{–}1.5)$ GHz and $T \approx 0.5$ K, we have $\bar{n}_{\rm th} \approx 6.5\text{–}10$. The second requirement for small errors, $\Gamma \ll g_{\rm eff}$, yields $\Gamma/2\pi \ll 65$ kHz, which may be satisfied in GaAs with recently demonstrated echo techniques, where decoherence time scales $T_2 \approx 1$ ms have been demonstrated [65]. Finally, with $\bar{n}_{\rm th}/Q \approx 10/10^6$ and $\Gamma/\omega_c \approx 1$ kHz/1.5 GHz, and using the relation $\xi \approx \alpha_\kappa(\kappa/\omega_c)\bar{n}_{\rm th} + \alpha_\Gamma \Gamma/\omega_c$, we can estimate the overall gate error as $\xi \approx 4 \times 10^{-5} + 2.5 \times 10^{-2} \approx 2.5\%$, which is largely limited by dephasing-induced errors (for the parameters chosen here). Again, to counteract this source of error, a strongly piezoelectric material such as $LiNbO_3$ may be used on the GaAs substrate. Alternatively, one could also investigate silicon quantum dots: while this setup also requires a more sophisticated heterostructure including some piezoelectric layer, it should benefit from prolonged dephasing times $T_2^\star > 100\ \mu$s [58], which is not longer than the dephasing time T_2 quoted above for GaAs, but relaxes the need for dynamical decoupling.

APPENDIX J: MICROSCOPIC DERIVATION OF THE NOISE MODEL

In this appendix, we provide a microscopic derivation of the master equation given in Eq. (7) of our paper. Here, we focus on the relevant decoherence processes induced by coupling between the resonator mode and its environment and restrict ourselves to the regime of interest where $\omega_q \to 0$. Our analysis is built upon the master-equation formalism, a tool widely used in quantum optics for studying the irreversible dynamics of a quantum system coupled to a macroscopic environment. We detail the assumptions of our approach and discuss in detail the relevant approximations.

1. Model

We consider a generic linear coupling between the resonator mode and a set of independent harmonic oscillators (representing, e.g., the modes of the free electromagnetic field), as described by the following textbook system-bath Hamiltonian:

$$H = \underbrace{H_S + H_B}_{=H_0} + H_I, \tag{J1}$$

$$H_S = \omega_c a^\dagger a + g\mathcal{S} \otimes (a + a^\dagger), \tag{J2}$$

$$H_B = \int_{\omega_c - \Delta_B}^{\omega_c + \Delta_B} d\omega\, \omega b_\omega^\dagger b_\omega, \tag{J3}$$

$$H_I = \int_{\omega_c - \Delta_B}^{\omega_c + \Delta_B} d\omega \sqrt{\frac{\kappa(\omega)}{2\pi}} (a^\dagger b_\omega + a b_\omega^\dagger), \tag{J4}$$

where b_ω refer to bosonic bath operators obeying standard commutation relations with $[b_\omega, b_{\omega'}^\dagger] = \delta(\omega - \omega')$, etc., and Δ_B denotes the characteristic bandwidth of the bath [66–68]. Within a rotating-wave approximation, we have dropped all energy-nonconserving terms, which is valid if the system's characteristic frequency ω_c is the largest frequency in the problem [67]. The bandwidth Δ_B is the frequency range over which the system-bath coupling is valid; it is closely related to the characteristic memory or correlation time of the bath $\tau_c \sim \Delta_B^{-1}$, as can be readily seen from the relation

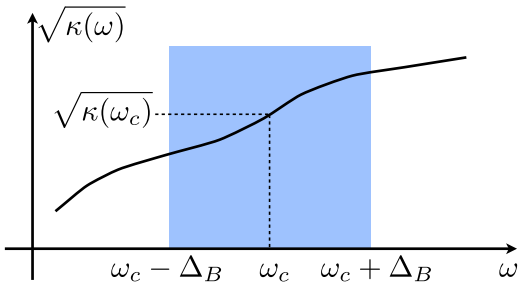

FIG. 11. Schematic illustration of the hierarchy of frequency scales assumed for the derivation of the quantum master equation. Following the standard treatment [70], the reservoir spectral density $\kappa(\omega)/2\pi$ is taken to be a flat function of ω within the frequency range of interest $[\omega_c - \Delta_B, \omega_c + \Delta_B]$.

$$\int_{\omega_c - \Delta_B}^{\omega_c + \Delta_B} d\omega\, e^{-i\omega\tau} = 2\Delta_B e^{-i\omega_c \tau} \mathrm{sinc}(\Delta_B \tau) \tag{J5}$$

$$= 2\pi \delta_{\Delta_B}(\tau) e^{-i\omega_c \tau}, \tag{J6}$$

as it appears in the standard derivation of the master equation presented below [if the spectral noise density $\kappa(\omega)$ and the thermal occupation number $\bar{n}_{\rm th}(\omega)$ are evaluated self-consistently at $\omega = \omega_c$]. Here, the function $\delta_{\Delta_B}(\tau) = \pi^{-1}\Delta_B \mathrm{sinc}(\Delta_B \tau)$ is a well-known diffractionlike function with a maximal amplitude Δ_B/π at $\tau = 0$ and a width of the order of $\tau_c \sim 2\pi/\Delta_B$ [54]. Since the integral equals one, this function is an approximate delta function which tends to $\delta(\tau)$ in the so-called white-noise limit $\Delta_B \to \infty$ (that is, $\tau_c \to 0$). Intuitively, $\delta_{\Delta_B}(\tau)$ can be seen as a slowly varying function (on the $\sim\omega_c^{-1}$ time scale) that effectively acts as a delta function on time scales of the system evolution (i.e., much slower than $1/\Delta_B$). Typically, $\Delta_B \ll \omega_c$ is assumed [66,67], but τ_c is still much shorter than the relevant time scales of the system dynamics $\tau_{\rm sys}$ (other than the free rotation ω_c), that is,

$$\omega_c \gg \Delta_B \gg \tau_{\rm sys}^{-1}. \tag{J7}$$

In this case, the bandwidth Δ_B can be much larger than the spin-resonator coupling strength g (which implies $g\tau_c \ll 1$, as required for the standard master-equation treatment discussed below), but still much smaller than the characteristic frequency ω_c. The system-reservoir coupling is usually only valid within a bandwidth $2\Delta_B \ll \omega_c$ around ω_c [67]. Within this frequency range the coupling strength may be approximated by a constant value as $\kappa(\omega) \approx \kappa(\omega_c)$, as schematically depicted in Fig. 11.

2. Microscopic derivation of the master equation

Our analysis is based on the standard Born-Markov framework, where correlations between the system and the bath are neglected (on relevant time scales) since the bath is considered to be very large and the effect of the interaction with the (small) system is negligible. Within this standard

Born-Markov approximation [54,69], in the interaction picture the system's dynamics is described by

$$\dot{\tilde{\rho}} = -\int_0^\infty d\tau\, \mathrm{Tr}_B\{[\tilde{H}_I(t),[\tilde{H}_I(t-\tau),\tilde{\rho}(t)\rho_B]]\}, \tag{J8}$$

with $\tilde{\rho} = e^{iH_0 t}\rho(t)e^{-iH_0 t}$, $\tilde{H}_I(t) = e^{iH_0 t}H_I e^{-iH_0 t}$, and $\rho_B = Z^{-1}\exp[-\beta H_B]$ refers to a thermal state of the bath with the standard thermal correlation functions [69]

$$\mathrm{Tr}_B[b_\omega^\dagger b_{\omega'}\rho_B] = \bar{n}_{\mathrm{th}}(\omega)\delta(\omega-\omega'), \tag{J9}$$

etc. Equation (J8) can equivalently be expressed as

$$\dot{\tilde{\rho}} = \int_0^\infty d\tau\, \mathrm{Tr}_B\{\underbrace{\tilde{H}_I(t)\tilde{\rho}(t)\rho_B\tilde{H}_I(t-\tau)}_{①} - \tilde{H}_I(t)\tilde{H}_I(t-\tau)\tilde{\rho}(t)\rho_B + \mathrm{H.c.}\}. \tag{J10}$$

In the interaction picture, the system-bath coupling reads as explicitly

$$\tilde{H}_I(t) = \int_{\omega_c-\Delta_B}^{\omega_c+\Delta_B} d\omega\sqrt{\frac{\kappa(\omega)}{2\pi}}\{e^{-i\omega t}b_\omega[e^{i\omega_c t}(a^\dagger+\mu\mathcal{S})-\mu\mathcal{S}] + e^{i\omega t}b_\omega^\dagger[e^{-i\omega_c t}(a+\mu\mathcal{S})-\mu\mathcal{S}]\}, \tag{J11}$$

where we have used the fact that the resonator annihilation operators transform as

$$\tilde{a}(t) = e^{iH_S t}ae^{-iH_S t} = e^{-i\omega_c t}(a+\mu\mathcal{S})-\mu\mathcal{S}, \tag{J12}$$

while the bath operators transform simply as $\tilde{b}_\omega(t) = e^{iH_B t}b_\omega e^{-iH_B t} = e^{-i\omega t}b_\omega$. Next, let us single out one term explicitly, but all other terms follow analogously. Using the thermal correlation functions as stated in Eq. (J9), we then obtain

$$\begin{aligned}\mathrm{Tr}_B\{①\} = &\int_{\omega_c-\Delta_B}^{\omega_c+\Delta_B} d\omega\frac{\kappa(\omega)}{2\pi}\bar{n}_{\mathrm{th}}(\omega)e^{-i\omega\tau}\\ &\times[e^{i\omega_c t}(a^\dagger+\mu\mathcal{S})-\mu\mathcal{S}]\tilde{\rho}(t)\\ &\times[e^{-i\omega_c(t-\tau)}(a+\mu\mathcal{S})-\mu\mathcal{S}]\\ &+\int_{\omega_c-\Delta_B}^{\omega_c+\Delta_B} d\omega\frac{\kappa(\omega)}{2\pi}[\bar{n}_{\mathrm{th}}(\omega)+1]e^{i\omega\tau}\\ &\times[e^{-i\omega_c t}(a+\mu\mathcal{S})-\mu\mathcal{S}]\tilde{\rho}(t)\\ &\times[e^{i\omega_c(t-\tau)}(a^\dagger+\mu\mathcal{S})-\mu\mathcal{S}],\end{aligned} \tag{J13}$$

and similar expressions for the remaining terms in Eq. (J8). In the next step, we perform the integration over the past, using the relation [71]

$$\int_0^\infty d\tau\, e^{\pm i(\omega_c-\omega)\tau} = \pi\delta(\omega_c-\omega)\pm i\mathbb{P}\frac{1}{\omega_c-\omega}, \tag{J14}$$

with $\mathbb{P}$ denoting Cauchy's principal value, perform the integration over frequency, and within a rotating-wave approximation [which is valid for the realistic parameter regime $\mu\kappa(\omega_c)\bar{n}_{\mathrm{th}}(\omega_c)\sqrt{\bar{n}_{\mathrm{th}}(\omega_c)} \ll \omega_c$] drop all fast oscillating terms $\sim\exp[\pm i\omega_c t]$. After some simple manipulations, we then arrive at the master equation

$$\begin{aligned}\dot{\tilde{\rho}} = &\kappa(\omega_c)[\bar{n}_{\mathrm{th}}(\omega_c)+1]\mathcal{D}[a+\mu\mathcal{S}]\tilde{\rho}\\ &+\kappa(\omega_c)\bar{n}_{\mathrm{th}}(\omega_c)\mathcal{D}[a^\dagger+\mu\mathcal{S}]\tilde{\rho}\\ &-i\Delta_c[(a^\dagger+\mu\mathcal{S})(a+\mu\mathcal{S}),\tilde{\rho}]\\ &+\gamma\mathcal{D}[\mathcal{S}]\tilde{\rho}-i\Delta_S[\mathcal{S}^2,\tilde{\rho}].\end{aligned} \tag{J15}$$

Here, we have introduced the decay rate

$$\gamma = \mu^2\int_{\omega_c-\Delta_B}^{\omega_c+\Delta_B} d\omega\,\kappa(\omega)[2\bar{n}_{\mathrm{th}}(\omega)+1]\delta(\omega-0), \tag{J16}$$

which derives from the terms in Eq. (J13) rotating at zero frequency, and the Lamb-type energy shifts

$$\Delta_c = \mathbb{P}\int_{\omega_c-\Delta_B}^{\omega_c+\Delta_B} d\omega\frac{\kappa(\omega)}{2\pi}\frac{1}{\omega_c-\omega}, \tag{J17}$$

$$\Delta_S = \mu^2\mathbb{P}\int_{\omega_c-\Delta_B}^{\omega_c+\Delta_B} d\omega\frac{\kappa(\omega)}{2\pi}\frac{1}{\omega}. \tag{J18}$$

In accordance with the frequency regime ($\omega_c \gg \Delta_B \gg \tau_{\mathrm{sys}}^{-1}$) discussed above, we assume the bandwidth Δ_B to be large, but finite. In this case, the rate γ vanishes ($\gamma = 0$), as the integration range does not cover the δ peak at $\omega = 0$. Physically, the regime where the lower limit of the relevant frequency range $\omega_c - \Delta_B$ does not extend all the way down to zero frequency amounts to the existence of a lower-frequency cutoff $\omega_{\mathrm{cut}} = \omega_c - \Delta_B$. For example, such a lower-frequency cutoff ω_{cut} naturally arises in the context of a phonon bath where the existence of $\omega_{\mathrm{cut}} \sim \lambda_{\mathrm{cut}}^{-1}$ is due to finite device dimensions (since a phonon wavelength λ larger than the device dimensions is not supported by this structure). Moreover, phonons with a wavelength much larger than the resonator are not able to resolve the resonator and simply represent a global shift of the resonator structure as a whole (and therefore do not linearly couple to the localized resonator mode). On the contrary, in the limit of infinite bandwidth $\Delta_B \to \infty$, the decay rate γ (as well as the Lamb-type shifts Δ_c, Δ_S) will depend on the relevant reservoir spectral density

$$\kappa(\omega)/2\pi = g^2(\omega)D_{\mathrm{DOS}}(\omega), \tag{J19}$$

often abbreviated as $J(\omega) = \kappa(\omega)/2\pi$ in the literature [72]. The spectral density $J(\omega) = \sum_k |g_k|^2\delta(\omega-\omega_k)$ encodes the features of the environment relevant for the reduced system description, and depends on both the environmental density of the modes $D_{\mathrm{DOS}}(\omega)$ and on how strongly the system couples to each mode $\sim g(\omega)$. For concreteness, let us discuss two particular examples: (i) First, in quantum optical systems typically $J(\omega) \sim \omega^n$ for a positive integer n [70,71]; in particular, for coupling of a harmonic oscillator to the electromagnetic field in three dimensions in free space the spectral density scales as $J(\omega) \sim \omega^3$ [73]. In this case, even in the absence of a lower-frequency cutoff ω_{cut}, the rate γ vanishes because $\kappa(\omega)\bar{n}_{\mathrm{th}}(\omega) \sim \omega^2 \to 0$ in the limit $\omega \to 0$. (ii) Second, a prominent phenomenological ansatz frequently used in the literature is the so-called Caldeira-Leggett model, where $J(\omega) \sim \omega^\alpha\Omega_{\mathrm{cut}}^{1-\alpha}e^{-\omega/\Omega_{\mathrm{cut}}}$ for all $\alpha > 0$ and some high-frequency cutoff Ω_{cut} [72]. Environments with $0 < \alpha < 1$ are referred to as sub-Ohmic, while those corresponding to $\alpha = 1$

and $\alpha > 1$ are called Ohmic and super-Ohmic, respectively [72]. Within this Caldeira-Leggett model (and for $\Delta_B \to \infty$), the decay rate γ given in Eq. (J16) vanishes for super-Ohmic spectral densities with $\alpha > 1$ becomes a constant for $\alpha = 1$ and diverges for $\alpha < 1$ since $\bar{n}_{\rm th}(\omega) \sim k_B T/\omega$ for $k_B T \gg \omega$.

Here, we restrict our analysis to the regime where γ vanishes, either because of the existence of a lower-frequency cutoff $\omega_{\rm cut} > 0$ or a spectral density with $J(\omega) \sim \omega^\alpha (\alpha > 1)$, as discussed above. Moreover, following the standard treatment [54,74] we neglect the Lamb shift $\Delta_S \sim \mu^2$ (typically, it is assumed that the Cauchy principal part of an integral of the spectral density is very small compared to the real part expressions [69,75]), yielding the master equation

$$\begin{aligned}\dot{\tilde{\rho}} = {} & \kappa(\omega_c)[\bar{n}_{\rm th}(\omega_c)+1]\mathcal{D}[a+\mu\mathcal{S}]\tilde{\rho} \\ & + \kappa(\omega_c)\bar{n}_{\rm th}(\omega_c)\mathcal{D}[a^\dagger+\mu\mathcal{S}]\tilde{\rho} \\ & - i\Delta_c[(a^\dagger+\mu\mathcal{S})(a+\mu\mathcal{S}),\tilde{\rho}], \end{aligned} \tag{J20}$$

which (due to the interaction-mediated hybridization of spin and resonator degrees of freedom $\sim g$) displays correlated decay terms of both resonator and spin degrees of freedom, that are proportional to the effective rate $\sim\kappa(\omega)\bar{n}_{\rm th}(\omega)$ evaluated at the (large) characteristic system frequency ω_c. Using the relation

$$e^{-iH_S t}(a+\mu\mathcal{S})e^{iH_S t} = e^{i\omega_c t}(a+\mu\mathcal{S}), \tag{J21}$$

the corresponding master equation in the Schrödinger picture is found to be

$$\begin{aligned}\dot{\rho} = {} & \kappa(\omega_c)[\bar{n}_{\rm th}(\omega_c)+1]\mathcal{D}[a+\mu\mathcal{S}]\rho \\ & + \kappa(\omega_c)\bar{n}_{\rm th}(\omega_c)\mathcal{D}[a^\dagger+\mu\mathcal{S}]\rho \\ & - i[H_S,\rho] - i\Delta_c[(a^\dagger+\mu\mathcal{S})(a+\mu\mathcal{S}),\rho]. \end{aligned} \tag{J22}$$

In what follows, we restrict our analysis to the experimentally most relevant regime of weak spin-resonator coupling where $\mu = g/\omega_c \ll 1$. Within the corresponding approximation of independent rates of variation [54], the interactions with the environment are treated separately for spin and resonator degrees of freedom; in other words, they can approximately be treated as independent entities and the terms (rates of variation) due to internal and dissipative dynamics are added independently. While for ultrastrong coupling the qubit-resonator system needs to be treated as a whole when studying its interaction with the environment [74], yielding irreversible dynamics through jumps between dressed states (rather than bare states), in the weak coupling regime we recover standard (quantum optical) dissipators, i.e.,

$$\dot{\rho} = -i[H_S,\rho] + \kappa[\bar{n}_{\rm th}+1]\mathcal{D}[a]\rho + \kappa\bar{n}_{\rm th}\mathcal{D}[a^\dagger]\rho. \tag{J23}$$

In the last step, we have set $\kappa \equiv \kappa(\omega_c)$, $\bar{n}_{\rm th} \equiv \bar{n}_{\rm th}(\omega_c)$ and dropped the energy shift Δ_c which may be incorporated into a renormalized cavity frequency $\omega_c \to \omega_c + \Delta_c$.

Note that the approximate replacement of the correlated dissipators by uncorrelated ones, that is, $\mathcal{D}[a+\mu\mathcal{S}]\rho \to \mathcal{D}[a]\rho$ and $\mathcal{D}[a^\dagger+\mu\mathcal{S}]\rho \to \mathcal{D}[a^\dagger]\rho$, gives rise to a conservative error estimate for our hot gate. As can be shown analytically (compare Appendix L), the rethermalization-induced error ξ_κ induced by independent decay terms as given in Eq. (J23) is twice as large as the one due to correlated decay terms. This statement has also been verified numerically; compare Table I.

TABLE I. Comparison of the rethermalization-induced error $\xi_\kappa(\%)$ for two different master equations, namely, Eq. (J23) (uncorrelated noise model) and $\dot{\rho} = -i[H_S,\rho] + \kappa[\bar{n}_{\rm th}+1]\mathcal{D}[a+\mu\mathcal{S}]\rho + \kappa\bar{n}_{\rm th}\mathcal{D}[a^\dagger+\mu\mathcal{S}]\rho$ (correlated noise model). The error found for the uncorrelated noise model (as used in the main text) is about twice as large as the one found for the correlated one, and may therefore be seen as a conservative estimate. Note that Fig. 4(c) of the main text is partially based on the first row (uncorrelated noise model). Other numerical parameters: $\mu = g/\omega_c = \frac{1}{16}$, $\Gamma = 0$, $k_B T/\omega_c = 2$, and $\omega_q = 0$.

$\kappa/\omega_c\bar{n}_{\rm th}(10^{-3})$	0	0.5	1	1.5	2	2.5
$\xi_\kappa(\%)$ for uncorrelated noise	0.0	0.21	0.41	0.61	0.81	1.01
$\xi_\kappa(\%)$ for correlated noise	0.0	0.10	0.20	0.30	0.40	0.50

While Eq. (J23) is not rigorous (given the approximations made throughout its derivation), this type of noise model (with independent rather than correlated decay terms, and complemented by additional dissipators for the qubits) has been used widely to describe a great variety of relevant spin-resonator systems (in the regime of weak spin-resonator coupling for values up to $\mu = g/\omega_c \lesssim 4\%$ [76]), ranging, e.g., from superconducting qubits [25,76] as well as quantum dots coupled to transmission line resonators [31,37], to NV-center spins [49] or carbon nanotubes [77] coupled to nanomechanical oscillators. For example, in Refs. [31,37] very good agreement with experimental results has been achieved for $\mu \sim 1\%$.

We conclude this discussion with a final remark on low-frequency noise: As shown above, the existence of a low-frequency cutoff does exclude low-frequency contributions to resonator-mediated dephasing of the spins (since $\gamma = 0$). Still, low-frequency noise (deriving for example from ambient nuclear spins [1]) may still couple directly to the qubits. In our model, this type of noise is captured by the dephasing rate Γ, which may, however, be mitigated efficiently by simple spin-echo techniques.

APPENDIX K: ADDITIONAL NUMERICAL RESULTS

Here, we provide further detailed results based on the numerical simulation of the master equation given in Eq. (7). Just as in the main text, for all simulations shown below the initial state of the spin-resonator system has been chosen as $\rho(0) = |\Uparrow\Downarrow\rangle\langle\Uparrow\Downarrow| \otimes \rho_{\rm th}(T)$, with the cavity mode in the thermal state $\rho_{\rm th}(T) = Z^{-1}\exp[-\beta\omega_c a^\dagger a]$. Apart from the state fidelity $\mathcal{F}$, we also quantify the logarithmic negativity $E_\mathcal{N}$ (which ranges between 0 for separable states to at maximum 1 for two maximally entangled qubits) in order to quantify the entanglement between the two qubits.

Periodic recurrences. First, as displayed in Fig. 12, we observe periodic recurrences of the maximally entangling dynamics: For example, for $g/\omega_c = \frac{1}{4}$ (as used in Fig. 12), ideally, apart from $\mathcal{F} = 1$ at $(\omega_c/2\pi)t = 1$, we find $\mathcal{F} = 1$ again at $(\omega_c/2\pi)t = 5$ since $U_{\rm id}^x(m = 5, \frac{1}{4}) = \exp[i\pi\sigma_1^x\sigma_2^x]U_{\rm id}^x(1, \frac{1}{4}) = -U_{\rm id}^x(1, \frac{1}{4})$. This statement holds provided that dephasing is negligible on the relevant time scale; compare the dashed curve in Fig. 12 which accounts for dephasing of the qubits.

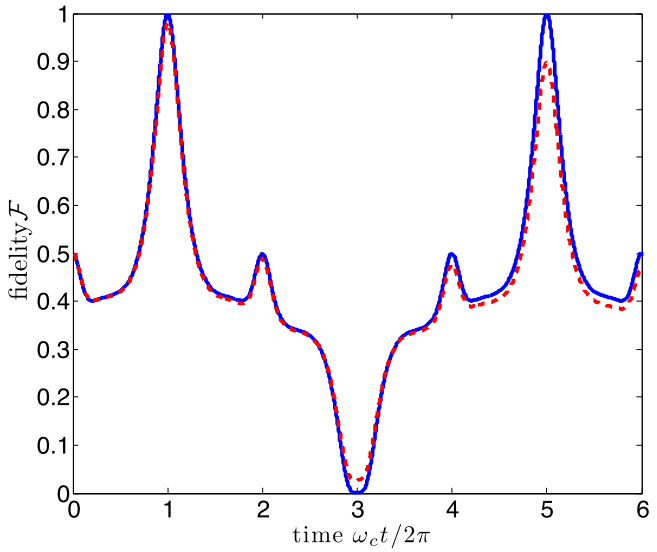

FIG. 12. Fidelity $\mathcal{F}$ for the two-qubit state ρ_{qubits} with the target state $|\Psi_{\text{tar}}\rangle = (|\Uparrow\Downarrow\rangle + i|\Downarrow\Uparrow\rangle)/\sqrt{2}$ for $\Gamma/\omega_c = 0$ (blue solid line) and $\Gamma/\omega_c = 1\%$ (red dashed line). For sufficiently low noise, at $\omega_c t = 2\pi$ and $\omega_c t = 5 \times 2\pi$ the fidelity with the maximally entangled state $|\Psi_{\text{tar}}\rangle$ reaches the maximal value $\mathcal{F} = 1$. Numerical parameters: $\omega_q/\omega_c = 0$, $k_B T/\omega_c = 2\,(\bar{n}_{\text{th}} \approx 1.54)$, $g/\omega_c = \frac{1}{4}$, $\kappa/\omega_c = Q^{-1} = 10^{-5}$.

Nonzero level splitting. While our analytical treatment has assumed $\omega_q = 0$, in Fig. 13 we provide exemplary numerical results that explicitly account for a nonzero qubit-level splitting $\omega_q > 0$, showing that the proposed protocol can tolerate nonzero level splittings of the qubits $\omega_q/\omega_c \lesssim 0.1$, without a severe reduction in the fidelity of the protocol. Again, this numerical finding is corroborated in Fig. 14. Here, it is shown explicitly that a strong entanglement reduction is observed

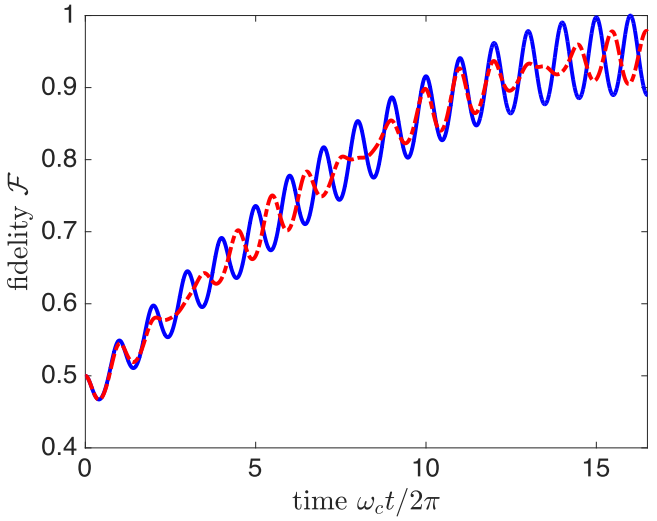

FIG. 13. Fidelity $\mathcal{F} = \langle\Psi_{\text{tar}}|\rho_{\text{qubits}}|\Psi_{\text{tar}}\rangle$ for the two-qubit state $\rho_{\text{qubits}} = \text{Tr}_{\text{cav}}[\rho]$ with the target state $|\Psi_{\text{tar}}\rangle = (|\Uparrow\Downarrow\rangle + i|\Downarrow\Uparrow\rangle)/\sqrt{2}$ for both $\omega_q/\omega_c = 0$ (solid blue line) and $\omega_q/\omega_c = 0.1$ (dashed red line); here, $g/\omega_c = \frac{1}{16} < 0.1$. Other numerical parameters: $k_B T/\omega_c = 2\,(\bar{n}_{\text{th}} \approx 1.54)$, $Q = 10^5$, and $\Gamma/\omega_c = 0$.

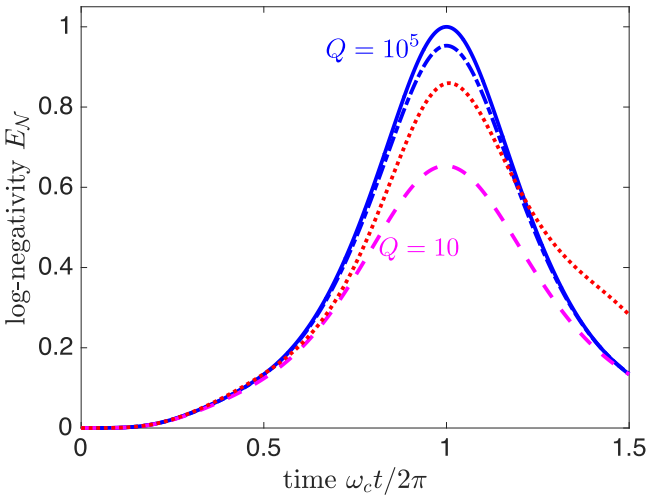

FIG. 14. Logarithmic negativity $E_{\mathcal{N}}$ for $k_B T/\omega_c = 1$ and different cavity quality factors: $Q = 10^5$ (solid blue), $Q = 10^2$ (dashed-dotted blue), and $Q = 10$ (dashed magenta). A clear reduction of the maximum entanglement is observed, if the quality factor Q is too low to satisfy the hot-gate requirement given in Eq. (8). Here, we have $g/\omega_c \times g/k_B T = \frac{1}{16} = 6.25 \times 10^{-2}$. The red (dotted) curve refers to $Q = 10^2$ and $\omega_q/\omega_c = 0.2$. Other numerical parameters: $g/\omega_c = \frac{1}{4}$ and $\Gamma/\omega_c = 0$.

once condition (8) is violated. Conversely, within the range of parameter values satisfying Eq. (8), the results are rather insensitive to the particular parameter values.

Rethermalization-induced errors. As illustrated in Fig. 15, we have numerically checked that (for small infidelities)

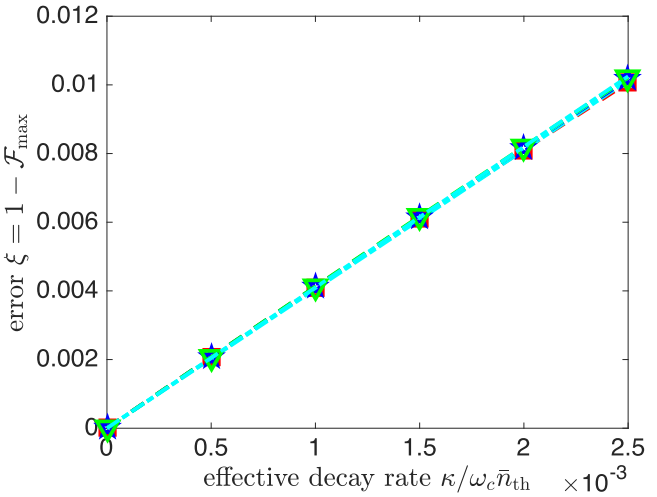

FIG. 15. Error as a function of the effective rethermalization rate $\kappa\bar{n}_{\text{th}}$ for $g/\omega_c = \frac{1}{16}$ (red squares), $g/\omega_c = 1/(8\sqrt{2})$ (blue stars) and $g/\omega_c = \frac{1}{8}$ (green triangles), and $k_B T/\omega_c = 2(\bar{n}_{\text{th}} \approx 1.54)$, within the relevant small-error regime ($\kappa_{\text{eff}}/g_{\text{eff}} \ll 1$). The dashed-dotted lines in cyan refer to linear fits, demonstrating a linear error scaling in the small error regime ($\kappa_{\text{eff}}/g_{\text{eff}} \ll 1$), which is independent of $\mu = g/\omega_c$. Accordingly, the error is larger for higher temperatures, but all temperature-related effects are approximately captured by the thermal occupation number $\bar{n}_{\text{th}}$. Other numerical parameters: $\Gamma = 0$ and $\omega_q = 0$.

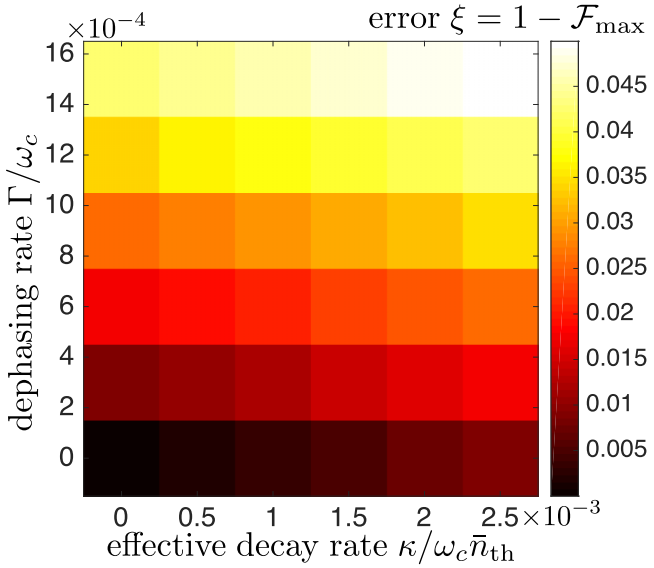

FIG. 16. Total error ξ as a function of both the effective rethermalization rate $\sim\kappa/\omega_c\bar{n}_{\rm th} \sim \bar{n}_{\rm th}/Q$ and the spin dephasing rate $\sim\Gamma/\omega_c$ for $g/\omega_c = \frac{1}{16}$, $k_BT/\omega_c = 4$, and $\omega_q = 0$.

the rethermalization-induced error ξ_κ scales linearly with the effective rethermalization rate $\kappa_{\rm eff} = \kappa\bar{n}_{\rm th}$. Notably, as evidenced in Fig. 15, the error is found to be independent of the spin-resonator coupling g. As demonstrated in in Appendix L, this numerical result can be corroborated analytically within a perturbative framework.

Full error analysis. Similar to Fig. 4(c) in the main text, in Fig. 16 we provide numerical results that fully account for higher-order, correlated errors (beyond the linear error approximation). Here, we have chosen a temperature $k_BT/\omega_c = 4$, a factor 2 larger than the one used in Fig. 4(c) in the main text. Still, if the rethermalization-induced error is scaled in terms of the effective decay rate $\kappa_{\rm eff} = \kappa\bar{n}_{\rm th}$, we obtain (approximately) the same total error ξ, independently of the temperature k_BT, showing that the effective decay rate $\kappa_{\rm eff} = \kappa\bar{n}_{\rm th}$ captures well any temperature-related effects. This is evidenced numerically in Fig. 16 which approximately coincides with the results displayed in Fig. 4(c) in the main text and is in line with our simple error estimate for rethermalization-induced errors; compare Eq. (10) in the main text.

Timing errors. Finally, we consider errors (infidelities) due to limited timing accuracies. To do so, we take the average fidelity of our protocol $\bar{\mathcal{F}}$ within a certain timing window Δt centered around the stroboscopic time $t_{\max}$ for which maximum fidelity (minimal infidelity) is achieved; for example, in quantum dot systems timing accuracies Δt of a few picoseconds have been demonstrated experimentally [78]. For $g/2\pi = 10$ MHz and $\omega_c/2\pi = 160$ MHz (that is, $\mu = g/\omega_c = \frac{1}{16}$) as used in the main text, the pulse time lies in the microsecond regime ($t_{\max} = \pi/8g_{\rm eff} \approx 0.2\ \mu$s), for which $\Delta t \approx 1$ ps is feasible; for this relatively long pulse, the relative time jitter is well below the percent level, i.e., $(\omega_c/2\pi)\Delta t \approx 10^{-4}$. Based on our numerical simulations, we make the following observations: (i) As demonstrated in Fig. 17, we find an average error scaling linearly with $\sim\bar{n}_{\rm th}$, that is $\bar{\xi} = 1 - \bar{\mathcal{F}} \sim \bar{n}_{\rm th}$. (ii) More precisely, the error expressions given in the main text can be generalized to

$$\bar{\xi} = \bar{\alpha}_\kappa \frac{\kappa}{\omega_c}\bar{n}_{\rm th} + \bar{\alpha}_\Gamma \frac{\Gamma}{\omega_c} + \bar{\beta}_\kappa + \bar{\beta}_\Gamma. \tag{K1}$$

Here, the unit-less quantities $\bar{\alpha}_\gamma, \bar{\beta}_\gamma$ for $\gamma = \kappa, \Gamma$ depend on the timing window Δt. For example, for $g/\omega_c = \frac{1}{16}$ and $(\omega_c/2\pi)\Delta t = 5\%$, we then extract $\bar{\alpha}_\kappa \approx 4.03$, $\bar{\beta}_\kappa \approx 2.2 \times 10^{-4}$, $\bar{\alpha}_\Gamma \approx 24.22$, and $\bar{\beta}_\Gamma \approx 5.1 \times 10^{-4}$. (iii) As shown in Fig. 17, for the experimentally most relevant regime where $(\omega_c/2\pi)\Delta t \ll 1$ (such that the timing window covers a small range of the oscillations only), this error is found to decrease for a smaller spin-resonator coupling strength g/ω_c because larger values of g/ω_c imply larger oscillation amplitudes within the relevant range over which we have to average; compare the center and right plots in Fig. 17. Therefore, for the experimentally most relevant regime where $(\omega_c/2\pi)\Delta t \ll 1$ and $g/\omega_c \lesssim \frac{1}{16}$, the effects of time jitter should be negligible.

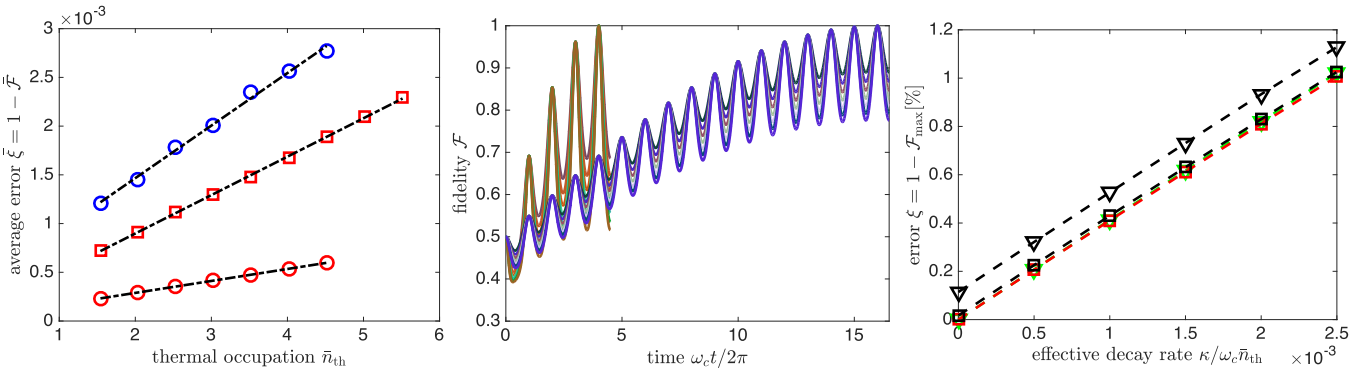

FIG. 17. Timing errors. Left: total average error $\bar{\xi}$ as a function of the thermal occupation number $\bar{n}_{\rm th}$ for timing windows $(\omega_c/2\pi)\Delta t = 5\%$ (circles) and $(\omega_c/2\pi)\Delta t = 10\%$ (squares); here, $g/\omega_c = \frac{1}{16}$ (red symbols) and $g/\omega_c = \frac{1}{8}$ (blue symbols, upper curve). All curves can be fit very well to linear error models (see black dashed lines). Center: set of underlying (temperature-dependent) simulations for both $g/\omega_c = \frac{1}{16}$ (terminating at $\omega_c t/2\pi = 16.5$) and $g/\omega_c = \frac{1}{8}$ (terminating at $\omega_c t/2\pi = 4.5$). Note that larger amplitudes are observed for larger values of $\mu = g/\omega_c$. Other numerical parameters: $Q = 10^5$, $\Gamma = 0$, and $\omega_q = 0$. Right: same analysis as done in Fig. 15 for $g/\omega_c = \frac{1}{8}$ (triangles) and $g/\omega_c = \frac{1}{16}$ (squares). The black curves account for a finite timing accuracy $(\omega_c/2\pi)\Delta t = 5\%$, showing that the detrimental effects of time jitter are less pronounced for smaller values of $\mu = g/\omega_c$.

APPENDIX L: ANALYTICAL EXPRESSION FOR RETHERMALIZATION-INDUCED ERRORS

In this Appendix, we derive an analytical expression for rethermalization-induced errors. In particular, we show that this expression is independent of the spin-resonator coupling strength g.

Our analysis starts out from the master equation

$$\dot{\rho} = -i[H,\rho] + \sum_{j=1,2} \mathcal{D}[L_j]\rho, \tag{L1}$$

where the Hamiltonian $H = \omega_c a^\dagger a + g\mathcal{S}\otimes(a+a^\dagger)$ refers to the ideal (noise-free) dynamics and the jump-operators $L_1 = \sqrt{\kappa_1}a$, $L_2 = \sqrt{\kappa_2}a^\dagger$ with $\kappa_1 = \kappa(\bar{n}_{\rm th}+1)$ and $\kappa_2 = \kappa\bar{n}_{\rm th}$ describe rethermalization of the resonator mode with a rate $\kappa = \omega_c/Q$ that is enhanced by the thermal occupation number $\bar{n}_{\rm th}$. It is convenient to move to an interaction picture, defined by $\tilde{\rho}(t) = \exp[iHt]\rho(t)\exp[-iHt]$. In this interaction picture, the system's dynamics is described by

$$\dot{\tilde{\rho}} = \sum_{j=1,2} \mathcal{D}[\tilde{L}_j]\tilde{\rho}, \tag{L2}$$

with time-dependent jump operators $\tilde{L}_j = \exp[iHt]L_j\exp[-iHt]$. Using the exact relation $\exp[-iHt] = U\exp[-i\omega_c t a^\dagger a]U^\dagger U_{\rm sp}(t)$, with the polaron transformation $U = \exp[\mu\mathcal{S}(a-a^\dagger)]$ and the pure spin (entangling) gate $U_{\rm sp}(t) = \exp[i\mu^2\omega_c t\mathcal{S}^2]$, the time-dependent jump operators $\tilde{L}_j$ take on a simple form

$$\begin{aligned}\tilde{L}_1(\tau) &= \sqrt{\kappa_1}[e^{-i\omega_c\tau}a + (e^{-i\omega_c\tau}-1)\mu\mathcal{S}],\\ \tilde{L}_2(\tau) &= \sqrt{\kappa_2}[e^{i\omega_c\tau}a^\dagger + (e^{i\omega_c\tau}-1)\mu\mathcal{S}].\end{aligned} \tag{L3}$$

The formal solution to Eq. (L2) reads as

$$\tilde{\rho}(t) = \tilde{\rho}(0) + \sum_j \int_0^t d\tau\, \mathcal{D}[\tilde{L}_j(\tau)]\tilde{\rho}(\tau), \tag{L4}$$

where in the interaction picture the zeroth-order solution $\tilde{\rho}_0(t) = \tilde{\rho}(0) = \rho(0)$ stays inert, and accounts for the ideal (noise-free) dynamics only in the laboratory frame, $\rho_0(t) = \exp[-iHt]\tilde{\rho}_0(t)\exp[iHt] = \exp[-iHt]\rho(0)\exp[iHt]$. To obtain the first-order correction $\tilde{\rho}_1(t)$ within a perturbative framework, we reinsert the zeroth-order solution into the dissipator of Eq. (L4), i.e., effectively we take $\tilde{\rho}(\tau)\to\rho(0)$, which yields $\tilde{\rho}(t)\approx\rho(0)+\tilde{\rho}_1(t)$, with

$$\tilde{\rho}_1(t) = \sum_j \int_0^t d\tau\, \mathcal{D}[\tilde{L}_j(\tau)]\rho(0). \tag{L5}$$

Inserting the expressions given in Eq. (L3) into Eq. (L5) and performing the integration, with $\int_0^t d\tau|1-e^{\pm i\omega_c\tau}|^2 = 2[t - \frac{\sin(\omega_c t)}{\omega_c}]$ and $\int_0^t d\tau(1-e^{\pm i\omega_c\tau}) = t \pm i\frac{e^{\pm i\omega_c t}-1}{\omega_c}$, one arrives at

$$\begin{aligned}\tilde{\rho}_1(t) = {}& \kappa_1 t\mathcal{D}[a]\rho(0) + \kappa_2 t\mathcal{D}[a^\dagger]\rho(0) + 2(\kappa_1+\kappa_2)\mu^2\left[t - \frac{\sin(\omega_c t)}{\omega_c}\right]\mathcal{D}[\mathcal{S}]\rho(0)\\ &+\left[\kappa_1\mu\left(t - i\frac{e^{-i\omega_c t}-1}{\omega_c}\right)\left\{a\rho(0)\mathcal{S} - \frac{1}{2}\{a\mathcal{S},\rho(0)\}\right\} + \text{H.c.}\right]\\ &+\left[\kappa_2\mu\left(t + i\frac{e^{i\omega_c t}-1}{\omega_c}\right)\left\{a^\dagger\rho(0)\mathcal{S} - \frac{1}{2}\{a^\dagger\mathcal{S},\rho(0)\}\right\} + \text{H.c.}\right],\end{aligned} \tag{L6}$$

which, for stroboscopic times $t_m = 2\pi m/\omega_c$ (with m integer), simplifies to

$$\begin{aligned}\tilde{\rho}_1(t_m) = {}& \kappa_1 t_m\mathcal{D}[a]\rho(0) + \kappa_2 t_m\mathcal{D}[a^\dagger]\rho(0) + 2(\kappa_1+\kappa_2)\mu^2 t_m\mathcal{D}[\mathcal{S}]\rho(0)\\ &+\left[\kappa_1\mu t_m\left\{a\rho(0)\mathcal{S} - \tfrac{1}{2}\{a\mathcal{S},\rho(0)\}\right\} + \text{H.c.}\right] + \left[\kappa_2\mu t_m\left\{a^\dagger\rho(0)\mathcal{S} - \tfrac{1}{2}\{a^\dagger\mathcal{S},\rho(0)\}\right\} + \text{H.c.}\right].\end{aligned}$$

Next, we perform a transformation back to the laboratory frame, with $\rho(t) = \exp[-iHt]\tilde{\rho}(t)\exp[iHt]$. As discussed in the main text, for stroboscopic times the ideal evolution simplifies to $\exp[-iHt_m] = \exp[i\mu^2 2\pi m\mathcal{S}^2] = \exp(-i\phi_{\rm gp})\exp[i4\pi m\mu^2\sigma_1^x\sigma_2^x]$. The ideal (noise-free) evolution is given by $\rho_{\rm id}(t_m) = \exp[-iHt_m]\rho(0)\exp[iHt_m] = \varrho_{\rm id}(t_m)\otimes\rho_{\rm th}$, where $\varrho_{\rm id}(t_m) = \exp[i4\pi m\mu^2\sigma_1^x\sigma_2^x]\varrho(0)\exp[-i4\pi m\mu^2\sigma_1^x\sigma_2^x]$ is the ideal qubit's state at time t_m, starting from the initial state $\rho(0) = \varrho(0)\otimes\rho_{\rm th}$. Then, the system's density matrix at time t_m is approximately given by

$$\begin{aligned}\rho(t_m) = {}& \rho_{\rm id}(t_m) + \kappa_1 t_m\mathcal{D}[a]\rho_{\rm id}(t_m) + \kappa_2 t_m\mathcal{D}[a^\dagger]\rho_{\rm id}(t_m) + 2(\kappa_1+\kappa_2)\mu^2 t_m\mathcal{D}[\mathcal{S}]\rho_{\rm id}(t_m)\\ &+\left[\kappa_1\mu t_m\left\{a\rho_{\rm id}(t_m)\mathcal{S} - \tfrac{1}{2}\{a\mathcal{S},\rho_{\rm id}(t_m)\}\right\} + \kappa_2\mu t_m\left\{a^\dagger\rho(0)\mathcal{S} - \tfrac{1}{2}\left\{a^\dagger\mathcal{S},\rho(0)\right\}\right\} + \text{H.c.}\right].\end{aligned}$$

Note that, in the limit $\kappa_i\to 0$, one retrieves the ideal result $\rho(t_m) = \rho_{\rm id}(t_m)$. Next, we trace out the resonator mode. Assuming the state of the resonator mode to be diagonal in the occupation number basis (in particular, this holds for a thermal state $\rho_{\rm th}$), none of the cross terms contribute to the partial trace, and for stroboscopic times t_m the state of the qubits is given by

$$\varrho(t_m) = \varrho_{\rm id}(t_m) + 2\kappa(2\bar{n}_{\rm th}+1)t_m\mu^2\mathcal{D}[\mathcal{S}]\varrho_{\rm id}(t_m). \tag{L7}$$

As expected naively, the error term scales with $\sim\kappa\bar{n}_{\rm th}t_m$, but it is further reduced by the factor $\mu^2 = (g/\omega_c)^2$. Equation (L7) holds for stroboscopic times $t_m = 2\pi m/\omega_c$, with m integer. If $m\mu^2 = \frac{1}{16}$, the ideal evolution $\exp[-iHt_m] = \exp(-i\phi_{\rm gp})\exp[i\frac{\pi}{4}\sigma_1^x\sigma_2^x]$ equals a maximally entangling gate, which (for an initial pure state like $|\Psi\rangle_0 = |\downarrow\downarrow\rangle$) yields the desired ideal qubit target state $|\Psi_{\rm tar}\rangle = \exp[i\frac{\pi}{4}\sigma_1^x\sigma_2^x]|\Psi\rangle_0$. Then, in the presence of noise, at the nominally ideal time $t_{\rm max} = \pi/8\mu^2\omega_c = \pi/8g_{\rm eff}$ the qubit's density matrix reads

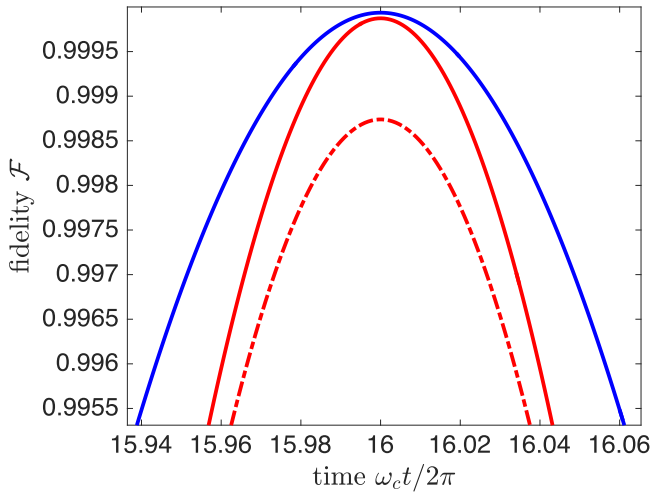

FIG. 18. Fidelity $\mathcal{F}$ close to the ideal time $t_{\max}$ for $g/\omega_c = \frac{1}{16}$. The different curves refer to $Q = 10^5$, $k_B T/\omega_c = 2$, i.e., $\bar{n}_{\rm th} \approx 1.54$ (blue solid, top curve), $Q = 10^5$, $k_B T/\omega_c = 4$, i.e., $\bar{n}_{\rm th} \approx 3.52$ (red solid), and $Q = 10^4$, $k_B T/\omega_c = 4$ (red dashed dotted). The error $\xi = 1 - \mathcal{F}$ can be estimated well with the formula $\xi_k \approx 4\bar{n}_{\rm th}/Q$, giving (for example) $\mathcal{F} \approx 1$–$4 \times 3.52/10^4 \approx 0.9986$. Other numerical parameters: $\Gamma = 0$ and $\omega_q = 0$.

as

$$\varrho(t_{\max}) = |\Psi_{\rm tar}\rangle\langle\Psi_{\rm tar}| + \frac{\pi}{4}\frac{\kappa}{\omega_c}(2\bar{n}_{\rm th}+1)\mathcal{D}[\mathcal{S}]|\Psi_{\rm tar}\rangle\langle\Psi_{\rm tar}|. \tag{L8}$$

Therefore, to first order rethermalization-induced noise leads to dephasing dynamics in the eigenbasis of $\mathcal{S}$ with a single such phase flip. Since neither the desired target state $|\Psi_{\rm tar}\rangle$ nor the initial state $|\Psi\rangle_0$ is an eigenstate of $\mathcal{S}$, the system loses fidelity with a probability $\frac{\pi}{4}\frac{\kappa}{\omega_c}(2\bar{n}_{\rm th}+1)$; notably, this expression is independent of the spin-resonator coupling strength g.

For the fidelity with the maximally entangled target state, we then obtain

$$\mathcal{F} = \langle\Psi_{\rm tar}|\varrho(t_{\max})|\Psi_{\rm tar}\rangle = 1 - \frac{\pi}{2}\frac{\kappa}{\omega_c}(2\bar{n}_{\rm th}+1), \tag{L9}$$

with a thermalization-induced error term given by

$$\xi_\kappa = \pi(\kappa/\omega_c)\bar{n}_{\rm th} + \frac{\pi}{2}Q^{-1}. \tag{L10}$$

This analytical result is in good agreement with our numerical findings [from which we have deduced $\xi_\kappa \approx \alpha_\kappa(\kappa/\omega_c)\bar{n}_{\rm th}$, with $\alpha_\kappa \approx 4$], showing (i) a linear scaling with the effective rethermalization rate $\sim\kappa\bar{n}_{\rm th}$, (ii) with a prefactor $\alpha_\kappa = \pi$ (close to ~ 4) that is *independent* of the spin-resonator coupling strength g, and (iii) a constant offset $\sim Q^{-1}$ which is negligible for realistic quality factors $Q \approx 10^5$–10^6. The latter is due to photon or phonon emission with a rate $\sim\kappa = \omega_c/Q$ at $T \to 0$. As illustrated further in Fig. 18 with a closeup of the fidelity $\mathcal{F}(t)$ around the optimal point $t_{\max}$, the error ξ_κ can be estimated well with this simple formula, where all temperature-related effects are captured by the simple linear expression in the thermal occupation number $\bar{n}_{\rm th}$.

Correlated noise model. An analog analysis to the one presented above can be performed for a master equation with correlated (rather than uncorrelated) noise. In this case, as shown in Appendix J 2, the jump operators are given by $L_1 = \sqrt{\kappa_1}(a + \mu\mathcal{S})$, $L_2 = \sqrt{\kappa_2}(a^\dagger + \mu\mathcal{S})$, which take on a simple form in the interaction picture, namely,

$$\tilde{L}_1(\tau) = \sqrt{\kappa_1}e^{-i\omega_c\tau}(a + \mu\mathcal{S}), \tag{L11}$$

$$\tilde{L}_2(\tau) = \sqrt{\kappa_2}e^{i\omega_c\tau}(a^\dagger + \mu\mathcal{S}), \tag{L12}$$

as compared to Eq. (L3) within the uncorrelated noise model discussed above. Then, following the same steps as above, the integration $\int_0^t d\tau|1 - e^{\pm i\omega_c\tau}|^2 = 2(t - \frac{\sin(\omega_c t)}{\omega_c})$ is simply replaced by $\int_0^t d\tau = t$; accordingly, in this scenario, the prefactor of the spin dephasing term $\mathcal{D}[\mathcal{S}]\rho(0)$ simplifies to $\sim(\kappa_1+\kappa_2)\mu^2 t$, which for stroboscopic times $t_m = 2\pi m/\omega_c$ is exactly a factor of 2 smaller than the corresponding rate in Eq. (L6) for the uncorrelated noise model. In summary, along the lines of our previous analysis, for a correlated noise model, Eqs. (L7) and (L10) should be replaced by

$$\varrho(t_m) = \varrho_{\rm id}(t_m) + \kappa(2\bar{n}_{\rm th}+1)t_m\mu^2\mathcal{D}[\mathcal{S}]\varrho_{\rm id}(t_m) \tag{L13}$$

and

$$\xi_\kappa = \frac{\pi}{2}(\kappa/\omega_c)\bar{n}_{\rm th} + \frac{\pi}{4}Q^{-1}, \tag{L14}$$

respectively, showing that for uncorrelated spin-resonator noise the rethermalization-induced error is approximately twice as large as for correlated spin-resonator noise; also compare the numerical results presented in Table I.

APPENDIX M: ANALYTICAL MODEL FOR DEPHASING-INDUCED ERRORS

In this Appendix, we provide an analytical model for dephasing-induced errors. Neglecting rethermalization-induced errors for the moment, here we consider the following master equation:

$$\dot{\rho} = \underbrace{-i[H_{\rm id},\rho]}_{\mathcal{L}_0\rho} + \underbrace{\gamma_\phi\big[\mathcal{D}\big[\sigma_1^z\big]\rho + \mathcal{D}\big[\sigma_2^z\big]\rho\big]}_{\mathcal{L}_1\rho}, \tag{M1}$$

where $H_{\rm id} = \omega_c a^\dagger a + g(\sigma_1^z + \sigma_2^z)\otimes(a + a^\dagger)$ describes the ideal (error-free), coherent evolution for longitudinal coupling between the qubits and the resonator mode, and γ_ϕ is the pure dephasing rate. Since the superoperators $\mathcal{L}_0$ and $\mathcal{L}_1$ as defined in Eq. (M1) commute, that is, $[\mathcal{L}_0,\mathcal{L}_1] = 0$ (since $[H_{\rm id},\mathcal{D}[\sigma_i^z]X] = \mathcal{D}[\sigma_i^z][H_{\rm id},X]$ for any operator X), the full evolution simplifies to

$$\rho(t) = e^{\mathcal{L}_1 t}e^{\mathcal{L}_0 t}\rho(0) = e^{\mathcal{L}_1 t}\rho_{\rm id}(t), \tag{M2}$$

where we have defined the ideal target state at time t as $\rho_{\rm id}(t) = \exp[\mathcal{L}_0 t]\rho(0)$, which, starting from the initial state $\rho(0)$, exclusively accounts for the ideal (error-free), coherent evolution. For small infidelities ($\gamma_\phi t \ll 1$), the deviation from the ideal dynamics $\Delta\rho = \rho - \rho_{\rm id}$ is approximately given by

$$\Delta\rho(t) \approx \gamma_\phi t\sum_i \mathcal{D}\big[\sigma_i^z\big]\rho_{\rm id}(t), \tag{M3}$$

showing that (in the regime of interest where $\gamma_\phi t \ll 1$) the dominant dephasing-induced errors are linearly proportional to $\sim\gamma_\phi t_g \sim \gamma_\phi/g_{\rm eff} = \gamma_\phi/\mu^2\omega_c$, as expected; here, $t_g \sim g_{\rm eff}$ is the relevant gate time which has to be short compared to γ_ϕ^{-1}.

In what follows, for completeness we derive the same result within a quantum jump approach. Equation (M1) can be rewritten as

$$\dot{\rho} = -iH\rho + i\rho H^\dagger + \mathcal{J}\rho, \tag{M4}$$

where $H = H_{\rm id} - i\gamma_\phi$ and $\mathcal{J}\rho = \gamma_\phi \sum_i \sigma_i^z \rho \sigma_i^z$. The formal solution to Eq. (M4) reads as

$$\rho(t) = e^{-iHt}\rho(0)e^{iH^\dagger t} + \int_0^t d\tau\, e^{-iH(t-\tau)}\mathcal{J}\rho(\tau)e^{iH^\dagger(t-\tau)}. \tag{M5}$$

Defining the ideal target state at time t as

$$\rho_{\rm id}(t) = e^{-iH_{\rm id}(t-\tau)}\rho(\tau)e^{iH_{\rm id}(t-\tau)}, \tag{M6}$$

the exact solution given in Eq. (M5) can be iterated, giving an illustrative expansion in terms of the jumps $\mathcal{J}$. It reads as

$$\begin{aligned}\rho(t) = \mathcal{U}(t)\rho(0) &+ \int_0^t d\tau_1 \mathcal{U}(t-\tau_1)\mathcal{J}\mathcal{U}(\tau_1)\rho(0)\\ &+ \int_0^t d\tau_2 \int_0^{\tau_2} d\tau_1 \mathcal{U}(t-\tau_2)\mathcal{J}\mathcal{U}(\tau_2-\tau_1)\\ &\times \mathcal{J}\mathcal{U}(\tau_1)\rho(0) + \cdots .\end{aligned}$$

Here, the nth-order term comprises n jumps $\mathcal{J}$ with free evolution $\mathcal{U}(t)\rho = e^{-iHt}\rho e^{iH^\dagger t}$ between the jumps. Up to second order in $\mathcal{J}$ we then find

$$\begin{aligned}\rho(t) = \mathcal{U}(t)\rho(0) &+ e^{-2\gamma_\phi t}\gamma_\phi t \sum_i \sigma_i^z \rho_{\rm id}(t)\sigma_i^z \\ &+ \frac{1}{2}e^{-2\gamma_\phi t}\gamma_\phi^2 t^2 \sum_{i,j} \sigma_i^z\sigma_j^z\rho_{\rm id}(t)\sigma_j^z\sigma_i^z + \cdots .\end{aligned} \tag{M7}$$

For the regime of interest where $\gamma_\phi t \ll 1$, we then obtain again the result given in Eq. (M3), where the dominant error term scales linearly with $\sim\gamma_\phi t$.

APPENDIX N: RELAXATION-INDUCED ERRORS

In this Appendix, we address in detail errors induced by relaxation processes, typically characterized by the time scale T_1. First, we discuss typical relaxation time scales for different physical platforms, with particular emphasis on their dependence on both temperature T and qubit-level splitting ω_q. We conclude that interlevel scattering processes typically play a minor role as compared to pure dephasing-induced errors, even in our regime of interest with elevated temperatures of a few Kelvin and small qubit-level splittings. Second, for completeness, we numerically verify the expected linear error scaling $\sim T_1^{-1}$ and, using the fundamental relation $T_2^{-1} = 1/2T_1 + 1/T_\phi$ [79], with T_2^{-1} (T_ϕ^{-1}) referring to the decoherence (pure-dephasing) rate, give an upper bound on decoherence-induced errors.

1. Experimental relaxation time scales

Let us first discuss spin qubits in quantum dots where decoherence predominantly results from spin-orbit interaction and hyperfine interaction with nuclear spins [60,80]. Thereafter, we discuss yet another candidate system for the implementation of the proposed hot gate, consisting of nitrogen-vacancy centers coupled to the vibrational mode of a diamond mechanical nanoresonator via strain [52,81,82].

(i) Single-electron spin qubits. For single-electron spins in GaAs quantum dots the inter-Zeeman level spin scattering is typically dominated by spin-orbit interaction in combination with the emission of single piezoelectric phonons, while other relaxation processes are usually negligible [60,80]. At low temperatures, the corresponding phonon-mediated spin relaxation rate γ_1 shows a well-known, pronounced dependence on magnetic field B, namely,

$$\gamma_1 = T_1^{-1} = A(g_s\mu_B B)^5/\omega_0^4, \tag{N1}$$

where A is a material-specific constant reflecting the effectiveness of the spin-phonon coupling strength, $\omega_q = g_s\mu_B B$ is the Zeeman splitting (with the g factor g_s and Bohr magneton μ_B), and ω_0 refers to the quantum dot single-particle level spacing; compare Refs. [60,80] and references therein. As usual, for elevated temperatures $k_B T \geqslant \omega_q$ this relaxation rate is enhanced by a (bosonic) thermal occupation factor $\bar{n}_{\rm th}(\omega_q) \approx k_B T/\omega_q$ (describing stimulated emission of phonons), yielding a linear scaling with temperature, that is an effective relaxation rate $\gamma_1 \sim \omega_q^4 \times k_B T$ for temperatures much larger than the Zeeman splitting ($k_B T \gg \omega_q$) [83]. Both the strong dependence on the magnetic field B and the linear dependence on temperature $\sim T$ have been confirmed experimentally [60,83], showing extremely long relaxation times of $T_1 > 1$ s at $B = 1$ T and $T = 120$ mK [84], and $T_1 > 20$ ms at $B = 4$ T and $T = 1$ K [83]. For very small magnetic fields B, this expression for T_1 diverges ($\gamma_1 \to 0$) because it accounts for single-phonon processes only (with single phonons in resonance with the Zeeman energy ω_q, as required by energy conservation) and Kramers theorem does not allow for spin-orbit-induced spin relaxation in the absence of a magnetic field [60,80]. When accounting for two-phonon processes, however, T_1 does converge to a finite value [80]. As shown theoretically in Refs. [85,86], the corresponding two-phonon spin-flip rate becomes the dominating (phonon-mediated) scattering mechanism for sufficiently small magnetic fields $\lesssim$0.4 T, with a corresponding two-phonon-mediated scattering rate of $\sim$1 kHz ($T_1 \sim 1$ ms) for $T \approx 4$ K in GaAs, reaching very long relaxation times of $T_1 \sim 1$ s for $T \approx 1$ K and sufficiently small magnetic fields of $B \lesssim 0.1$ T. Similarly, experiments on the relaxation rate from the two-electron triplet to singlet states as a function of the singlet-triplet energy splitting $\Delta E_{\rm ST}$ (referred to as ω_q in our analysis) show relaxation times well below 1 ms as $\Delta E_{\rm ST}$ approaches zero [87], due to a vanishing phonon density of states; compare Fig. 21 in Ref. [60]. Finally, near zero magnetic field ($\omega_q = 0$), in GaAs energy relaxation is known to be dominated by direct hyperfine-mediated electron-nuclear flip flops [60]. For a (relatively small) magnetic field $B \gg B_n \approx 3$ mT (with B_n denoting the effective nuclear magnetic field caused by ambient nuclear spins), however, this mechanism is suppressed efficiently by the mismatch between nuclear and electron Zeeman energies [84], effectively leaving the hyperfine interaction as the well-known, dominating pure-dephasing mechanism for the electron spin qubit [60]. Therefore, as soon as the qubit-level splitting $\omega_q = g_s\mu_B B$ exceeds the typical hyperfine energy scale in GaAs $g_{\rm hf}/2\pi \approx 25$ MHz, one reaches a regime, where T_1 processes can be neglected compared to pure dephasing

$\sim T_2^\star$ (even at temperatures of a few Kelvin), while easily satisfying the inequality $g_{\rm hf} \ll \omega_q \ll \omega_c$ for typical resonator frequencies $\omega_c/2\pi \sim$ GHz, as required for the implementation of the proposed hot gate. The prospects for a faithful implementation of the proposed hot gate are potentially even more promising when switching to materials such as Si and Ge where both hyperfine interactions with the ambient nuclei (since these materials can be grown nuclear-spin free) and piezoelectric electron-phonon coupling (due to bulk inversion symmetry) are absent [79,80]; note that the latter typically dominates spin relaxation in GaAs-based systems [60,85,86]. In fact, silicon-based experiments have demonstrated $T_1 \sim 3$ s at $B = 1.85$ T and $T = 0.15$ K [88], suggesting (according to the usual thermal enhancement) $T_1 \sim 0.3$ s for $T \approx 1$ K, which is still much longer than the spin-dephasing time scale $T_2^\star \sim 100$ μs quoted in the main text and agrees with the common wisdom that spin lifetimes are orders of magnitude longer than the ones reported for GaAs [79,89]; compare our subsequent discussion on singlet-triplet qubits.

(ii) Singlet-triplet spin qubits. For singlet-triplet qubits in silicon relaxation times of $T_1 \sim 10$ ms have been demonstrated at zero magnetic field for cryostat temperatures $T \sim 15$ mK [89], which exceeds the $B = 0$ lifetimes measured in comparable GaAs setups by about two orders of magnitude. As discussed in detail in Appendix D 2, in this system the qubit splitting ω_q is set by the well-controlled exchange splitting J, which can be tuned to very small values. For example, in Ref. [89] $\omega_q/2\pi \approx 16$ MHz, which is much smaller than any relevant resonator frequency ω_c. As argued in Ref. [89], the measured lifetimes of $T_1 \sim 10$ ms (at $B = 0$) are limited by the (small) hyperfine interaction in natural (i.e., not purified) silicon with $g_{\rm hf} \sim 3$ neV. Since the effective relaxation rate at elevated temperatures is determined by integrated autocorrelation functions of the bath operators [yielding, for example, the thermal enhancement factor $\bar{n}_{\rm th}(\omega_q) \approx k_B T/\omega_q$ when coupling to a bosonic bath, as discussed above], very long lifetimes of $T_1 \sim 10$ ms (at $B = 0$) can still be expected, even at higher temperatures $T \sim$ K, because the autocorrelation functions of the relevant nuclear spin bath operators do not show a bosonic thermal enhancement factor; conversely, due to their extremely small magnetic moment, nuclear spins can be treated as an infinite temperature bath, even at ultralow temperatures $\sim$100 mK and strong magnetic fields [90]. Therefore, singlet-triplet qubits in silicon should be well suited for the implementation of the proposed hot gate, with tunable qubits splittings much smaller than relevant resonator frequencies ($\omega_q \ll \omega_c$) and relaxation times T_1 much longer than $T_2^\star$, even at elevated temperatures of a few Kelvin.

(iii) NV centers. Since for nitrogen-vacancy (NV) centers in diamond the spin T_1 time can be several seconds or longer [91–93], even at temperatures of a few Kelvin, it is common practice to neglect the spin decay; compare for example Ref. [52], which may serve as a potential platform for a proof-of-principle implementation of the proposed hot gate. The electronic ground state of the negatively charged NV center is a spin $S = 1$ triplet with spin states $|m_s = 0, \pm 1\rangle$, where the levels $|\pm 1\rangle$ are split off from $|0\rangle$ by the zero-field splitting $D/2\pi = 2.88$ GHz. In the absence of an external magnetic field, the states $|\pm 1\rangle$ are degenerate. As discussed in detail in Refs. [52,81,82], such an electronic spin can be coupled to the motion of a mechanical resonator through lattice strain, with perpendicular strain mixing the $|\pm 1\rangle$ states, which is otherwise a dipole-forbidden transition ($\Delta m_s = 2$) [52,81,82]. If the system is prepared in the $|\pm 1\rangle$ subspace, the state $|0\rangle$ remains unpopulated and the effect of parallel strain plays no role [52], yielding an effective qubit with qubit splitting $\omega_q = 2\gamma_{\rm NV} B$ (with $\gamma_{\rm NV}/2\pi = 2.8$ MHz/G), that is coupled to the mechanical resonator mode of frequency $\omega_c \gg \omega_q$. Then, in the absence of an external magnetic field ($\omega_q = 0$), the effective Hamiltonian $H_{\rm eff}$ for this spin-resonator system takes on the desired form, that is, $H_{\rm eff} = \omega_c a^\dagger a - g_\perp \sigma^x \otimes (a + a^\dagger)$, where $\sigma^x = |+1\rangle\langle -1| + {\rm H.c.}$ and $g_\perp$ is the transverse single-phonon strain-coupling strength [81]. At first sight, in this setup the spin-resonator coupling $g_\perp$ is static and not easily tunable; hence, while it does not provide a universal two-qubit primitive, it can nevertheless be used to generate entanglement at elevated temperatures. The spin-resonator coupling may, however, effectively be switched on and off by making use of the hyperfine coupling to adjacent single nuclear spins where quantum information can be stored with qubit memory lifetimes exceeding 1 s [94].

2. Error scaling

To quantitatively capture the effect of relaxation-induced errors, we have analyzed the master equation

$$\dot{\rho} = -i[H,\rho] + \gamma_1 \sum_i \mathcal{D}[\sigma_i^-]\rho, \tag{N2}$$

where the first term refers to the ideal, coherent dynamics and the second term describes single-spin relaxation with a rate $\gamma_1 = T_1^{-1}$; incoherent excitation processes could be included as well, with additional terms of the same form with the appropriate replacement $\sigma_i^- \to \sigma_i^+$, but are omitted here for clarity. Along the lines of our analysis for dephasing-induced errors, the relaxation-induced error is expected to scale linearly with the relaxation rate as $\xi_\gamma \sim \gamma_1/g_{\rm eff}$, that is,

$$\xi_\gamma \approx \alpha_\gamma \frac{\gamma_1}{\omega_c}, \tag{N3}$$

with the prefactor $\alpha_\gamma = c_\gamma/\mu^2$, where $\mu = g/\omega_c$. As shown in Fig. 19, based on numerical simulations of Eq. (N2), this linear error scaling has been verified numerically, yielding the numerical prefactor $c_\gamma \approx 0.38$, that is, $\alpha_\gamma \approx 0.38/\mu^2$. This numerical prefactor coincides very well with the value obtained for the dephasing-induced error $\sim\Gamma$ [when properly accounting for the factor of four in our definition $\Gamma = 2/T_2^\star$; compare the corresponding master equation (7) in the main text]; recall $\xi_\Gamma \approx \alpha_\Gamma \Gamma/\omega_c = 4\alpha_\Gamma \gamma_\phi/\omega_c$, with $4\alpha_\Gamma \approx 0.4/\mu^2$ and $\gamma_\phi \equiv \Gamma/4$ (to match with our definition of γ_1). Accordingly, in the typical scenario where $T_2^\star \ll T_1$ (as discussed in the previous subsection), indeed relaxation-induced errors (as well as similar incoherent excitation processes) can be safely neglected. In the opposite regime, where pure-dephasing processes are negligible (such that the decoherence time scale reaches its fundamental upper limit $T_2 \leqslant 2T_1$, i.e., the qubit coherence is limited by spin flips), the total error $\xi_{\rm dec}$ induced by qubit decoherence is simply given by $\xi_{\rm dec} \approx \xi_\gamma \approx \alpha_\gamma \gamma_1/\omega_c$. Finally, in the worst-case regime where the pure-dephasing rate and the relaxation rate are comparable ($\gamma_\phi \approx \gamma_1$), the total error due to qubit decoherence amounts to $\xi_{\rm dec} = \xi_\gamma + \xi_\Gamma \approx$

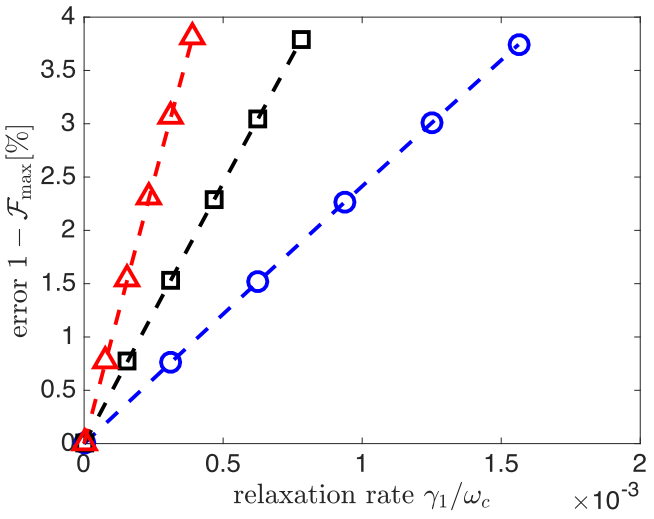

FIG. 19. Relaxation-induced error ξ_γ for $g/\omega_c = \frac{1}{8}$ (blue circles), $g/\omega_c = 1/(8\sqrt{2})$ (black squares), and $g/\omega_c = \frac{1}{16}$ (red diamonds). Other numerical parameters: $k_B T/\omega_c = 0.01$, $\kappa = 0$, $\Gamma = 0$, and $\omega_q = 0$.

$2\alpha_\gamma \gamma_1/\omega_c \approx 2\alpha_\Gamma \Gamma/\omega_c$, i.e., just a factor of 2 larger than the decoherence-induced error considered in the main text.

APPENDIX O: AVERAGE GATE FIDELITY

The average gate fidelity $\bar{F}$ is a useful measure in order to quantify how well the completely positive, trace-preserving quantum operation $\mathcal{M}$ (in the presence of noise) approximates a given unitary gate $U_{\rm id}$, which represents the ideal (noise-free) evolution. Formally, it is defined as

$$\bar{F} = \int d\psi \langle\psi|U_{\rm id}^\dagger \mathcal{M}(|\psi\rangle\langle\psi|)U_{\rm id}|\psi\rangle, \tag{O1}$$

where the integral runs over the uniform (Haar) measure $d\psi$ on state space, with $\int d\psi = 1$ [95]. As shown in Ref. [95], $\bar{F}$ may be reexpressed as

$$\bar{F} = \frac{dF_{\rm ent} + 1}{d+1}, \tag{O2}$$

where d is the dimension of the Hilbert space ($d = 4$ for two qubits) and the entanglement fidelity $F_{\rm ent}$ is the fidelity of the state obtained when $\mathcal{M}$ acts on one-half of a maximally entangled state with the state obtained from the action of the ideal evolution; it is given by

$$F_{\rm ent} = \frac{1}{d^3}\sum_{P\in G} {\rm tr}[P^\dagger U_{\rm id}^\dagger \mathcal{M}(P) U_{\rm id}]. \tag{O3}$$

Here, G is a set of $d \times d$ unitary operators, forming a basis for a qudit, i.e., ${\rm tr}[P_j^\dagger P_k] = \delta_{jk} d$, $j,k = 1,\ldots,d^2$. For two qubits we may take the set of Pauli matrices modulo phase, comprising in total 16 operators $G = \{\mathbb{1}, \sigma_i^\alpha, \sigma_1^\alpha \sigma_2^\beta\}$, with $i = 1,2$, $\alpha = x,y,z$. Experimentally, $\bar{F}$ may be determined using standard state tomography [95].

Errors. The average gate error (infidelity) is defined as $\bar{E} = 1 - \bar{F}$. As follows directly from Eq. (O2), it is related to the entanglement infidelity $E_{\rm ent} = 1 - F_{\rm ent}$ via $\bar{E} = d/(d+1) \times E_{\rm ent}$; thus, for two qubits $\bar{E} = (4/5)E_{\rm ent}$.

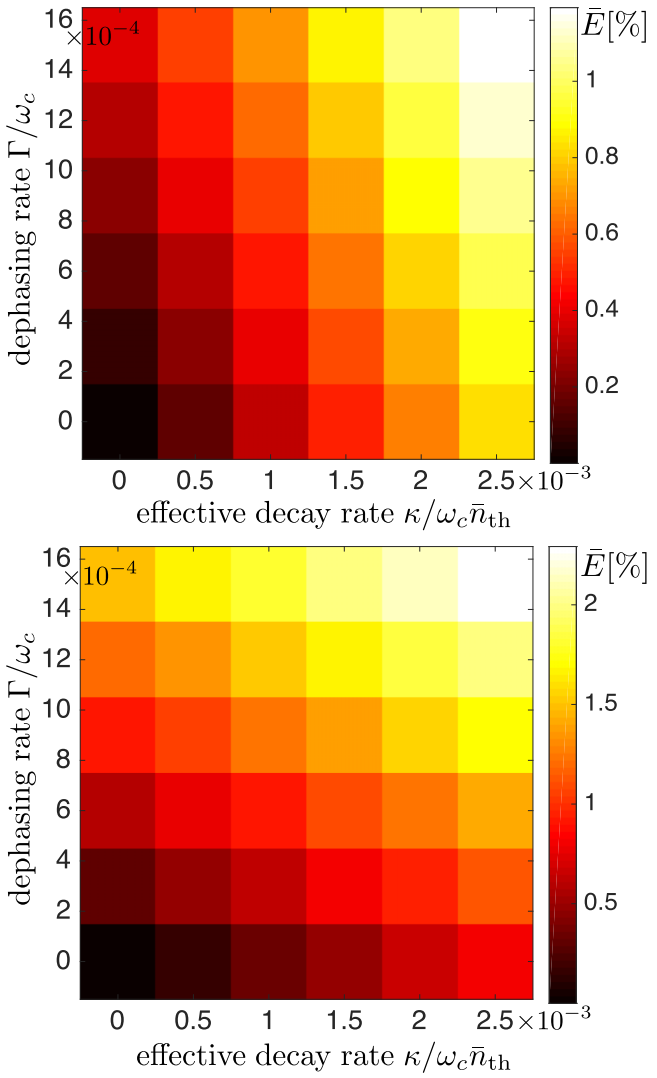

FIG. 20. Total average gate error $\bar{E}$ (in percent) as a function of both the effective rethermalization rate $\sim\kappa/\omega_c \bar{n}_{\rm th} \sim \bar{n}_{\rm th}/Q$ and the spin dephasing rate $\sim\Gamma/\omega_c$ for $g/\omega_c = \frac{1}{4}$ (top) and $g/\omega_c = \frac{1}{8}$ (bottom). Other numerical parameters: $k_B T/\omega_c = 2$ and $\omega_q = 0$.

Numerical results. Numerical results for the average gate error $\bar{E}$ are presented in Fig. 20. Here, the map $\mathcal{M}(P)$ is given implicitly as $\mathcal{M}(P) = {\rm tr}_a[e^{\mathcal{L}t_{\max}} P \otimes \rho_{\rm th}]$, where the superoperator $\mathcal{L}\bullet = -i[H,\bullet] + \mathcal{L}_{\rm noise}\bullet$ is the Liouvillian associated with the master equation given in Eq. (7) in the main text, which includes undesired processes due to rethermalization of the cavity mode and dephasing of the spins. Broadly speaking, our numerical results for the (average) gate error $\bar{E}$ are comparable to the ones obtained for the state infidelity $\xi = 1 - \mathcal{F}$, as discussed in the main text. First, comparison of our results for $g/\omega_c = \frac{1}{4}$ and $\frac{1}{8}$ shows that rethermalization-induced errors are approximately independent of the spin-resonator coupling g; for example, for $\Gamma = 0$ and $\kappa/\omega_c \bar{n}_{\rm th} = 2.5 \times 10^{-3}$ we find $\bar{E}_\kappa \approx 0.82\%$ for both $g/\omega_c = \frac{1}{4}$ and $\frac{1}{8}$, respectively. Second, as expected, the dephasing-induced error scales as $\bar{E}_\Gamma \sim 1/g^2 \sim 1/\mu^2$; for example, as shown in Fig. 20, for $\kappa = 0$ and $\Gamma/\omega_c = 1.5 \times 10^{-3}$, we find $\bar{E}_\Gamma \approx 0.376\%$ and $\bar{E}_\Gamma \approx 1.49\% \approx 4 \times 0.376\%$ for $g/\omega_c = \frac{1}{4}$ and $\frac{1}{8}$, respectively.

[1] R. Hanson and D. D. Awschalom, Nature (London) **453**, 1043 (2008).
[2] M. A. Nielsen and I. L. Chuang, *Quantum Computation and Quantum Information* (Cambridge University Press, Cambridge, UK, 2010).
[3] L. R. Schreiber and H. Bluhm, Nat. Nanotechnol. **9**, 966 (2014).
[4] E. Knill, Nature (London) **434**, 39 (2005).
[5] N. H. Nickerson, Y. Li, and S. C. Benjamin, Nat. Commun. **4**, 1756 (2013).
[6] J. Majer *et al.*, Nature (London) **449**, 443 (2007).
[7] M. A. Sillanpää, J. I. Park, and R. W. Simmonds, Nature (London) **449**, 438 (2007).
[8] F. Schmidt-Kaler *et al.*, Nature (London) **422**, 408 (2003).
[9] A. Sorensen and K. Molmer, Phys. Rev. Lett. **82**, 1971 (1999).
[10] A. Sorensen and K. Molmer, Phys. Rev. A **62**, 022311 (2000).
[11] K. Molmer and A. Sorensen, Phys. Rev. Lett. **82**, 1835 (1999).
[12] G. J. Milburn, arXiv:quant-ph/9908037.
[13] G. J. Milburn, S. Schneider, and D. F. V. James, Fortschr. Phys. **48**, 801 (2000).
[14] J. F. Poyatos, J. I. Cirac, and P. Zoller, Phys. Rev. Lett. **81**, 1322 (1998).
[15] J. I. Cirac and P. Zoller, Nature (London) **404**, 579 (2000).
[16] J. J. Garcia-Ripoll, P. Zoller, and J. I. Cirac, Phys. Rev. Lett. **91**, 157901 (2003).
[17] J. J. Garcia-Ripoll, P. Zoller, and J. I. Cirac, Phys. Rev. A **71**, 062309 (2005).
[18] D. Porras and J. I. Cirac, Phys. Rev. Lett. **92**, 207901 (2004).
[19] D. Leibfried *et al.*, Nature (London) **422**, 412 (2003).
[20] G. Kirchmair, J. Benhelm, F. Zähringer, R. Gerritsma, C. F. Roos, and R. Blatt, New J. Phys. **11**, 023002 (2009).
[21] A. J. Kerman, New J. Phys. **15**, 123011 (2013).
[22] B. Royer, A. L. Grimsmo, N. Didier, and A. Blais, arXiv:1603.04424.
[23] D. J. Reilly, NPJ Quantum. Inf. **1**, 15011 (2015).
[24] P. Treutlein, C. Genes, K. Hammerer, M. Poggio, and P. Rabl, Hybrid Mechanical Systems in *Cavity Optomechanics*, edited by M. Aspelmeyer, T. J. Kippenberg, and F. Marquardt (Springer, Berlin, 2014), pp. 327–351.
[25] A. Blais, R.-S. Huang, A. Wallraff, S. M. Girvin, and R. J. Schoelkopf, Phys. Rev. A **69**, 062320 (2004).
[26] L. Childress, A. S. Sorensen, and M. D. Lukin, Phys. Rev. A **69**, 042302 (2004).
[27] J. M. Taylor and M. D. Lukin, arXiv:cond-mat/0605144.
[28] P.-Q. Jin, M. Marthaler, A. Shnirman, and G. Schon, Phys. Rev. Lett. **108**, 190506 (2012).
[29] X. Hu, Y.-X. Liu, and F. Nori, Phys. Rev. B **86**, 035314 (2012).
[30] M. Trif, V. N. Golovach, and D. Loss, Phys. Rev. B **77**, 045434 (2008).
[31] M. J. Gullans, Y.-Y. Liu, J. Stehlik, J. R. Petta, and J. M. Taylor, Phys. Rev. Lett. **114**, 196802 (2015).
[32] P.-Q. Jin, M. Marthaler, J. H. Cole, A. Shnirman, and G. Schon, Phys. Rev. B **84**, 035322 (2011).
[33] M. Kulkarni, O. Cotlet, and H. E. Tureci, Phys. Rev. B **90**, 125402 (2014).
[34] V. Srinivasa, J. M. Taylor, and C. Tahan, Phys. Rev. B **94**, 205421 (2016).
[35] T. Frey, P. J. Leek, M. Beck, A. Blais, T. Ihn, K. Ensslin, and A. Wallraff, Phys. Rev. Lett. **108**, 046807 (2012).
[36] K. D. Petersson, L. W. McFaul, M. D. Schroer, M. Jung, J. M. Taylor, A. A. Houck, and J. R. Petta, Nature (London) **490**, 380 (2012).
[37] Y.-Y. Liu, K. D. Petersson, J. Stehlik, J. M. Taylor, and J. R. Petta, Phys. Rev. Lett. **113**, 036801 (2014).
[38] H. Toida, T. Nakajima, and S. Komiyama, Phys. Rev. Lett. **110**, 066802 (2013); Also see A. Wallraff, A. Stockklauser, T. Ihn, J. R. Petta, and A. Blais, *ibid.* **111**, 249701 (2013).
[39] M. R. Delbecq, V. Schmitt, F. D. Parmentier, N. Roch, J. J. Viennot, G. Feve, B. Huard, C. Mora, A. Cottet, and T. Kontos, Phys. Rev. Lett. **107**, 256804 (2011).
[40] J. J. Viennot, M. R. Delbecq, M. C. Dartiailh, A. Cottet, and T. Kontos, Phys. Rev. B **89**, 165404 (2014).
[41] J. J. Viennot, M. C. Dartiailh, A. Cottet, and T. Kontos, Science **349**, 408 (2015).
[42] L. J. Zou, D. Marcos, S. Diehl, S. Putz, J. Schmiedmayer, J. Majer, and P. Rabl, Phys. Rev. Lett. **113**, 023603 (2014).
[43] F. Beaudoin, D. Lachance-Quirion, W. A. Coish, and M. Pioro-Ladriere, Nanotechnology **27**, 464003 (2016).
[44] X. Mi, J. V. Cady, D. M. Zajac, P. W. Deelman, and J. R. Petta, Science **355**, 156 (2017).
[45] A. Stockklauser, P. Scarlino, J. V. Koski, S. Gasparinetti, C. K. Andersen, C. Reichl, W. Wegscheider, T. Ihn, K. Ensslin, and A. Wallraff, Phys. Rev. X **7**, 011030 (2017).
[46] M. J. A. Schuetz, E. M. Kessler, G. Giedke, L. M. K. Vandersypen, M. D. Lukin, and J. I. Cirac, Phys. Rev. X **5**, 031031 (2015).
[47] J. C. Chen, Y. Sato, R. Kosaka, M. Hashisaka, K. Muraki, and T. Fujisawa, Sci. Rep. **5**, 15176 (2015).
[48] D. A. Golter, T. Oo, M. Amezcua, K. A. Stewart, and H. Wang, Phys. Rev. Lett. **116**, 143602 (2016).
[49] P. Rabl, P. Cappellaro, M. V. Guredev Dutt, L. Jiang, J. R. Maze, and M. D. Lukin, Phys. Rev. B **79**, 041302(R) (2009).
[50] P. Rabl, S. J. Kolkowitz, F. H. L. Koppens, J. G. E. Harris, P. Zoller, and M. D. Lukin, Nat. Phys. **6**, 602 (2010).
[51] K. V. Kepesidis, S. D. Bennett, S. Portolan, M. D. Lukin, and P. Rabl, Phys. Rev. B **88**, 064105 (2013).
[52] S. D. Bennett, N. Y. Yao, J. Otterbach, P. Zoller, P. Rabl, and M. D. Lukin, Phys. Rev. Lett. **110**, 156402 (2013).
[53] A. Palyi, P. R. Struck, M. Rudner, K. Flensberg, and G. Burkard, Phys. Rev. Lett. **108**, 206811 (2012).
[54] C. Cohen-Tannoudji, J. Dupont-Roc, and G. Grynberg, *Atom-Photon Interactions: Basic Processes and Applications* (Wiley, New York, 1992).
[55] R. J. Schoelkopf and S. M. Girvin, Nature (London) **451**, 664 (2008).
[56] N. Samkharadze, A. Bruno, P. Scarlino, G. Zheng, D. P. DiVincenzo, L. DiCarlo, and L. M. K. Vandersypen, Phys. Rev. Applied **5**, 044004 (2016).
[57] R. Barends, J. J. A. Baselmans, S. J. C. Yates, J. R. Gao, J. N. Hovenier, and T. M. Klapwijk, Phys. Rev. Lett. **100**, 257002 (2008).
[58] M. Veldhorst *et al.*, Nat. Nanotechnol. **9**, 981 (2014).
[59] Chow *et al.*, Phys. Rev. Lett. **109**, 060501 (2012).
[60] R. Hanson, L. P. Kouwenhoven, J. R. Petta, S. Tarucha, and L. M. K. Vandersypen, Rev. Mod. Phys. **79**, 1217 (2007).
[61] J. Levy, Phys. Rev. Lett. **89**, 147902 (2002).
[62] K. E. Cahill and R. J. Glauber, Phys. Rev. **177**, 1857 (1969).
[63] M. V. Gustafsson, P. V. Santos, G. Johansson, and P. Delsing, Nat. Phys. **8**, 338 (2012).

[64] R. Manenti, M. J. Peterer, A. Nersisyan, E. B. Magnusson, A. Patterson, and P. J. Leek, Phys. Rev. B **93**, 041411(R) (2016).
[65] F. K. Malinowski *et al.*, Nat. Nanotechnol. **12**, 16 (2017).
[66] P. Zoller, Quantum Optics: Continous Measurement, Stochastic Schrödinger Equations, Master Equations etc., lecture notes, available online (http://www.coqus.at/fileadmin/quantum/coqus/documents/Klemens_Hammerer/QO_Zoller_Lecture2-Continous_Measurement.pdf).
[67] P. Rabl, Advanced Quantum Optics, lecture notes TU Vienna (unpublished).
[68] P.-O. Guimond, H. Pichler, A. Rauschenbeutel, and P. Zoller, Phys. Rev. A **94**, 033829 (2016).
[69] C. W. Gardiner and P. Zoller, *Quantum Noise* (Springer, Berlin, 2000).
[70] Y. Yamamoto and A. Imamoglu, *Mesoscopic Quantum Optics* (Wiley, New York, 1999).
[71] H. J. Carmichael, *Statistical Methods in Quantum Optics 1* (Springer, Berlin, 2002).
[72] I. de Vega and D. Alonso, Rev. Mod. Phys. **89**, 015001 (2017).
[73] J. Paavola, Role of the environmental spectrum in the decoherence and dissipation of a quantum Brownian particle, Master's thesis, University of Turku, 2008.
[74] F. Beaudoin, J. M. Gambetta, and A. Blais, Phys. Rev. A **84**, 043832 (2011).
[75] M. Scala, B. Militello, A. Messina, S. Maniscalco, J. Piilo, and K. A. Suominen, J. Phys. A: Math. Gen. **40**, 14527 (2007).
[76] A. Blais, J. Gambetta, A. Wallraff, D. I. Schuster, S. M. Girvin, M. H. Devoret, and R. J. Schoelkopf, Phys. Rev. A **75**, 032329 (2007).
[77] H. Wang and G. Burkard, Phys. Rev. B **92**, 195432 (2015).
[78] E. Bocquillon *et al.*, Science **339**, 1054 (2013).
[79] V. Kornich, C. Kloeffel, and D. Loss, Phys. Rev. B **89**, 085410 (2014).
[80] C. Kloeffel and D. Loss, Annu. Rev. Condens. Matter Phys. **4**, 51 (2013).
[81] A. Barfuss, J. Teissier, E. Neu, A. Nunnenkamp, and P. Maletinsky, Nat. Phys. **11**, 820 (2015).
[82] J. Teissier, A. Barfuss, P. Appel, E. Neu, and P. Maletinsky, Phys. Rev. Lett. **113**, 020503 (2014).
[83] M. Kroutvar, Y. Ducommun, D. Heiss, M. Bichler, D. Schuh, G. Abstreiter, and J. J. Finley, Nature (London) **432**, 81 (2004).
[84] S. Amasha, K. MacLean, I. P. Radu, D. M. Zumbuhl, M. A. Kastner, M. P. Hanson, and A. C. Gossard, Phys. Rev. Lett. **100**, 046803 (2008).
[85] L. M. Woods, T. L. Reinecke, and Y. Lyanda-Geller, Phys. Rev. B **66**, 161318 (2002).
[86] A. V. Khaetskii and Y. V. Nazarov, Phys. Rev. B **64**, 125316 (2001).
[87] T. Meunier, I. T. Vink, L. H. Willems van Beveren, K. J. Tielrooij, R. Hanson, F. H. L. Koppens, H. P. Tranitz, W. Wegscheider, L. P. Kouwenhoven, and L. M. K. Vandersypen, Phys. Rev. Lett. **98**, 126601 (2007).
[88] C. B. Simmons, J. R. Prance, B. J. Van Bael, T. S. Koh, Z. Shi, D. E. Savage, M. G. Lagally, R. Joynt, M. Friesen, S. N. Coppersmith, and M. A. Eriksson, Phys. Rev. Lett. **106**, 156804 (2011).
[89] J. R. Prance, Z. Shi, C. B. Simmons, D. E. Savage, M. G. Lagally, L. R. Schreiber, L. M. K. Vandersypen, M. Friesen, R. Joynt, S. N. Coppersmith, and M. A. Eriksson, Phys. Rev. Lett. **108**, 046808 (2012).
[90] H. Christ, J. I. Cirac, and G. Giedke, Phys. Rev. B **78**, 125314 (2008).
[91] R. Amsuss, C. Koller, T. Nobauer, S. Putz, S. Rotter, K. Sandner, S. Schneider, M. Schrambock, G. Steinhauser, H. Ritsch, J. Schmiedmayer, and J. Majer, Phys. Rev. Lett. **107**, 060502 (2011).
[92] J. Harrison, M. Sellars, and N. Manson, Diam. Relat. Mater. **15**, 586 (2006).
[93] A. Jarmola, V. M. Acosta, K. Jensen, S. Chemerisov, and D. Budker, Phys. Rev. Lett. **108**, 197601 (2012).
[94] P. C. Maurer *et al.*, Science **336**, 1283 (2012).
[95] M. A. Nielsen, Phys. Lett. A **303**, 249 (2002).